Doctoral Dissertation
Doctoral Program in Electrical, Electronics and Telecommunications Engineering
(37^{th} cycle)

Treatment Planning and Real-time Temperature Monitoring in Microwave Cancer Hyperthermia

Maryam Firuzalizadeh

* * * * *

Supervisors
Prof. Giuseppe Vecchi, Supervisor
Dr. Rossella Gaffoglio, Co-supervisor
Dr. Giorgio Giordanengo, Co-supervisor
Dr. Marco Righero, Co-supervisor

Doctoral examination committee
Prof. Paolo Maccarini, Referee, Duke University
Prof. Tommaso Isernia, Referee, Università Mediterranea di Reggio Calabria

Politecnico di Torino
2025

I hereby declare that the contents and organisation of this dissertation constitute my own original work and does not compromise in any way the rights of third parties, including those relating to the security of personal data.

.....

Maryam Firuzalizadeh

Turin, 2025

Summary

Hyperthermia (HT) has emerged as a promising adjuvant cancer therapy, leveraging controlled heating of tumor tissues to 40-44°C to enhance the efficacy of radiotherapy and chemotherapy. Despite its clinical potential, widespread adoption of HT is hindered by challenges in precise energy delivery, patient-specific optimization and real-time treatment monitoring.

This thesis presents a comprehensive investigation into the treatment planning methods, experimental validation, and real-time temperature monitoring in microwave hyperthermia.

The first contribution concerns the development of reproducible tissue-mimicking phantoms and consequently the development of an experimental testbed to replicate head and neck (H&N) hyperthermia treatments. This was complemented by a digital twin implemented in COMSOL Multiphysics to enable validation and complement experimental measurements. Next, we introduced a joint SAR-based optimization strategy integrating array matching, aimed at improving antenna performance, ensuring efficient tumor targeting, and reducing reflection coefficients while maintaining electronic stability. The influence of blood flow on heat focusing was then analyzed, highlighting the importance of accounting for major vessels in treatment planning.

Building on these foundations, the third and main contribution is a novel real-time 3D temperature reconstruction method, which integrates sparse invasive thermometry with pre-computed libraries of patient-specific simulations. Validated in fully anthropomorphic phantoms (Duke and Ella from the Sim4Life virtual population), and the developed experimental setup, this approach enables minimally invasive, low-cost, and robust temperature monitoring method. Finally, a deterministic Alternating Projections Algorithm (APA) for SAR-based optimization was proposed as an alternative to metaheuristic methods, achieving comparable thermal performance with improved hotspot suppression and reduced power requirements.

Overall, this work provides methodological and computational advances to enhance the safety, accuracy, and clinical feasibility of microwave hyperthermia, contributing toward its broader adoption as an effective adjunct in cancer therapy.

Acknowledgements

The author would like to thank to the company co-supervisors from Fondazione LINKS Dr. Rossella Gaffoglio, Dr. Marco Righero and Dr. Giorgio Giordanengo for their supervision, collaboration and co-authoring of the work presented in this thesis. Also thanks to my supervisor Professor Giuseppe Vecchi without whom this presented research would have been impossible.

This work was supported by the projects:

1. "Real-Time Temperature Maps Reconstruction in Microwave Cancer Hyperthermia — T-REX", funded by Fondazione Compagnia di San Paolo, Convenzione 2022-2024, Proof of Concept (PoC), CUT-OFF 2 initiative.

2. "Real-Time Temperature Maps Reconstruction in Microwave Cancer Hyperthermia — RESOLVED", funded by Fondazione Compagnia di San Paolo, Bando vEIColo, accompagnamento per la valorizzazione della ricerca, Linea 1.

Contents

List of Tables VIII

List of Figures X

1 Overview 1

2 Hyperthermia cancer therapy 3
- 2.1 Thermal therapies: overview . . . 3
- 2.2 Hyperthermia: state of the art . . . 4
- 2.3 Governing Physics . . . 6
  - 2.3.1 Maxwell's Equations . . . 7
  - 2.3.2 Bioheat Equation . . . 8
- 2.4 Hyperthermia Treatment Planning and Optimization . . . 9
- 2.5 Temperature Monitoring in HT . . . 10
  - 2.5.1 Non-Invasive Thermometry Methods . . . 10
  - 2.5.2 Invasive Thermometry Methods . . . 11
- 2.6 Challenges and Future Directions . . . 12

3 Experimental Setup and Numerical Modeling for Microwave Hyperthermia 15
- 3.1 Introduction . . . 15
- 3.2 Tissue-Mimicking Phantom Development . . . 16
  - 3.2.1 Preparation method . . . 17
  - 3.2.2 Characterization . . . 17
  - 3.2.3 Results and discussion . . . 19
- 3.3 Experimental Setup and its Digital Twin . . . 19
  - 3.3.1 Experimental Testbed . . . 20
  - 3.3.2 COMSOL Model . . . 26

4 SAR-based Optimization 31
- 4.1 Introduction . . . 31
  - 4.1.1 State-of-the-Art . . . 32
  - 4.1.2 Innovation . . . 33

4.2 Joint Optimization Approach . . . 33
4.3 Application and Validation . . . 35
4.4 Conclusions . . . 44

5 Heat Focusing and Blood Flow Considerations 47
5.1 Introduction . . . 47
5.2 Methodology . . . 48
5.3 Results and Discussion . . . 50
5.3.1 Heating Session Without Vessels . . . 50
5.3.2 Heating Session With Vessels . . . 52
5.4 Conclusion . . . 54

6 Real-time 3D Temperature Reconstruction 55
6.1 Introduction . . . 55
6.2 Methodology . . . 58
6.3 Realistic In-silico testbed . . . 62
6.4 SAR-based optimization . . . 64
6.5 Validation of the method using the in-silico testbed . . . 66
6.6 Discussion of the in-silico results . . . 74
6.7 Experimental Testbed . . . 76
6.8 Validation of the Method Using the Experimental Testbed . . . 78
6.9 Conclusion . . . 84

7 SAR-based Optimization via Local Power Synthesis Algorithm 87
7.1 Introduction . . . 87
7.2 Optimization method . . . 89
7.3 Results . . . 93
7.3.1 Reference testbed . . . 93
7.3.2 Power levels search . . . 94
7.3.3 SoA comparison . . . 96
7.3.4 Realistic testbed . . . 100
7.4 Discussion and future works . . . 105
7.5 Conclusions . . . 105

8 Conclusions 107

Bibliography 109

List of Tables

3.1 Dielectric properties of the main phantom at $f = 434$ MHz evaluated with the Method 1 during different experimental sessions 18
3.2 Dielectric properties of the main phantom at $f = 434$ MHz evaluated with the Method 2 during different sessions 18
3.3 Dielectric and thermal properties of the implemented phantoms . . 18
3.4 Dielectric and thermal properties of the materials used in the mock-up at $f = 434$ MHz and room at temperature. 21
3.5 Coordinates of the FBG sensors along the different arrays 25
4.1 Antenna feeding coefficients (ξ_n, φ_n) and corresponding magnitude of the simulated active reflection coefficients $\left(\left|\Gamma^a_{n,sim}\right|\right)$ 37
4.2 Comparison of the considered optimization approaches and their properties 37
4.3 Antenna phases optimized using the proposed cost function $(\mathcal{F})$ and comparison of the simulated and measured magnitude of the active reflection coefficients 41
5.1 Center coordinates and diameters of key elements within the neck phantom 49
5.2 Coordinates of FBG sensors used during the heating session without vessels. 50
5.3 Coordinates of FBG sensors used during the heating session with vessel-mimicking tubes. 52
6.1 coordinates of the tumor target centroid. 62
6.2 optimized antenna amplitudes and phases for different phantoms and target positions. 65
6.3 Considered tissues' properties, baseline values, and the extreme range of the variation 67
6.4 Position and characteristics of the 8 catheters used for each tumor's position; z_c is the z-coordinate of the tumor centroid. 71
6.5 Median and inter-quartile range (IQR) of the standard estimators using the proposed method and the SoA approach 74
6.6 Coordinates of the FBG sensors along the different arrays. 76

6.7 measured dielectric properties of the materials used in the prototype and ideal estimates of the heat transfer coefficients with the corresponding variation ranges. 79
6.8 Temperature reconstruction accuracy over all probes and the complete heating session duration 84
7.1 Optimized antenna excitation coefficients (amplitudes and phases) for APA and PSO 97
7.2 Comparison of the convergence indicators for APA and PSO 97
7.3 Standard thermal estimators obtained with the different methods . 100
7.4 Standard thermal estimators obtained with the different methods . 105

List of Figures

2.1 The different types of Electromagnetic-Based Hyperthermia Techniques [15]. 5
2.2 Clinical integration of the HYPERcollar hyperthermia applicator in two patients with tumors located in the (a) oropharynx and (b) nasopharynx/nasal cavity [16]. The waterbolus, visible between the applicator and patient's neck/head, improves electromagnetic coupling and provides surface cooling. 5
2.3 Hyperthermia Treatment Planning Stages [39]. 10
3.1 Preparation of the semi-solid agar mixture using an electric hotplate and a temperature probe. 16
3.2 a: Neck phantom container with the agar-based phantom; b: target sphere representing the tumor; c: view of the complete neck phantom with the tumor target inside. 17
3.3 (a) Experimental prototype reproducing an HT applicator for deep-seated and sub-superficial tumors in the H&N region. (b) Digital twin of the implemented mock-up developed using COMSOL Multiphysics. 20
3.4 (a) Perspective and side view of the designed antenna with the optimized parameters. (b) Top view of the hyperthermia mock-up simulated in COMSOL. 21
3.5 Comparison of simulated reflection coefficients for a single antenna optimized in a simplified layered scenario versus its performance as part of an 8-element array, alongside experimental measurements. . 22
3.6 (a) Overview of the complete experimental apparatus. (b) Insets showing the position of the tumor target and the FBG arrays before (*top*) and after (*bottom*) the introduction of the agar mixture reproducing the muscle tissue. 23
3.7 Block diagram of the antenna array feeding network. Only 4 of the 8 channels are depicted for clarity. 24
3.8 (a) Positions of the arrays of FBGs on the xy plane. (b) z-coordinates of the FBGs along the arrays (the Array 1 passing through the tumor target is depicted as an example). 25

3.9 (a) The top view layout of the HT mock-up (b) Digital twin of the implemented mock-up developed in COMSOL Multiphysics environment. 26
3.10 PEC Boundary Condition. 27
3.11 Heat Flux Boundary Conditions 27
3.12 (a) Finite Element mesh of simulated prototype in COMSOL, (b) Spherical Perfectly Matched Layers (PML) considered in EM simulation. Note that only half of the sphere is shown here for visualization purposes. 28
4.1 (a) Simulated normalized SAR contours at a depth of 1 cm within the phantom along the x axis. The 0.5 isoline encloses the region used to estimate the effective field size (EFS). (b) Normalized SAR map visualized on a plane at 1 cm depth within the phantom. (c) Normalized SAR values versus the depth inside the phantom, evaluated along the x-axis for constant $y = z = 0$ mm. All results refer to the case when only antenna 7 is fed (see Fig. 3.4b for details on the numbering used). 36
4.2 (a) Standard cost function (HTQ) evolution. Normalized SAR distribution obtained in COMSOL Multiphysics using the feeding coefficients corresponding to the minimization of the standard cost function (HTQ), displayed on the (b) xy plane , (c) xz plane , and (d) yz plane. The dash circle indicates the profile of the considered target spherical region. 38
4.3 (a) Proposed cost function ($\mathcal{F}$) evolution alongside the corresponding HTQ. Normalized SAR distribution obtained in COMSOL Multiphysics using the feeding coefficients corresponding to the minimization of the proposed cost function ($\mathcal{F}$), displayed on the (b) xy plane , (c) xz plane , and (d) yz plane . The dash circle indicates the profile of the considered target spherical region. 39
4.4 Setup of the experimental mock-up reproducing the HT applicator. Components are labeled as follows: a) RF signal coming from Power Amplifier (PA) – Variable Gain Amplifier (VGA) – Phase Shifter (PS) chain, b) Circulator, c) Dummy Load, d) Directional Coupler, e) Patch Antenna, f) Neck Phantom, g) Waterbolus with circulating water. 40
4.5 Temperatures recorded by the FOS arrays at (a) the beginning , and at (b) the end of the heating session. 42
4.6 Temperature values read by the array of FBG sensors passing through the tumor target (array 1) as function of time and of the z-coordinate. 43
4.7 Measured temperatures and simulated values as function of time at the z coordinate corresponding to the tumor center ($z = z_t = 0$ mm). 44

5.1 (a) Experimental setup of the HT mock-up. (b) Zoomed view of the central section showing the neck phantom prior to pouring the agar mixture, with embedded silicone tubes simulating the major blood vessels and the red sphere representing the tumor target. 48
5.2 (a) Digital twin of the experimental setup implemented in COMSOL Multiphysics. (b) Cross-sectional view in the xy plane showing the four silicone tubes simulating blood vessels (blue: jugular veins; red: carotid arteries). (c) 3D visualization of the neck phantom highlighting vessel arrangement and blood flow directions. 49
5.3 Heating session results for the phantom without vessels: Temperature read by the arrays of FBG sensors at the beginning (upper row) and at the end (lower row) of the heating session; the position of the different arrays on the xy plane is indicated in the upper row (right picture) and reported in Table 5.2, together with the z-coordinates of the corresponding FBG sensors. 51
5.4 Heating session without vessels: comparison between experimental and simulated temperature results. Top: temperature evolution over time at the tumor center ($z = z_t = 0$ mm). Bottom: temperature distribution along the z-axis at the end of the heating session ($t =$ 120 min). 52
5.5 Heating session results for the phantom incorporating vessels: Temperature read by the arrays of FBG sensors at the beginning (upper row) and at the end (lower row) of the heating session; the position of the different arrays on the xy plane is indicated in the upper row (right picture) and reported in Table 5.3, together with the z-coordinates of the corresponding FBG sensors. 53
5.6 Heating session with vessels: comparison between experimental and simulated temperature results. Top: temperature evolution over time at the tumor center ($z = z_t = 0$ mm). Bottom: temperature distribution along the z-axis at the end of the heating session ($t = 160$ min). 54
6.1 Proposed method. Flow chart reporting the approach used nowadays in the clinic to perform HT treatments (State-of-the-Art (SoA) approach) and the proposed methodology. 59
6.2 Fully-anthropomorphic phantoms and target positions: (a) Fully-anthropomorphic male phantom Duke V3.0 and different positions of the target region displayed on the xy-plane; (b) Fully-anthropomorphic female phantom Ella cV3.1 and different positions of the target region. 62

6.3 (**a**) Fully anthropomorphic phantom Duke and tumor mass with irregular shape inserted in the neck of the phantom; the overall dimensions of the tumor mass are reported in the inset. (**b**) Top view of the phased array applicator surrounding the segmented phantom visualized on the xy plane; the reported number are used to index the antennas of the array; the tumor target (T1) is highlighted in green. (**c**) Employed patch antenna and optimized dimensions. (**d**) Optimized reflection coefficient; a bandwidth (-10 dB) of about 30 MHz is achieved around the central frequency (434 MHz) (dashed line). 63
6.4 Optimized SAR distribution simulated in Sim4Life for both phantoms Duke (top row) and Ella (bottom row), displayed on the three canonical planes cutting the tumor sphere at its centroid. The green dot on the SAR distribution displayed on the xy plane indicates the position T1 of the tumor's centroid. 66
6.5 Temperature maps variation. (a-c) Boxplots showing the distribution of the considered sets of thermal parameters (k and ω) of the four most significant tissues in the ROI (i.e., muscle (M), fat + SAT (F), skin (S) and tumor (T)). The dots show the set of parameters corresponding to the baseline values (a), and two target sets, $\boldsymbol{\xi}_1$ (b) and $\boldsymbol{\xi}_2$ (c). (d-f) Temperature maps obtained from steady-state bioheat equation, displayed on the xy (upper row) and the yz (lower row) planes passing through the tumor at its centroid, corresponding to: (d) the baseline set of parameters $\boldsymbol{s}_{base}$; (e) the target set $\boldsymbol{\xi}_1$; (f) the target set $\boldsymbol{\xi}_2$. 68

6.6 visualization of the reconstruction error for two target maps and different number of points along the catheter. (a) The phantom Duke employed to simulate an HT treatment; the insets show the tumor target position T1 (highlighted in green). (b) Different configurations of the acquisition points $\boldsymbol{q}_\ell$ in the transversal (xy) plane passing through the tumor at its centroid (showed on the baseline map); where the number of points considered are: L= 20 (case 1) and 7 (case 2). (c, d) Boxplots showing the distribution of the considered sets of thermal parameters (k and ω) corresponding to key tissues in the ROI (M = muscle, F = fat + SAT, S = skin, T = tumor); superimposed blue dots represent the combinations of parameters $\boldsymbol{\xi}_a$ of two target maps, $a = 1$ (c), $a = 2$ (d). (e) Normalized goodness function $g(\chi)$ (see Equation 6.5): rows refer to the catheter cases (b), and columns represent the target maps (c, d); the blue-dot line corresponds to the reconstruction of the target map without noise, the blue-shadow region includes 2000 realizations of the Gaussian error $f_{\mathcal{N}}$, with $\mu = \pm 0.1$°C and $\sigma = 0.2$°C, with the blue dashed line denoting the median and the dash-dotted line indicating the 95th percentile, the red-dot line expresses the discrepancy between the target field and the baseline map. 70

6.7 General validity and robustness of the proposed method. (a) Candidate catheter positions considered for the single catheter, e.g., the red one in the picture, inserted in the ROI of the anthropomorphic phantoms and used for the reconstruction. (b) Different positions of the tumor target regions in the two phantoms Duke (top) and Ella (bottom). (c-d) $L(\chi,0.95)$ where the reconstruction procedure is applied to a large number of cases, involving 1860 combinations of the target and reconstruction maps, 100 noise realizations and the two phantoms with different tumor's positions (c), and to a set of target cases that exhibit variations in the dielectric parameters, as well as in the phantom geometry (d). (e-f) $L(\chi,0.95)$ obtained at different times by considering transient reconstruction functions, the phantom Duke with the tumor in position T1, 100 noise realizations, 8 catheters configurations and two target maps: (e) $\mathcal{F}(\boldsymbol{r}, t; \text{Model1})$ and (f) $\mathcal{F}(\boldsymbol{r}, t; \text{Model2})$. 72

6.8 Piecewise linear temperature dependent perfusion model. (a) Perfusion scaling factors used for muscle, fat (+SAT), and tumor [53, 128]. (b) Simulated temperature evolution of the target map $\mathcal{F}(\boldsymbol{r}, t; \text{Model2})$ in the indicated probe points for the phantom Duke with the tumor in position T1. 73

6.9 Temperature read by the arrays of FBG sensors at the beginning (upper row) and at the end (lower row) of the heating session; the position of the different arrays on the xy plane is indicated in the upper row (right picture) and reported in Table 6.6, together with the z-coordinates of the corresponding FBG sensors. 77
6.10 Measured temperatures and simulated values corresponding to the COMSOL model that best reproduces the experimental mock-up in correspondence of the different arrays' positions ("Pos") on the xy-plane, (a) as a function of time at $z = z_t = 0$ mm, and (b) as a function of the z-coordinate at $t = t_{off} = 160$ min. 78
6.11 Reconstruction error indicating the fraction of points with an error below the threshold χ. The temperature map is reconstructed using the experimental data along each array (from 1 to 5, as indicated in the title of the different frames) and the normalized goodness function $g(\chi)$, Eq. (6.5), is evaluated in all the available points, at the end time $t = t_{off} = 160$ min (solid red-dot lines). The function $g(\chi)$ obtained by computing the error between the experiment and the ideal simulation model (dash-diamond green line) is reported for comparison, together with the envelope (gray shaded region) and the average (dashed black line) of the functions $g(\chi)$ evaluated by considering the difference between each reconstruction function and the experimental data (note that $g(\chi) = 1$, $\forall\chi$, denotes perfect reconstruction). 81
6.12 Reconstructed temperature profiles versus experimental values and ideal profiles. Temperature profiles at $t = t_{off} = 160$ min along all the available arrays at the different positions ("Pos") on the xy-plane, reconstructed by applying the CLS method using the experimental points along (a) the Array 2 , (b) the Array 4 and (c) the Array 5, where the last one is inserted in the phantom's region mimicking the human trachea. For direct comparison, the measured temperatures are also reported (black-dot line), together with the temperature profiles corresponding to the ideal simulation model (dash-dotted green line), which is the model obtained in COMSOL by directly measuring the dielectric properties of the materials used in the experiment and using heat transfer coefficients derived by fitting the model to all the available experimental data. 82

6.13 ℓ^2-norm error $h(t)$ evaluated in all the available points as a function of time. The red-dot lines report the ℓ^2-norm error $h(t)$, Eq. (6.6), computed by comparing the reconstructed temperature values and the experimental measurements in all the available points when the reconstruction is performed using the information along the Arrays from 1 to 5, at 17 time samples between the initial and final time of the heating session. The error is also reported for the ideal simulation model and the reconstruction functions (envelope and average). . . 83
7.1 (**a**) Clipping of a generic 1D function using a two-level mask, where values are confined between two thresholds th_{low} and th_{up} through smooth transitions. The distances r_t and r_h are the maximum radial distances from the tumor center that define, respectively, the boundary of the tumor region and the outer edge of the transition (gray) region. (**b**) APA mask defined on a 3D phantom: red points correspond to the tumor region where the th_{low} is applied; gray points denote the transition region where no constraints are imposed; blue points indicate the healthy region (outside the transition zone) where the th_{up} is enforced. For visualization clarity, only the boundary of the healthy region is shown in blue. 89
7.2 (**a**) Circular array of patch antennas surrounding the simple neck model immersed in the waterbolus. (**b**) Middle top view ($z = 0$ plane) of the simplified neck model with all the considered tissues. (**c**) Employed patch antenna and optimized dimensions. 93
7.3 (**a**) Pareto front generated during the APA threshold selection process, showing the trade-off between SAR confinement ($V^H_{10\%}$) and hotspot suppression ($V^H_{50\%}$). The knee point (highlighted in red) indicates the optimal point, corresponding to (th_{low}, th_{up}) = (9.08, 4.2)$\times$ 10^3 V^2/m^2. (**b**) Comparison of the $V^H_{\chi\%}$ performance across increasing $\chi\%$ for the APA (using the thresholds corresponding to the knee point) and PSO-based SAR optimization. 95
7.4 Normalized SAR maps comparison between PSO (upper row) and APA (lower row), displayed on the three canonical planes cutting the tumor sphere at its centroid. The black dashed circle indicates the tumor sphere region. The APA thresholds considered are (th_{low}, th_{up}) = $(9.08, 4.2) \times 10^3$ V^2/m^2. While both methods achieve good tumor coverage, the APA solution results in more confined SAR patterns, reducing hotspots outside the target. 98
7.5 Temperature map comparison between PSO (upper row) and APA (lower row), visualized on the three canonical planes intersecting the tumor centroid. The maps correspond to the SAR distributions shown in Fig. 7.4, obtained with $P_0 = 26$ W for PSO and $P_0 = 16$ W for APA. 99

7.6 (**a**) Circular array of patch antennas surrounding the neck of the realistic phantom Duke V3.0 [124] and immersed in the waterbolus. (**b**) Tumor target size (expressed in mm) and its position near to the larynx of Duke. (**c**) Top view of the phased array applicator surrounding the segmented phantom visualized on the xy plane; the reported number are used to index the antennas of the array; the tumor target is highlighted in green. (**d**) Employed patch antenna and optimized dimensions. 101
7.7 (**a**) Pareto front generated during the APA threshold selection process, showing the trade-off between SAR confinement ($V^H_{10\%}$) and hotspot suppression ($V^H_{50\%}$). The knee point (highlighted in red) indicates the optimal point, corresponding to $(th_{low},\ th_{up}) = (9.41,\ 5.8)\times 10^3\ \mathrm{V^2/m^2}$. (**b**) Comparison of the $V^H_{\chi\%}$ performance across increasing $\chi\%$ for the APA (using the thresholds corresponding to the knee point) and PSO-based SAR optimization. 102
7.8 Normalized SAR maps comparison between PSO (upper row) and APA (lower row), displayed on the three canonical planes cutting the tumor sphere at its centroid. The black dashed line indicates the contour of the target tumor. The APA thresholds considered are $(th_{low},\ th_{up}) = (9.41, 5.8) \times 10^3\ \mathrm{V^2/m^2}$. While both methods achieve good tumor coverage, the APA solution results in more confined SAR patterns, reducing hotspots outside the target. 103
7.9 Temperature map comparison between PSO (upper row) and APA (lower row), visualized on the three canonical planes intersecting the tumor centroid. The maps correspond to the SAR distributions shown in Fig. 7.8, obtained with $P_0 = 60$ W for PSO and $P_0 = 44$ W for APA. Thanks to better energy focusing, APA achieves comparable tumor heating with lower input power, while also reducing the presence of hotspots in healthy tissues. 104

Chapter 1

Overview

The research work reported in this thesis has been focused on the design and implementation of simulation-guided Hyperthermia treatments (HT). This overview outlines the general framework of the research; HT refers to the process of temperature increment of certain tissues to a range of 40-44°C, often used as a complementary treatment in cancer therapy demonstrating significant radio-, chemo- and immuno-sensitizing effects [1].

Chapter 2 provides an introduction to hyperthermia cancer therapy, presenting an overview of thermal therapies, the current state of hyperthermia, and the governing physics behind HT treatments. The section also discusses hyperthermia treatment planning (HTP), temperature monitoring techniques (both invasive and non-invasive), and the challenges and future directions in the field.

Chapter 3 details an experimental testbed designed to replicate an HT treatment in the head and neck (H&N) region, together with its digital twin developed in COMSOL Multiphysics. In addition, it describes the fabrication of tissue-mimicking phantoms and the characterization of their dielectric and thermal properties for experimental validation.

Chapter 4 focuses on Specific Absorption Rate (SAR)-based optimization, a key component in improving HT treatment efficiency. It reviews state-of-the-art techniques, introduces a joint optimization approach, and presents examples of applications, including experimental validation against real-world testbeds.

Chapter 5 investigates the effect of blood flow in major vessels on temperature distribution during H&N HT treatments, providing insights into their role in achieving precise thermal control.

Chapter 6 introduces a real-time 3D temperature reconstruction method, which integrates computational models with sparse thermometry data, providing accurate temperature estimates across the entire region of interest during treatment. Validated both in a fully anthropomorphic in-silico scenario, and in an experimental controlled setting, this approach demonstrates strong potential as a low-cost and minimally invasive monitoring strategy for clinical HT treatments.

Chapter 7 presents a deterministic framework for SAR-based optimization in microwave hyperthermia, introducing the Alternating Projections Algorithm (APA) as an efficient alternative to conventional meta-heuristic methods and demonstrating its ability to enhance tumor targeting while reducing hotspots in healthy tissue.

Finally, in Chapter 8, a summary of the main achievements of this research work is given, along with possible future developments and improvements.

Chapter 2

Hyperthermia cancer therapy

Over the past two decades, there has been a growing interest in hyperthermia (HT) due to its promising role in cancer treatment. Several clinical trials have demonstrated that when hyperthermia is combined with radiotherapy or chemotherapy, it can achieve comparable clinical outcomes while requiring lower doses of radiation or chemotherapeutic drugs (or improved clinical outcomes using the same radio- or chemo-dose) [1]. This dose reduction is particularly beneficial, as it helps minimize toxicity and side effects, which are major concerns in conventional cancer therapies [2, 3]. More recently, hyperthermia has also been investigated in combination with immunotherapy [4] and gene therapy [5], where it has been reported to enhance or activate therapeutic efficacy. Moreover, clinical evidence shows that HT used in combination with conventional cancer treatments significantly enhances tumor response and improves patient survival rates [6, 7, 8, 9]. In addition, microwave hyperthermia employs non-ionizing radiation, ensuring that additional radiation-induced toxicity is not introduced. This makes it an attractive approach for improving cancer treatment efficacy while maintaining patient safety.

2.1 Thermal therapies: overview

Thermal therapies have been utilized in medicine for centuries, with historical examples in Indian, Roman and Greek civilization highlighting the therapeutic benefits of heat [1]. The primary goal of these treatments is to achieve optimal clinical outcomes while preserving healthy tissues.

The ability to regulate and maintain temperatures—both above and below physiological levels—has led to diverse medical applications, including cryoablation for tumor destruction, rheumatic disease treatment, hyperthermia for oncology, and thermal surgery.

Different thermal therapies vary in terms of target temperature, treatment duration, and biological effects:

- **Thermal Ablation:** Involves heating tissues above 60°C for 5–15 minutes, leading to protein denaturation and membrane rupture. This method effectively destroys cancerous tissue, which is later cleared by macrophages [10, 11]. A similar outcome can be achieved through cryoablation, which operates at approximately −75°C [12].
- **Diathermy:** Commonly used in physiotherapy, this technique applies moderate heat up to 41°C for 5 to 20 minutes across multiple sessions, promoting muscle relaxation and pain relief [13].
- **Hyperthermia:** Utilizes temperatures between 40–44°C for prolonged periods (around 60 minutes). Unlike thermal ablation, hyperthermia does not induce direct tissue destruction but instead enhances the effectiveness of radiotherapy, chemotherapy and immunotherapies over multiple treatment sessions.

It is important to note that these classifications are not rigid, as treatment temperatures and durations may vary across studies and clinical protocols. However, the 40–44°C range for hyperthermia is widely accepted in the medical community, particularly following guidelines established by the European Society for Hyperthermic Oncology (ESHO) [14].

2.2 Hyperthermia: state of the art

Microwave hyperthermia utilizes electromagnetic waves in the 300 MHz–3 GHz frequency range to induce localized heating within biological tissues. Compared to radiofrequency (RF) and ultrasound hyperthermia, microwave (MW) offer better penetration depth and more precise energy deposition [15].

The heating process is governed by the Specific Absorption Rate (SAR), which quantifies the rate of electromagnetic energy absorption in tissues. The efficacy of microwave hyperthermia depends on various factors, including tissue dielectric and thermal properties, applicator design, and treatment optimization.

Microwave hyperthermia systems employ different applicator configurations:

- Whole-body hyperthermia: Uses high frequencies (200–375 MHz) and involves raising systemic temperatures to 38.5–40.5°C for more than 3 hours or 40.5–42°C for 1–2 hours.
- Superficial hyperthermia: Operates at 400–1000 MHz for localized heating of tumors near the skin surface.

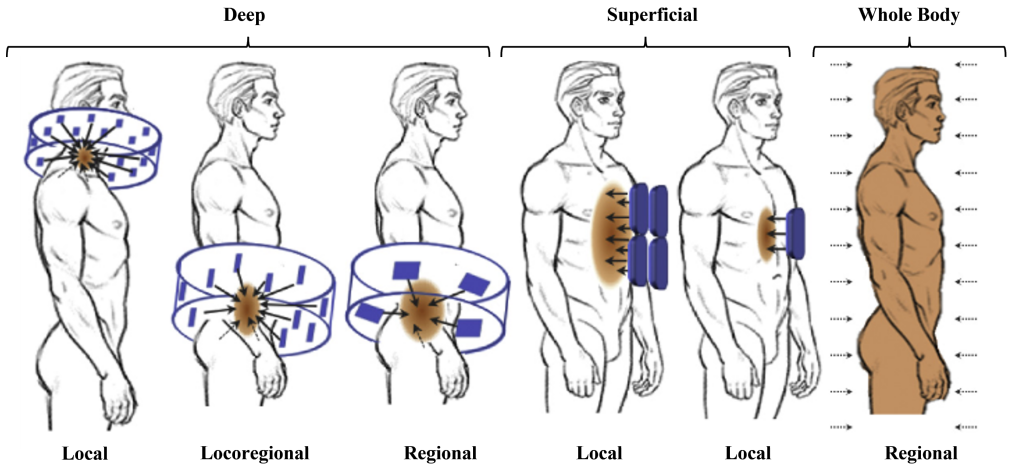

Figure 2.1: The different types of Electromagnetic-Based Hyperthermia Techniques [15].

- Deep hyperthermia: Uses frequencies below 100 MHz (regional), 100–300 MHz (loco-regional), or 300–1000 MHz (local) for targeted heating of deep-seated tumors, often via phased-array antenna systems.

To improve radiation coupling and control of the heating spots, microwave hyperthermia systems commonly include a waterbolus. This device serves a dual role: enhancing electromagnetic coupling between the applicator and the patient's body while simultaneously protecting superficial tissues from overheating. By reducing the electromagnetic impedance mismatch between the antennas and the biological tissues—since the relative permittivity of water is much closer to that of tissues

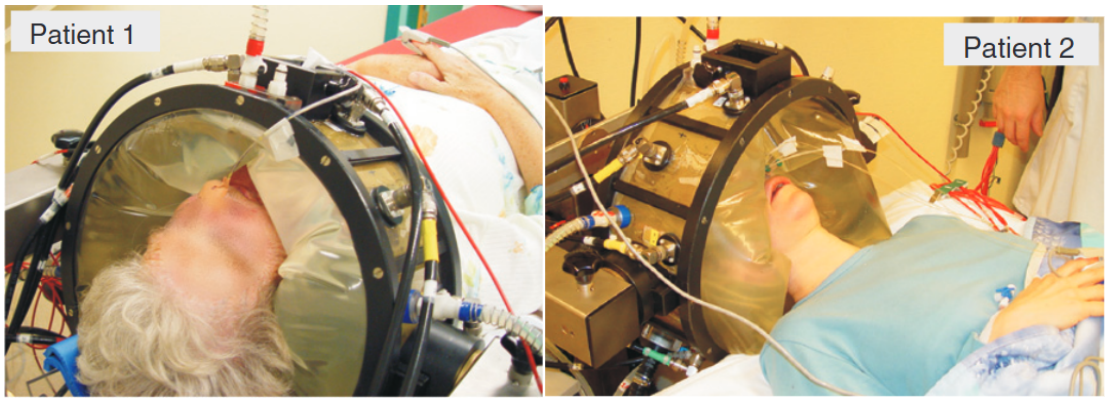

(a) (b)

Figure 2.2: Clinical integration of the HYPERcollar hyperthermia applicator in two patients with tumors located in the (a) oropharynx and (b) nasopharynx/nasal cavity [16]. The waterbolus, visible between the applicator and patient's neck/head, improves electromagnetic coupling and provides surface cooling.

than to that of air—the water bolus lowers reflection losses and improves the efficiency of power delivery to deeper tumor regions [17]. Incorporating a waterbolus into phased-array applicator design leads to improved focusing performance and more predictable field distributions across heterogeneous tissues [18]. Furthermore, by circulating water at controlled temperatures (typically 20–30 °C), the bolus provides effective surface cooling, preventing skin damage and enabling the safe application of higher power levels. Overall, the waterbolus is an essential component for achieving both efficient energy transfer and patient safety in clinical hyperthermia treatments (see Fig. 2.2).

2.3 Governing Physics

In order to clarify the physical principles underlying microwave hyperthermia, we briefly recall the standard mechanisms of electromagnetic (EM) energy deposition in biological tissues [19, 20].

The interaction of microwave fields with biological tissue is typically investigated using a macroscopic model including two key parameters: the relative permittivity ε_r (unitless) and the effective electrical conductivity σ (units of S/m) [21]. The relative permittivity describes the ability to polarize a material subjected to an applied EM field [15]. The effective electrical conductivity embodies all electrical losses in the material due to the currents driven by the EM field, as formalized in well-known macroscopic tissue models (e.g., Cole–Cole, Gabriel-Gabriel models) [22, 23, 24, 25]. Both ε_r and σ are strongly frequency- and tissue-dependent, with comprehensive datasets available in the IT'IS database [26]. The dielectric properties of tumor tissue differ from those of normal tissue, reflecting changes in tissue composition and structure [27, 28, 29].

It is worth noting that the dielectric properties typically used in numerical hyperthermia studies—usually taken from the IT'IS database [26]— are measured ex-vivo and may differ from the actual in-vivo values due to physiological variability, temperature dependence, and patient-specific factors. For this reason, several techniques have been proposed to retrieve in-vivo permittivity and conductivity distributions directly from electromagnetic measurements, thereby reducing reliance on tabulated ex-vivo data. Examples include quantitative electrical-property imaging from amplitude-only data [30] and segmented contrast-source inversion approaches for effective property mapping [31]. Although these methods lie beyond the scope of this thesis, they represent complementary strategies that could enhance future patient-specific hyperthermia treatment planning.

2.3.1 Maxwell's Equations

Maxwell's equations describe the fundamental behavior of electromagnetic fields and govern the interaction between electromagnetic waves and biological tissues. In vacuum, they are expressed as [32]:

$$\nabla \cdot \boldsymbol{\mathcal{E}}(\boldsymbol{r},t) = \frac{\rho}{\varepsilon_0}, \tag{2.1}$$

$$\nabla \cdot \boldsymbol{\mathcal{H}}(\boldsymbol{r},t) = 0, \tag{2.2}$$

$$-\nabla \times \boldsymbol{\mathcal{E}}(\boldsymbol{r},t) = \mu_0 \frac{\partial \boldsymbol{\mathcal{H}}(\boldsymbol{r},t)}{\partial t}, \tag{2.3}$$

$$\nabla \times \boldsymbol{\mathcal{H}}(\boldsymbol{r},t) = \varepsilon_0 \frac{\partial \boldsymbol{\mathcal{E}}(\boldsymbol{r},t)}{\partial t} + \boldsymbol{\mathcal{J}}(\boldsymbol{r},t). \tag{2.4}$$

where ε_0 and μ_0 denote the permittivity and permeability of free space, respectively; ρ is the charge density ($\mathrm{C/m^3}$); and $\boldsymbol{\mathcal{E}}$ ($\mathrm{V/m}$), $\boldsymbol{\mathcal{H}}$ ($\mathrm{A/m}$), and $\boldsymbol{\mathcal{J}}$ ($\mathrm{A/m^2}$) are the time-harmonic electric field, magnetic field, and current density at position $\boldsymbol{r}$ and time t.

In biological tissues, which behave as lossy dielectric media, the power dissipation per unit volume due to time-harmonic fields is represented by [33]:

$$\frac{dp_{diss}}{dV} = \boldsymbol{\mathcal{E}}(\boldsymbol{r},t) \cdot \boldsymbol{\mathcal{J}}(\boldsymbol{r},t), \tag{2.5}$$

To simplify the analysis, we express time-harmonic fields in their complex phasor form as $\boldsymbol{\mathcal{E}}(\boldsymbol{r},t) = \Re\{\boldsymbol{E}(\boldsymbol{r})e^{j\omega t}\}$ and $\boldsymbol{\mathcal{J}}(\boldsymbol{r},t) = \Re\{\boldsymbol{J}(\boldsymbol{r})e^{j\omega t}\}$, where $\omega = 2\pi f$ is the angular frequency of operation. Substituting these expressions into (2.5) and taking the time average over one period $T = 1/f$, the average power dissipated per unit volume becomes:

$$\left\langle \frac{dp_{\mathrm{diss}}}{dV} \right\rangle_T = \frac{1}{2}\Re\{\boldsymbol{E}(\boldsymbol{r}) \cdot \boldsymbol{J}^*(\boldsymbol{r})\}. \tag{2.6}$$

By introducing the macroscopic constitutive relation $\boldsymbol{J} = \sigma\,\boldsymbol{E}$ (with effective conductivity σ), the expression in (2.6) simplifies to [21]:

$$\left\langle \frac{dp_{\mathrm{diss}}}{dV} \right\rangle_T = \frac{1}{2}\sigma(\boldsymbol{r})\,|\boldsymbol{E}(\boldsymbol{r})|^2\,, \tag{2.7}$$

The quantity in (2.7) is the volumetric heat source ($\mathrm{W/m^3}$) generated by EM absorption and we denote it with Q_{EM}:

$$Q_{EM}(\boldsymbol{r}) = \frac{1}{2}\sigma(\boldsymbol{r})|\boldsymbol{E}(\boldsymbol{r})|^2. \tag{2.8}$$

The convention adopted in Equation (2.8) assumes complex peak phasors; when RMS fields are used, the prefactor 1/2 is omitted.

A metric widely adopted in MW hyperthermia [21] is the specific absorption rate (SAR) (units of W/kg) which quantifies the rate at which the EM energy is absorbed per unit mass of tissue [34]), defined as:

$$\mathrm{SAR}(\boldsymbol{r}) = \frac{Q_{EM}(\boldsymbol{r})}{\rho(\boldsymbol{r})}, \tag{2.9}$$

so that:

$$\mathrm{SAR}(\boldsymbol{r}) = \frac{1}{2}\frac{\sigma(\boldsymbol{r})}{\rho(\boldsymbol{r})}|\boldsymbol{E}(\boldsymbol{r})|^2, \tag{2.10}$$

where ρ (kg/m^3) is the tissue mass density, at position vector $\boldsymbol{r}$.

2.3.2 Bioheat Equation

As common in hyperthermia literature, the rise in tissue temperature caused by the absorption of EM energy can be described using Pennes' bioheat equation (PBHE) [35]. The *time-dependent* form of the equation is given by:

$$\rho C_p \frac{\partial T}{\partial t} = \boldsymbol{\nabla} \cdot (k\boldsymbol{\nabla} T) - \rho_b C_{p,b} \omega \rho (T - T_a) + Q_{met} + Q_{EM}, \tag{2.11}$$

where, k (W/m/°C) is the tissue thermal conductivity, $\rho_b = 1060$ kg/m^3 and $C_{p,b} = 3890$ J/kg/°C are the volume density and specific heat capacity of blood, $T_a = 37$°C is the arterial blood temperature, and ω (ml/min/kg) is the tissue volumetric blood perfusion rate. Moreover, Q_{EM} is the EM heat source related to SAR (Equation (2.9)) and Q_{met} is the metabolic heat generation term. Q_{met} can be neglected in local hyperthermia because, within the limited heated volume, it contributes orders of magnitude less power than Q_{EM}, whereas in whole-body hyperthermia it must be retained since it contributes to a significant fraction of the total heat and influences the global energy balance. Throughout this thesis, Q_{met} is neglected, and the term bioheat equation refers to Eq. 2.11 in its general form, while the *steady-state* bioheat equation implies that the time-dependent term ($\frac{\partial T}{\partial t}$) is neglected. Conversely, when referring to the absence of a bioheat contribution, we mean that the last term in Eq. 2.11 (i.e., $\rho_b C_{p,b} \omega \rho (T - T_a)$) is omitted. In this case, the equation is referred to as the *heat equation*.

While PBHE is widely adopted for treatment planning due to its simplicity, more detailed models (e.g., discrete vasculature models [36]) provide improved accuracy but remain computationally demanding.

In summary, tissue heating under MW exposure arises from fundamental electrodynamic principles: effective conductivity captures both conduction and dielectric losses in a macroscopic sense. The SAR metric provides the standard bridge (coupling) between EM fields and thermal response, and—combined with bioheat

modeling—constitutes the accepted theoretical foundation for clinical hyperthermia.

2.4 Hyperthermia Treatment Planning and Optimization

Although clinical results show promise, achieving the desired optimal thermal dose of 43°C for an hour-long HT treatment is often hindered by hotspots in normal tissues, which prevent the further increase of total power, impacting the ability to reach the targeted thermal dose. Thus, maintaining precise temperature control during HT treatment becomes evident, underscoring the importance of hyperthermia treatment planning (HTP). As outlined in clinical Quality Assurance Guidelines, the HTP workflow encompasses several critical steps [37, 38] (see Figure 2.3 for an overview):

1. Acquisition of CT or MRI images with the patient in the treatment position.
2. Creation of a full 3D patient model through manual, semi-automatic, or automatic segmentation of different tissue types.
3. The segmented patient model and a 3D model of the applicator are virtually inserted into an electromagnetic simulation software based on the Finite Element (FEM) or Finite-Difference Time-Domain (FDTD) methods.
4. Tissue-specific electromagnetic and thermal parameters are assigned to the individual tissues.
5. The phase and amplitudes of the antennas in the applicator are optimized (through SAR- or Temperature-based optimization) to focus the heat in the tumor target volume, while avoiding overheating of surrounding healthy tissues.
6. Closed-tip thermometry catheters are placed interstitially, intraluminally, and/or on the skin.
7. A CT scan is performed to accurately document the locations of the catheter tracks.
8. In the hyperthermia treatment room, the patient is positioned according to the planned alignment with the microwave applicator.
9. Optical thermometry fibers are inserted into the interstitial and intraluminal catheters.

10. Additional thermometry probes are placed on the skin and at the inflow and outflow of the waterbolus.

11. The waterbolus is filled with demineralized water, which is circulated at a temperature in the range of 20–30°C.

12. The optimized phase and amplitudes are applied to the hyperthermia system unit during the treatment session.

13. Power is stopped if temperature probes indicate the tolerance limit has been reached or if the patient experiences pain.

14. If the procedure is halted due to a suspected hotspot, further evaluation and adjustment (possibly reoptimizing the antenna) are performed before continuing.

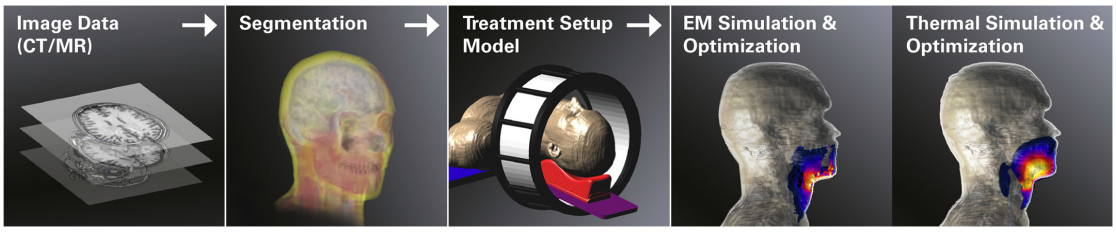

Figure 2.3: Hyperthermia Treatment Planning Stages [39].

2.5 Temperature Monitoring in HT

As mentioned in the previous section, during hyperthermia treatments, temperature monitoring is crucial for ensuring treatment efficacy and minimizing thermal damage to surrounding healthy tissues. Several thermometric techniques have been investigated, but most are still under research and not yet established in routine clinical practice. These approaches can be broadly classified into non-invasive and invasive methods, each with specific advantages and limitations.

2.5.1 Non-Invasive Thermometry Methods

Non-invasive thermometry techniques measure temperature indirectly by analyzing tissue properties affected by heat. The most well-known approaches are based on Magnetic Resonance (MR), Computed Tomography (CT), Ultrasound (US), and Infrared (IR) imaging [40]. Although promising, these methods are not yet mature enough to be considered standard in clinical hyperthermia treatments.

MR thermometry, for example, is an evolving field but suffers from several limitations: it currently provides only relative temperature changes rather than absolute values, is hampered by field heterogeneity, subject to inaccuracies in the presence of (e.g., respiratory) motion, and has difficulties measuring in fatty tissues. Widespread application of MR thermometry is also limited by the high cost of operating MRI scanners, their scarce availability, and the challenges involved in applying thermal therapies inside an MRI system. CT thermometry having the same limitation of MR thermometry is additionally limited by ionizing radiation exposure, making it unsuitable for long-duration HT sessions. IR imaging, on the other hand, is restricted to superficial temperature assessment and is mainly used for laboratory studies rather than in vivo applications. US thermometry, which estimates temperature changes based on variations in acoustic properties, offers real-time monitoring and thus potential guidance for HT treatments, but its effectiveness is limited by poor penetration depth and sensitivity to motion artifacts.

2.5.2 Invasive Thermometry Methods

On the other hand, invasive methods, which are significantly more cost-effective than imaging systems, require direct sensor insertion into the target tissue. The most commonly used sensors include [40, 41]:

- **Thermistors**: Low-cost resistive temperature sensors with high sensitivity in the clinical temperature range and typical accuracies of approximately 0.1–0.2°C. However, thermistors provide only point measurements and may be affected by self-heating and electromagnetic interference in microwave hyperthermia [42].
- **Thermocouples**: Inexpensive and fast-responding (<1°C accuracy, response time <1s). However, they provide only point measurements and are susceptible to electromagnetic interference, which may lead to errors in microwave hyperthermia. With proper material selection and coatings, thermocouples can also be made biocompatible for medical use.
- **Fiber Optic Sensors (FOSs)**: Unlike thermocouples, FOSs are immune to electromagnetic interference and have low thermal conductivity. Two main types are commonly used in hyperthermia applications:
  - **Fiber Bragg Grating sensors (FBGs)**: Measure temperature variations through changes in reflected light wavelength [43].
  - **Fluoroptic sensors**: Use fluorescence decay time to determine temperature, offering high precision (∼0.3°C) [44].

  - **Gallium arsenide (GaAs) bandgap sensors**: Measure temperature through shifts in the optical absorption edge and provide high accuracy and stability in microwave hyperthermia [45].

While non-invasive methods are appealing due to their ability to measure temperature without physical contact, their clinical implementation remains limited by cost, accessibility, and accuracy. In contrast, invasive techniques, particularly FOS probes encased in closed-tip catheters, provide highly accurate and localized measurements, making them the preferred choice for real-time temperature monitoring in clinical hyperthermia treatments. However, the accurate thermometry information is strictly limited to a scarce number of point and the insertion locations, and their use must be reduced to the bare minimum to avoid severe treatment-related morbidities. Furthermore, encasing temperature sensors within closed-tip catheters introduces a thermal response delay and a measurement offset due to the catheter material and geometry. These effects can be characterized and compensated through calibration procedures, although the presence of the catheter may slightly perturb the local temperature distribution in surrounding tissue. In particular, under uniform temperature conditions, the catheter does not distort the temperature distribution, whereas any induced error becomes more relevant in the presence of thermal gradients [46, 47].

Ultimately, the choice of thermometry method depends on factors such as the treatment modality, available equipment, and the clinical setting.

2.6 Challenges and Future Directions

Despite significant advancements, microwave hyperthermia still faces several challenges that limit its widespread clinical adoption. These challenges can be broadly categorized into technological, physiological, and clinical aspects.

- **Temperature Monitoring:** Accurate real-time thermometry remains a challenge. While MR thermometry offers high-resolution temperature mapping, its high cost, complexity (dedicated radiologist and technical person), logistics, motion sensitivity, and limited availability hinder routine clinical use. Invasive thermometry, such as fiber optic sensors, provides localized temperature measurements but lacks comprehensive spatial coverage.

- **Energy Deposition and Control:** Achieving precise and homogeneous heating in deep-seated tumors requires advanced applicator designs and real-time feedback mechanisms. The interaction of microwaves with heterogeneous tissue structures, variations in perfusion, and patient-specific anatomical differences complicate treatment planning.

- **Treatment Optimization:** Personalized HTP is crucial to maximize therapeutic efficacy. Current HTP methods rely on electromagnetic and thermal simulations, but these require further refinement to accurately predict temperature distributions in real time.

Future research should address the current lack of methods capable of providing reliable, real-time temperature maps across the entire treated region—a limitation that affects not only hyperthermia but all thermal therapies. Invasive thermal probes remain the clinical standard due to their high accuracy, yet they only provide information at a very limited number of points and locations and their use must be minimized to reduce patient discomfort and treatment-related morbidities. On the other hand, simulations can deliver the required spatial information but cannot be fully relied on for temperature monitoring. Their large uncertainties in tissues' dielectric and thermal properties, which vary between patients and even during treatment. Alternative non-invasive techniques, such as MR thermometry, are still confined to the research stage and rely on expensive, complex equipment not easily applicable to HT routine clinical workflows. These limitations clearly underline the need for novel approaches that can deliver accurate and spatially resolved temperature map in real time, thereby enabling safer and more effective clinical hyperthermia treatments.

Chapter 3

Experimental Setup and Numerical Modeling for Microwave Hyperthermia

3.1 Introduction

To validate new methods for hyperthermia application under controlled and reproducible conditions, a realistic physical benchmark model and its corresponding numerical counterpart are therefore required. This chapter presents the development and validation of a tissue-mimicking phantom for microwave hyperthermia in the Head and Neck (H&N) region and its integration into an experimental testbed. It then describes the implementation of a corresponding digital twin in COMSOL Multiphysics [48], providing a simulation environment to complement and validate the experimental setup. The overall objective is to establish a controlled research framework that enables precise heating localization and supports treatment optimization.

The chapter is organized as follows:

- **Section 3.2** describes the tissue-mimicking H&N phantom, including material composition, preparation process, and dielectric/thermal property characterization.
- **Section 3.3** details the experimental setup and its digital twin, describing the phantom implementation in a physical experimental testbed and its corresponding simulative counterpart in COMSOL Multiphysics.

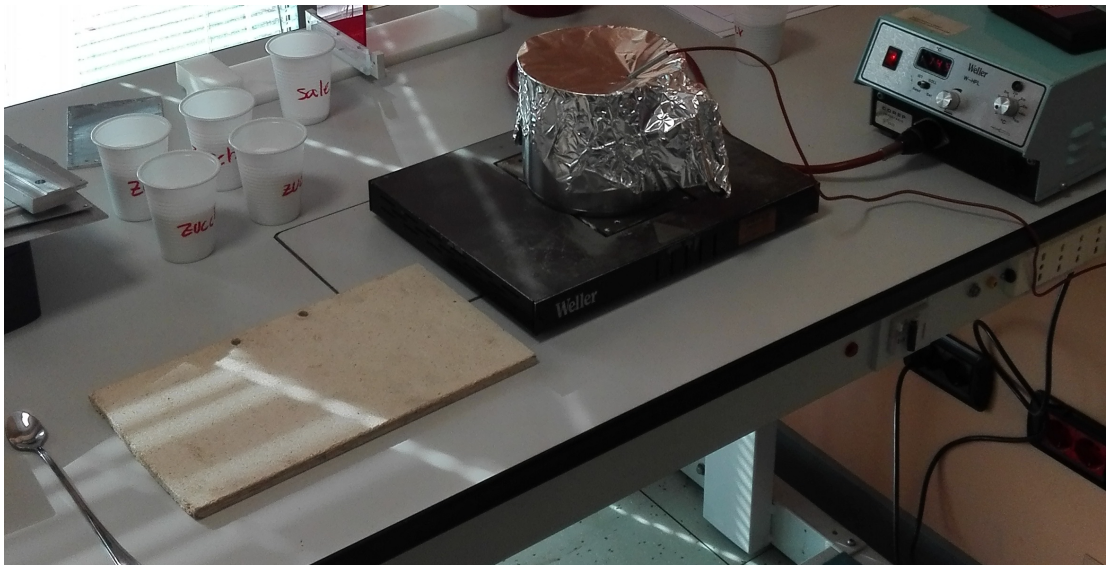

Figure 3.1: Preparation of the semi-solid agar mixture using an electric hotplate and a temperature probe.

3.2 Tissue-Mimicking Phantom Development

This section highlights the key findings presented in the IEEE International Symposium on Antennas and Propagation and ITNC-USNC-URSI Radio Science Meeting [49].

The development of new medical devices and techniques requires performing tests with physical anatomically realistic tissue mimicking materials (TMMs), without risk to animals or humans [50]. To this purpose, a plethora of different phantom recipes has been developed for distinct medical applications, to mimic the dielectric properties of tissues in the frequency range of interest according to the values reported in specific databases [26, 51].

One of the medical context requiring the use of phantoms for applicator design and testing is microwave hyperthermia. This work is focused on the development of an easily reproducible, inexpensive, semi-solid phantom, used to estimate in a physical scenario the thermal dose delivered to a tumor target by means of a hyperthermia antenna array applicator surrounding the phantom. The recipe reported in [52] was slightly modified to create an agar-based phantom with repeatable density, thermal and dielectric properties similar to those of human muscle tissue at 434 MHz, for reliable temperature measurements with fiber optic sensors. This choice is motivated by the fact that the neck is predominantly composed of muscle and soft tissues; therefore, when patient-specific imaging and detailed tissue composition are unavailable, assuming muscle-like properties for the healthy background is a practical and reasonable approximation.

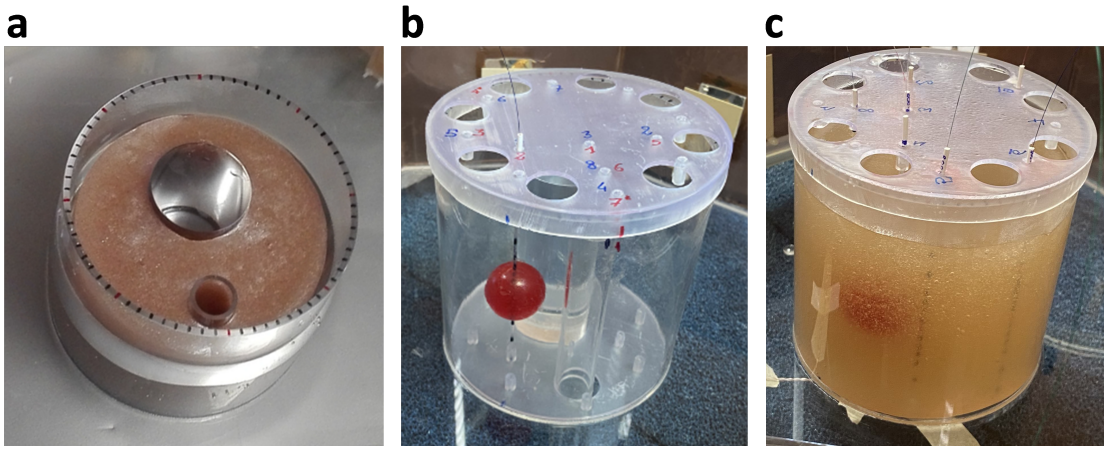

Figure 3.2: a: Neck phantom container with the agar-based phantom; b: target sphere representing the tumor; c: view of the complete neck phantom with the tumor target inside.

3.2.1 Preparation method

The ingredients and the proportions by weight used to create the semi-solid TMM employed in our experiments are: demineralized water ($\varepsilon_r = 79.53$, $\sigma = 0.05$ S/m) (58.44%), agar-agar powder (5%), sugar (35%), salt (NaCl) (1.4%) and some drops of disinfectant solution (0.16%) (we used Amuchina 100%®). After heating the water to 90°C (see Figure 3.1), the pot is removed from the heat source and the agar-agar powder is mixed in. Then, while stirring continuously, the pot is repositioned on the heating source, and the sugar and salt are added. When the mixture becomes smooth and without lumps, it is removed from heat and the disinfectant drops are introduced to the mixture. After pouring it into the neck-shaped container (Figure 3.2a), the phantom solidifies quickly. The reported proportions have been determined after several refinements with the aim of reproducing the dielectric parameters reported in [53].

To simulate the presence of a tumor target with a different electrical conductivity (see Figs. 3.2b,c) (strongly increased to stress the difference with respect to the surrounding medium), it was simply necessary to increase the quantity of salt from 1.4% to 2.83%. A few drops of red food coloring were then added for visualization purpose, without altering the dielectric properties of the mixture.

3.2.2 Characterization

Tables 3.1 and 3.2 report the estimations of the relative permittivity (ε_r) and the electrical conductivity (σ) measured during different experimental sessions in which the finalized phantom recipe was prepared to perform hyperthermia experiments. In each session, the measurement of the parameters was repeated N times;

Table 3.1: Dielectric properties of the main phantom at $f = 434$ MHz evaluated with the Method 1 during different experimental sessions

Session	$\bar{\epsilon}_r$ (-)	SDOM$_{\epsilon_r}$	$\bar{\sigma}$ (S/m)	SDOM$_\sigma$ (S/m)
Feb ($N = 11$)	58.04	0.64	0.86	0.02
Jun ($N = 13$)	59.81	1.08	1.10	0.05
Jul ($N = 6$)	57.70	0.85	0.99	0.04
Weighted average	58.16 ± 1.29		0.95 ± 0.05 S/m	

Table 3.2: Dielectric properties of the main phantom at $f = 434$ MHz evaluated with the Method 2 during different sessions

Session	$\bar{\epsilon}_r$ (-)	SDOM$_{\epsilon_r}$	$\bar{\sigma}$ (S/m)	SDOM$_\sigma$ (S/m)
Jun ($N = 2$)	59.84	3.25	0.86	0.11
Jul ($N = 8$)	58.88	1.20	0.88	0.03
Aug ($N = 10$)	57.41	0.57	0.87	0.02
Weighted average	57.99 ± 1.49		0.87 ± 0.05 S/m	

Table 3.3: Dielectric and thermal properties of the implemented phantoms

Material	ϵ_r (-)	σ (S/m)	ρ (kg/m^3)	k (W/m°C)	C_p (kJ/kg°C)
Literature	59[53]	0.89[53]	1090 ± 23[26]	0.49 ± 0.01[26]	3.42 ± 0.21[26]
Neck phantom	58.09 ± 0.98	0.91 ± 0.04	1138.27 ± 3.56	0.50 ± 0.01	3.20 ± 0.07
Tumor target	58.73 ± 0.06	1.568 ± 0.004	-	-	-

the best estimate was evaluated as the average value and the error as standard deviation of the mean (SDOM). The measurements reported in Table 3.1 were carried out using a Keysight ® open-ended coaxial probe, and analyzing the resulting reflection coefficients using the Marsland–Evans simplified solution (Eq. (5) in [54]) under the three calibration configurations (short circuit, open in air, and probe in water) (Method 1). Table 3.2 reports instead the measurements performed using a commercial dielectric probe (Method 2) [55]. The dielectric properties of the phantom evaluated with the two methods are then computed as weighted averages. A further weighted average is performed between the two methods to provide the final estimations reported in Table 3.3.

Table 3.3 also reports an estimation of the volume density of the agar neck phantom, performed using three equal square samples with known mass and volume. Finally, the thermal conductivity (k) and the heat capacity (C_p) reported in Table 3.3 were each estimated using two independent methods: one implemented

at the Department of Applied Science and Technology (DISAT), Politecnico di Torino [56], and the other at the Department of Energy (DENERG), Politecnico di Torino, using the heat flux meter apparatus Lasercomp FOX600 [57]. The final values were obtained as weighted averages of the two corresponding estimates.

For the tumor target phantom, we only estimated the dielectric properties using the Method 2 [55] (see Table 3.3). Unlike the neck phantom, in this case measurements were performed within a single session, so the estimated error is relatively smaller. The computed error for the tumor dielectric properties, evaluated using 4 repeated measurements from the same experimental session, are reported in Table 3.3. A dedicated experimental characterization of the tumor target thermal properties (and density) was not performed in this study; this represents a limitation since recipe variations (e.g., added salt) may also affect these parameters, and will be addressed in future phantom iterations.

3.2.3 Results and discussion

As reported in Tables 3.1 and 3.2, the dielectric parameters measured during the different experimental sessions show an excellent agreement, highlighting the strong reproducibility of the considered phantom. Furthermore, as shown in Table 3.3, the estimated values show a satisfactory alignment with the literature values we aimed to reproduce.

The thermal characterization, implemented with two different methods, provide thermal parameters very close to those of the muscle tissue (see Table 3.3); this is important in biomedical applications as microwave hyperthermia, where thermal parameters play a crucial role.

Finally, the considered recipe proved to be highly versatile, allowing to change the dielectric properties of the resulting phantom by simply varying the proportions of salt and sugar. It should be noted, however, that these dielectric properties are frequency-dependent; therefore, matching the targeted dielectric properties reported in the IT'IS database at the operating frequency of 434 MHz does not necessarily guarantee matching at other hyperthermia frequencies (e.g., 915 MHz) with the same phantom.

3.3 Experimental Setup and its Digital Twin

This part presents an expanded discussion of the published work presented in COMSOL conference [58].

Following the principles of Hyperthermia Treatment Planning (HTP), an experimental mock-up was developed that replicates a typical hyperthermia applicator designed for treating deep-seated and sub-superficial tumors in the head and neck (H&N) region [18, 59]. This section details the experimental testbed and its

in-silico counterpart, the so-called digital twin, implemented in COMSOL Multiphysics. The validation of the developed digital twin is detailed in the next chapter (See section 4.3).

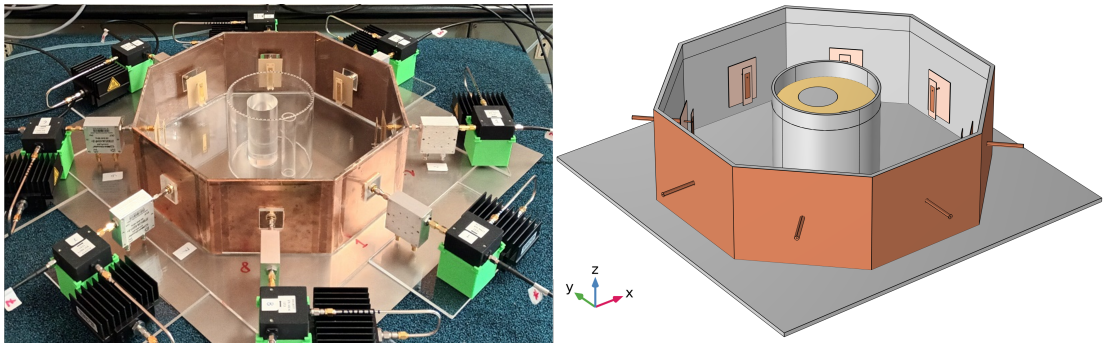

(a) (b)

Figure 3.3: (a) Experimental prototype reproducing an HT applicator for deep-seated and sub-superficial tumors in the H&N region. (b) Digital twin of the implemented mock-up developed using COMSOL Multiphysics.

3.3.1 Experimental Testbed

The experimental mock-up reproducing our HT setup is composed of four main elements: a tissue-mimicking phantom representing the human neck, a circular array of eight patch antennas as HP applicator, the electronic control system for antenna feeding, and temperature monitoring system. This experimental mock-up is demonstrated in Figure 3.3 along with its in-silico counterpart, developed in COMSOL Multiphysics, which enables detailed electromagnetic and thermal simulations for HTP.

Prototype Design

The experimental prototype consists of a Poly(methyl methacrylate) (PMMA) octagonal frame (circumradius = 20 cm, height = 12 cm) designed to hold the antenna array. This frame is positioned on a square base (side = 45 cm, thickness = 5 mm). The frame also hosts a hollow PMMA cylinder (outer diameter = 12.4 cm, inner diameter = 11.8 cm, height = 12 cm) which is placed at the center of the octagonal container and is used to model the neck of the patient.

Inside the cylinder reproducing the neck, a solid PMMA cylinder (diameter = 45 mm) and a hollow cylinder (outer diameter = 20 mm, inner diameter = 16 mm) are positioned to reproduce the presence of the spine and the trachea. In order to recreate the muscle tissues in the neck, a properly developed in-house muscle phantom which has been detailed in section 3.2, is used to fill the central cylinder (See Figure 3.1).

The space between the walls of the octagonal container and the central phantom is filled with demineralized water, which forms the so-called waterbolus [18] and acts as the coupling medium in which the patch antennas are immersed. Finally, thin copper foils cover the outside walls of the octagonal PMMA container; this metallization was introduced for practical/compatibility reasons and was included in all simulations.

The dielectric and thermal properties of the materials used in this mock-up are detailed in Table 3.4 (refer to section 3.2.2 for characterization details).

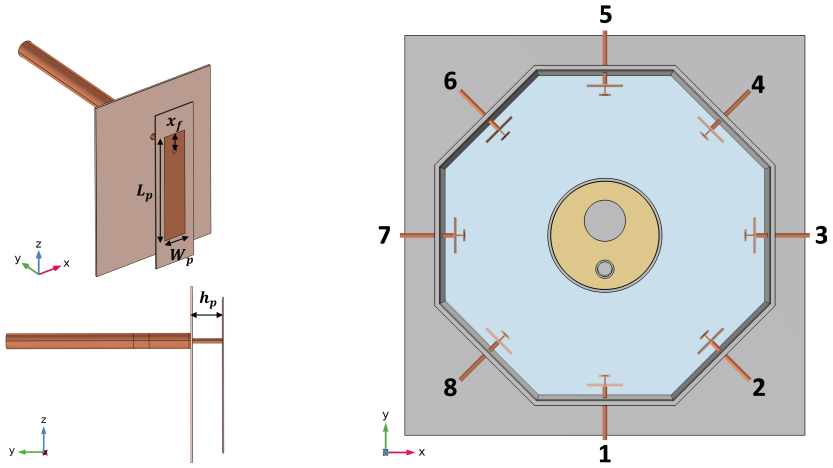

(a) (b)

Figure 3.4: (a) Perspective and side view of the designed antenna with the optimized parameters. (b) Top view of the hyperthermia mock-up simulated in COMSOL.

Antenna Array

The patch antenna forming the array was the result of an optimization and refinement procedure involving both the antenna as a single element and as part of the array. To provide a robust support for the antenna, both the ground and the patch have been printed on layers of I-Tera MT40 ($\varepsilon_r = 3.45$, $\tan\delta = 0.0031$) with thickness 0.508 mm and 0.254 mm, respectively. With reference to Figure 3.4a, the

Table 3.4: Dielectric and thermal properties of the materials used in the mock-up at $f = 434$ MHz and room at temperature.

Material	ρ (kg/m^3)	ε_r $(-)$	σ (S/m)	k (W/m°C)	C_p (kJ/kg°C)
PMMA	1410	2.33*	10^{-4}*	0.39	1.4
Water	997	79.53*	0.047*	0.6	4.18
Muscle phantom	1138.27 ± 3.56*	58.09 ± 0.98*	0.91 ± 0.04*	0.50 ± 0.01*	3.20 ± 0.07*

* Experimentally measured

length (L_p) and the width (W_p) of the patch, together with the distance of the patch from the ground (h_p) and the distance of the coaxial feed to the edge of the patch (x_f), have been optimized in CST Microwave Studio [60] using a simplified layout, where the antenna is immersed in a water domain and the phantom is replaced by two finite dielectric layers reproducing the PMMA wall of the neck container and the agar-based phantom [17]. The distance of the patch antenna from the PMMA layer was fixed to 8 cm, which is approximately twice the minimum distance at which the reflection coefficient becomes stable.

The resulting optimized parameters were found to be: $L_p = 33.85$ mm, $W_p = 7.13$ mm, $h_p = 9$ mm, and $x_f = 5.66$ mm. The antenna parameters optimized in this simplified layout have been refined by considering the antenna as part of the array in the in-silico counterpart of the prototype realized in the COMSOL (see Figure 3.4b). This refinement only resulted in increasing the distance between the antenna ground and the patch element h_p to 10.5 mm. When considering the entire mock-up, other parameters have been refined to avoid undesired reflections, such as the distance between the antenna ground and the PMMA wall, fixed at 13.5 mm.

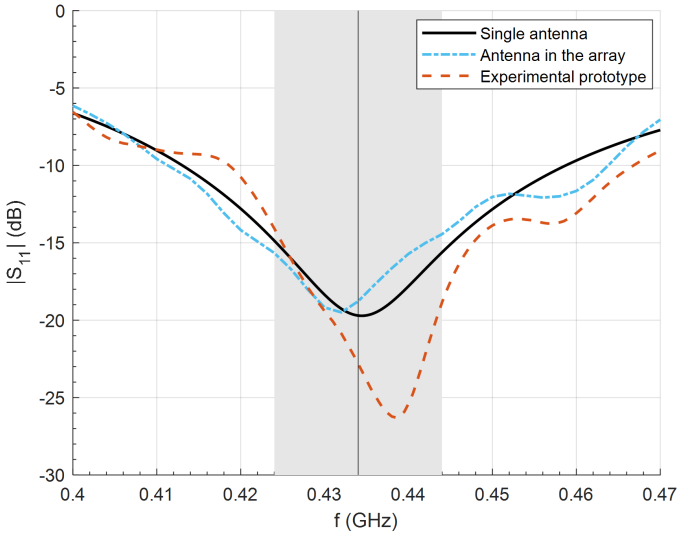

Figure 3.5: Comparison of simulated reflection coefficients for a single antenna optimized in a simplified layered scenario versus its performance as part of an 8-element array, alongside experimental measurements.

Figure 3.5 compares the curves of the reflection coefficient evaluated for the single antenna optimized in the simplified layered scenario, the antenna being part of the prototype model, and the antenna experimentally realized in the complete hyperthermia mock-up. A good agreement is observed among the different curves, and a bandwidth (-15 dB) of 20 MHz is achieved around the central frequency (434 MHz).

Electronic Setup

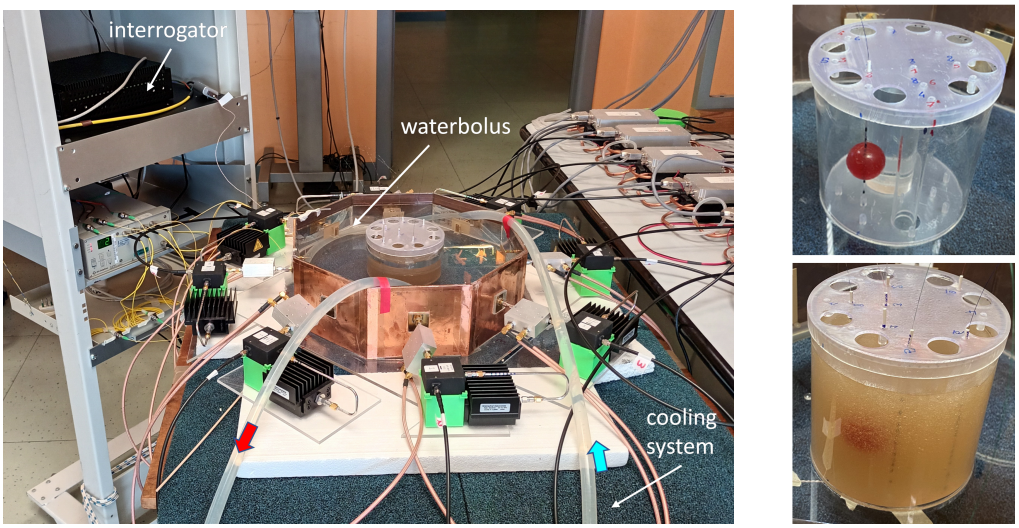

(a) (b)

Figure 3.6: (a) Overview of the complete experimental apparatus. (b) Insets showing the position of the tumor target and the FBG arrays before (*top*) and after (*bottom*) the introduction of the agar mixture reproducing the muscle tissue.

In order to effectively administer a thermal dose, the heat applied to the target region must be delivered continuously and with minimal losses [61]. To achieve this, the feeding coefficients of the antennas need to be properly optimized (this will be fully discussed in Section 4.2), then accurately delivered to the array and kept constant throughout the entire heating session, ensuring stable and efficient energy deposition in the target region. During the heating sessions of this project, this is achieved using a closed-loop electronic control system that supplies the appropriate power to each antenna while simultaneously feeding them with a constant amplitude and phase. Figure 3.6a shows the experimental prototype with part of the electronic components. The first element of the electronic chain is a signal generator (HP-Agilent/Keysight 8648A) operating at 434 MHz, whose output is connected to a 1:8 power splitter to feed the antennas of the array. The phase and the amplitude delivered to each antenna are voltage-controlled by means of a phase shifter (PS) and a voltage gain amplifier (VGA), respectively. A closed-loop electronic control system was implemented to correctly set the PS and VGA input voltages via a microcontroller unit (MCU) and a 16-bit DAC board. A dedicated power amplifier (PA) collects the low-power signal exiting each PS, amplifying it before feeding the antenna. The block diagram of the feeding network shown in Fig. 3.7. The sensing topology was selected to acquire both forward and reflected signals at a low-power directional-coupler monitoring port, which is required to compute the active

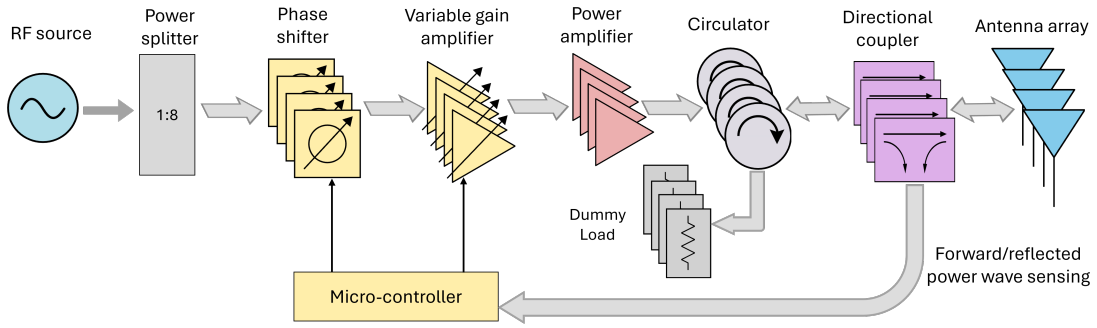

Figure 3.7: Block diagram of the antenna array feeding network. Only 4 of the 8 channels are depicted for clarity.

reflection coefficients while keeping the microcontroller isolated from high-power RF levels. Measuring reflected power at the circulator port could reduce cross-coupling under large mismatch, but would require additional protection to avoid exposing the microcontroller to high-power back-reflections. In addition, high-reflection operating conditions are discouraged by the optimization itself through the active-reflection penalty term introduced in the cost function (see eq. (4.6)).

To mitigate the temperature increase in the waterbolus due to the electromagnetic heating, the demineralized was circulated and passed through an external water-cooling radiator by means of two pipes and a pump (see the in- and outflow directions of the pipes in Figure 3.6a).

During the experimental session, a target sphere with radius $r_t = 15$ mm was introduced in the neck container before pouring the agar mixture reproducing the neck phantom (see Figure 3.6b).

Temperature Measuring Systems

To measure the temperature in the realized mock-up in different locations and in real time, a system of Fiber Optic Sensors (FOS) has been considered. In particular, we used arrays of Fiber Bragg Grating (FBG) sensors inserted in thin glass catheters (OD = 1.5 mm, ID = 1 mm) and then placed into the neck phantom to measure the temperature along the vertical axis as shown in Fig. 3.8. Table 3.5 reports the coordinates in the xy plane of the arrays numbered in Fig. 3.8a and the positions along the z-axis of the corresponding FBG sensors (Fig. 3.8b).

The Array 1 is inserted in the center of the tumor target sphere, while the Array 4 is placed in the hollow cavity of the cylinder reproducing the trachea. The sampling time-interval is 3s for the arrays 1,3, and about 12s for the arrays 2,6. To correctly position the catheters along the vertical axis, a support placed at the bottom of the neck and a cap with small hollow cylinders were purposely 3D printed. The circular holes in the cap shown in Fig. 3.8a serve to pour the agar uniformly inside the neck cylinder once the tumor target and the catheters have

Table 3.5: Coordinates of the FBG sensors along the different arrays

Array	x (mm)	y (mm)	$\boldsymbol{z}$ (mm)
1	-30	-15	$\boldsymbol{z_1}$
2	0	-15	$\boldsymbol{z_2}$
3	30	-15	$\boldsymbol{z_3}$
4	0	-37	$\boldsymbol{z_2}$

$\boldsymbol{z_1} = (30,\ 20,\ 15,\ 10,\ 5,\ 0,\ -5,\ -10,\ -20)$
$\boldsymbol{z_2} = (40,\ 30,\ 20,\ 15,\ 10,\ 5,\ 0,\ -5,\ -10,\ -15,\ -20,\ -30,\ -40)$
$\boldsymbol{z_3} = (30,\ 20,\ 10,\ 0,\ -10)$

been positioned. Temperature data were acquired and processed using the Micron Optics HYPERION si255, which is an industrial sensing interrogator that allows for rapid, full-spectrum data acquisition and visualization (see Fig. 3.6a).

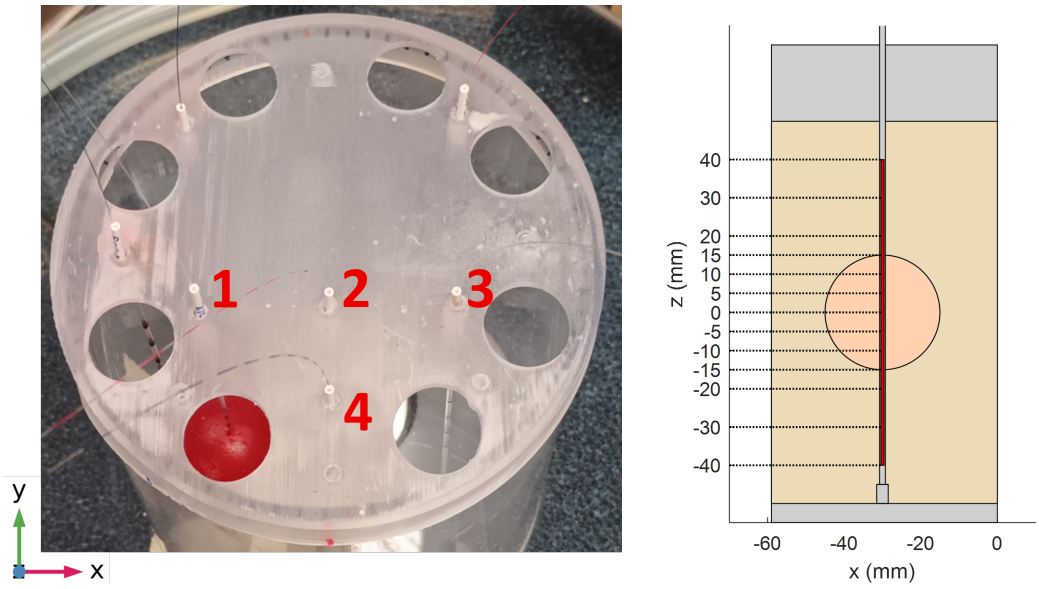

(a) (b)

Figure 3.8: (a) Positions of the arrays of FBGs on the xy plane. (b) z-coordinates of the FBGs along the arrays (the Array 1 passing through the tumor target is depicted as an example).

3.3.2 COMSOL Model

As previously mentioned, the digital twin of the constructed HT mock-up, illustrated in Figure 3.3b, was implemented in the simulation software COMSOL Multiphysics, starting with the proper design of the geometry. Later, the experimentally measured dielectric and thermal properties of the fabricated phantom [49] were integrated into the RF simulation domain. LiveLink for MATLAB was then used to optimize the antenna array coefficients, focusing power deposition (specific absorption rate, SAR) on a target sphere representing the tumor while minimizing the risk of hotspots in surrounding healthy tissue. The BioHeat Transfer (BT) Module was then used to generate the temperature distribution. This section details additional specifications regarding the simulation of the implemented HT mock-up in COMSOL Multiphysics.

Geometry and Material properties

The geometry of the simulated prototype was established in accordance to the dimensions of the physical model described in section 3.3.1. Similarly, the material properties of each component are defined in reference to their physical counterpart (See Table 3.4).

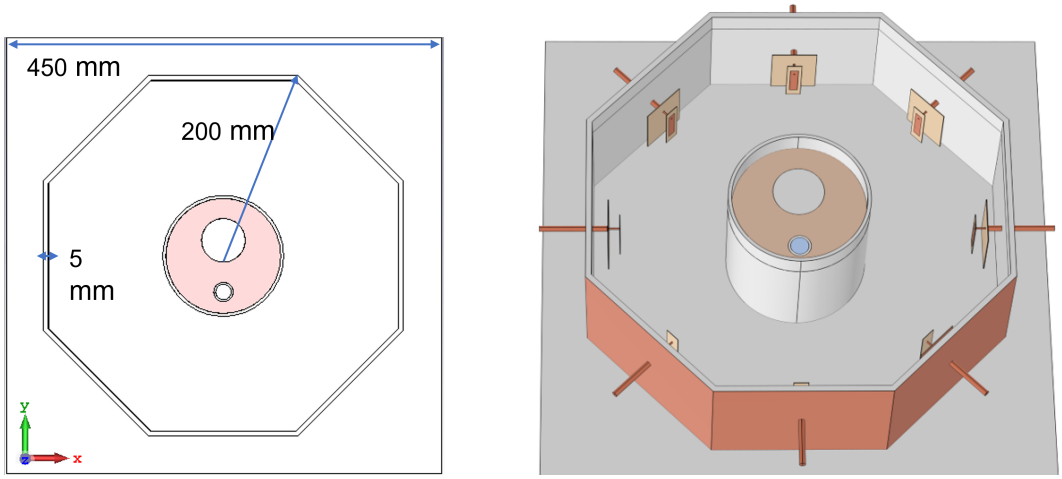

(a) (b)

Figure 3.9: (a) The top view layout of the HT mock-up (b) Digital twin of the implemented mock-up developed in COMSOL Multiphysics environment.

Physics and Boundary Conditions

In COMSOL Multiphysics, defining boundary conditions is essential for accurately modeling interactions between different materials and capturing physical

phenomena at specific surfaces and edges. These conditions help approximate real-world system behavior within a constrained computational domain.

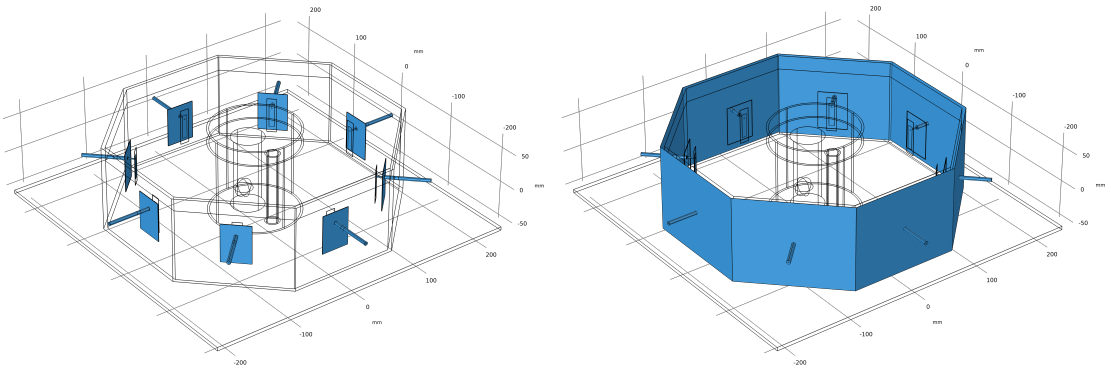

(a) (b)

Figure 3.10: PEC Boundary Condition.

For the electromagnetic simulation, the antennas and the external walls of the octagonal frame are assigned as Perfect Electric Conductors (PEC), representing them as idealized lossless metallic surfaces. As depicted in Figure 3.10, the PEC boundary condition ensures that all incident electromagnetic waves are reflected by enforcing a zero tangential electric field along the designated surfaces. This assumption provides a reasonable approximation for modeling the copper components of the antennas and the thin copper layers lining the outer walls of the prototype.

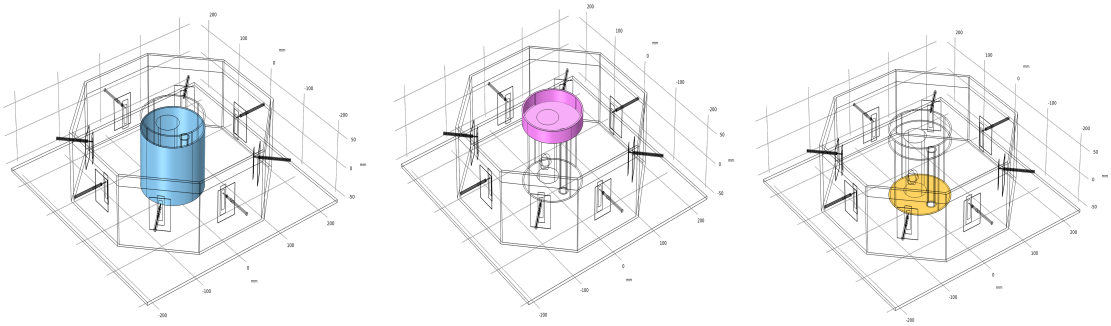

(a) (b) (c)

Figure 3.11: Heat Flux Boundary Conditions

The bioheat transfer simulation needs to be completed by the boundary conditions, which describe the thermal interaction of the system with the surrounding environment [27]. The initial temperature in the neck phantom was fixed according to the average temperature read by the FBG sensors at the beginning of the heating session. To describe the interaction of the neck phantom with the air and the water

of the waterbolus, the convective heat flux boundary condition was used, defined as:

$$\hat{\boldsymbol{n}} \cdot (k\boldsymbol{\nabla} T) = h\,(T_{ext} - T)\,, \tag{3.1}$$

where $\hat{\boldsymbol{n}}$ is the unit vector normal to the boundary, h (W/(m^2°C)) is the heat transfer coefficient, and T_{ext} is the external reference temperature. The boundary condition (3.1) was applied at the following interfaces (See Figure 3.11): phantom lateral walls–waterbolus (h_{wb}), phantom upper boundary–air (h_{tn}), phantom lower boundary–air (h_{bn}). A heat flux boundary condition was applied at the interface between the bottom of the phantom and the air since during the heating session the prototype was lifted from the bench with proper supports to avoid thermal insulation. The internal air was included in the computational domain hence no boundary conditions were applied on the hollow cylinder representing trachea. The temperatures (T_{ext} in (3.1)) of the surrounding air and the waterbolus were set to their corresponding values measured during the heating session. Then, the best values of the heat transfer coefficients have been obtained by varying these parameters in COMSOL in order to minimize the average absolute difference between measured and simulated temperatures, assuming that all measurement points are known at all times.

Mesh Construction

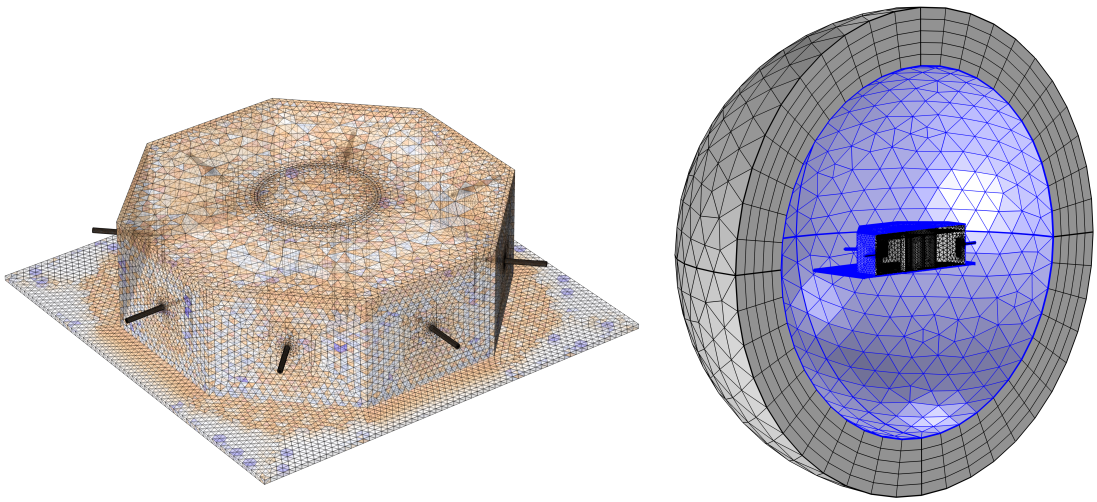

(a) (b)

Figure 3.12: (a) Finite Element mesh of simulated prototype in COMSOL, (b) Spherical Perfectly Matched Layers (PML) considered in EM simulation. Note that only half of the sphere is shown here for visualization purposes.

COMSOL Multiphysics employs the finite element method (FEM) to numerically solve complex physical equations, which are often represented by partial differential equations (PDEs) that lack analytical solutions [62]. The software approximates these equations over discrete points within the computational domain, and the mesh defines the resolution of these approximations.

The accuracy of numerical solutions depends on mesh density—a finer mesh enhances solution precision but also increases computational complexity. Consequently, a balance between accuracy and computational efficiency must be maintained. For this study, as shown in Figure 3.12a, a *tetrahedral* mesh is applied, with localized refinement near geometric edges to enhance accuracy where needed.

Additionally, as shown in Figure 3.12b, a Perfectly Matched Layer (PML) was incorporated to simulate an open-boundary domain, enabling accurate electromagnetic wave propagation and energy absorption without spurious reflections or non-physical artifacts.

Chapter 4

SAR-based Optimization

This chapter reports the main contents and results of the published article [63].

As already mentioned, in microwave hyperthermia, the electromagnetic fields are externally generated and coupled into the patient body via antenna applicators in order to increase the temperature of tumor cells. As a result, the primary goal is to shape the power deposition (specific absorption rate, SAR), with focusing in the tumor region and minimizing the risk of hotspots in the surrounding healthy tissues. For non-superficial tumors, phased array antennas are used to achieve this focusing. Finding patient-specific optimal antenna feeding coefficients represents an essential step to ensure an effective and safe administration of the heating. In this Chapter, we present a way to optimize the array power transfer effectiveness (impedance matching) that does not deteriorate the spatial power deposition performance. A global optimization approach is adopted, using a cost function properly tailored to incorporate the active reflection coefficients of the array and the Hotspot-to-Target SAR Quotient (HTQ) – the latter being the standard in hyperthermia applications. The effectiveness of the technique has been demonstrated in a scenario relevant to the treatment of tumors in the neck region. The results show that our method significantly improves antenna matching without compromising the HTQ, achieving values within the recommended limits. The performance of the proposed approach has also been experimentally tested with full heating in the setup described in Section 3.3.

4.1 Introduction

Building on the established clinical role of HT as an adjuvant to radiotherapy and chemotherapy, and on the treatment planning framework introduced in Chapters 2 and 3, this chapter focuses on the joint optimization of antenna system matching and specific absorption rate (SAR). The physical principle of hyperthermia relies on the absorption of microwave radiation by biological tissues, which

induces molecular motion and localized heating [20, 64]. The localized heating improves the penetration of chemotherapy drugs into the tumor cells, and increases the sensitivity to radiation, making HT a potent sensitizer for chemotherapy and radiotherapy.

For the treatment of sub-superficial and deep-seated tumors, phased-array antenna applicators are commonly employed [15, 65]. These are typically combined with a waterbolus, which prevents skin overheating while improving electromagnetic coupling into the body [66].

As described in Sec. 2.4, hyperthermia treatment planning (HTP) is a key step in clinical practice, recommended by current guidelines [67] to determine the set of optimal steering parameters (amplitude and phase) for each antenna in the applicator array [68]. Patient-specific numerical simulations are employed in state-of-the-art clinical approaches [39], involving electromagnetic simulations of the segmented model of the patient's region of interest (ROI) obtained from CT or MRI scans [38], as well as the geometry of the applicator. Central to all optimization techniques described in the literature is the optimization of the antenna feedings to maximize power deposition within the tumor region while minimizing the occurrence of hotspots on the surrounding healthy tissues.

4.1.1 State-of-the-Art

The actual medium in which the array operates is patient-specific, and hence different in all applications. Hence, the antennas are usually designed to operate in an average situation, which typically corresponds to the coupling medium alone in the entire region of interest (e.g. waterbolus [18] for deep-seated tumors); the antenna geometry and array layout are designed to have low reflection (S_{ii}) at each port and low inter-element coupling (S_{ij}) in that reference situation.

Current optimization techniques employed in clinical settings are either temperature-based [37] or SAR-based [69, 70, 71]. The temperature-based approach aims at directly optimizing temperature distribution within the tumor and in the surrounding tissues, yet the outcome can be affected by the uncertainty characterizing thermal parameters [72, 73]. Conversely, SAR-based optimization techniques exploit SAR as a surrogate metric, which correlates strongly with temperature increase and exhibits lower computational complexity while yielding favorable treatment outcomes [74]. Both SAR- and temperature-based methods are currently in use in the clinical setting while both require real-time adjustments during treatment [69, 75]; with SAR-based optimization being favored for its efficiency, which will be the focus of this study.

4.1.2 Innovation

State-of-the-art array coefficient synthesis approaches optimize SAR (or temperature) distribution, but do not consider the *array impedance mismatching* due to operating in a situation (patient) that differs from the array design environment.

The objective of this paper is to optimize the array antenna matching in the presence of a given patient medium, without affecting the SAR deposition profile performance. To the best of the authors' knowledge this has not been addressed yet in the existing literature.

The presented approach significantly improves antenna matching without compromising the Hotspot-to-Target SAR Quotient (HTQ). The proposed technique is demonstrated in an environment representative of HT in the neck region; the approach is first validated on an "in-silico" (simulative) model of the setup, followed by an experimental validation using a physical phantom.

The proposed method has general applicability to sub-superficial and deep-seated tumors located in all regions of the human body that (intrinsically) require the use of phased array applicators for energy focusing. In our present application, we will focus on deep-seated tumors in the H&N region; the underlying microwave HT system has been demonstrated in other studies for several other anatomical districts [18, 59, 14].

4.2 Joint Optimization Approach

The primary objective of SAR-based optimization is to maximize power deposition within the tumor region while minimizing the risk of overheating in the surrounding healthy tissues; we recall the definition of the specific absorption rate (SAR):

$$\mathrm{SAR}(\boldsymbol{r}) = \frac{\sigma(\boldsymbol{r})}{2\rho(\boldsymbol{r})}|\boldsymbol{E}(\boldsymbol{r})|^2 \tag{4.1}$$

where: σ (S/m) is the electrical conductivity, ρ (kg/m^3) is the tissue mass density, and $\boldsymbol{E}$ (V/m) represents the total electric field (using the peak value convention), all evaluated at position vector $\boldsymbol{r}$. The total electric field can be expressed as a superposition of the electric fields generated by each antenna of the $N-$element array acting as standalone and the unknown excitation coefficients, i.e.:

$$\boldsymbol{E}(\boldsymbol{r}) = \sum_{n=1}^{N} \tilde{\nu}_n \, \boldsymbol{e}_n(\boldsymbol{r}), \tag{4.2}$$

where $\boldsymbol{e}_n(\boldsymbol{r})$ is the field generated by the nth antenna when fed by unitary excitation, while $\tilde{\nu}_n$ is the nth antenna excitation coefficient – considering both amplitude and phase – as part of the array, which can be conveniently expressed as:

$$\tilde{\nu}_n = \nu_0 \xi_n e^{i\varphi_n}, \tag{4.3}$$

where $\varphi_n \in [0,2\pi)$ represents the phase, $\xi_n \in [0,1]$ denotes the normalized amplitude coefficient ,and $\nu_0 = \sqrt{2R_0P_0}/\|\boldsymbol{\xi}\|_2$ is a constant amplitude coefficient, being $R_0 = 50\,\Omega$ the reference impedance of each antenna, P_0 the total power delivered to the array, and $\|\cdot\|_2$ the Euclidean norm. Note that the fields $\boldsymbol{e}_n(\boldsymbol{r})$ in (4.2) are obtained in the actual situation, i.e., considering the actual scenario (patient and applicator), and are the extension of the embedded pattern concept [76].

The standard cost function to be minimized in SAR-based optimization is the Hotspot-to-Target SAR Quotient (HTQ) [69], defined as:

$$\mathrm{HTQ} = \frac{\langle \mathrm{SAR}_{\,\mathrm{V1}} \rangle}{\langle \mathrm{SAR}_{\,\mathrm{TARGET}} \rangle}, \tag{4.4}$$

where $\langle \mathrm{SAR}_{\,\mathrm{V1}} \rangle$ is the average SAR in V1, being V1 the 1% of the healthy volume with the highest SAR [66, 77], and $\langle \mathrm{SAR}_{\,\mathrm{TARGET}} \rangle$ is the average SAR in the target region. While the goal of the standard SAR-based optimization is to minimize the HTQ, reaching a value of $\mathrm{HTQ} \leq 1$ is considered acceptable in clinical settings [78].

Antenna array matching is described by the *active reflection coefficients* Γ_n^a at the antenna ports [76, 79]:

$$\Gamma_n^a = S_{nn} + \sum_{m \neq n} S_{nm} \frac{\tilde{\nu}_m}{\tilde{\nu}_n}, \tag{4.5}$$

where S is the scattering matrix, and $\tilde{\nu}_1, ..., \tilde{\nu}_N$ are the considered excitation coefficients. Throughout this paper, the magnitude of the reflection coefficient will be expressed in dB as common in the related literature, i.e. $20 \log |\Gamma|$ is intended when reporting the value in dB.

In this article we propose an optimization method that includes active reflection coefficients bounding into the cost function. It is apparent that array matching imposes additional constraints to the optimization; hence, SAR performance is expected to be affected, with respect to the case in which no such constraints are enforced. Hence, it is recognized that absolute minimization of active reflection coefficients is not the best strategy: it is instead more expedient to require that the active reflection coefficients are lower than a given threshold (typically acceptable threshold is $\Gamma_{th} = -10$ dB). To achieve this joint optimization, we define the cost function $\mathcal{F}$ as:

$$\mathcal{F} = \alpha\,\mathrm{HTQ} + (1-\alpha)\sum_{n=1}^{N} f_n, \;\; f_n = \begin{cases} 0 & \text{if } |\Gamma_n^a| \leq \Gamma_{th} \\ 1/N & \text{if } |\Gamma_n^a| > \Gamma_{th} \end{cases} \tag{4.6}$$

here, α is a weighting factor and Γ_{th} is a threshold value.

For the optimization, we employed a particle swarm optimization (PSO) algorithm [80, 81]. We found that $\alpha = 0.5$ was the best choice, consistent with the fact that after a few iterations the HTQ is on the order of 1.

4.3 Application and Validation

The optimization method introduced in Sec. 4.2 was validated using the experimental testbed and its digital twin in COMSOL Multiphysics, previously described in Chapter 3. For completeness, only a brief recall of the setup is provided here, while full details on phantom preparation, material characterization, and prototype design can be found in Sections 3.2–3.3.

The testbed considered for the verification of the proposed procedure is a mock-up reproducing a typical HT applicator used for treating deep-seated and subsuperficial tumors in the head and neck (H&N) region [18, 59]. The in-silico model of this mock-up, illustrated in Fig. 3.3b, was implemented in COMSOL Multiphysics [48]. The dielectric and thermal properties of the materials used in this mock-up are detailed in Table 3.4.

The HT applicator (see Fig. 3.4b) consists of a circular array of 8 patch antennas immersed in water, and arranged in an octagonal PMMA container.A PMMA hollow cylinder simulates the neck of the patient using a phantom that mimics the dielectric properties of human muscle [26]; it contains one solid and one hollow PMMA cylinder, that simulate the spine and the trachea, respectively. The space between the container walls and the central phantom is filled with demineralized water, which serves as the substrate for the patch antennas and forms the so-called waterbolus [18]. The phantom used in this study is a semi-solid agar-based phantom, properly developed to reproduce the dielectric properties of muscle tissue (see Section 3.2 and Table 3.4) [52, 49].

The patch antennas forming the array were designed to be matched at the operating frequency $f = 434$ MHz [17] (See Fig. 3.5); this frequency lies within a commonly used ISM band, and it has been demonstrated to provide a good balance between tissue penetration and energy absorption, and size of the applicators, thus making it well-suited for deep-seated tumors HT [82, 83]. The optimized dimensions of the antenna is detailed in section 3.3.1.

To quantify the ability of the designed setup to couple the electromagnetic energy into the phantom, the effective field size (EFS), defined as the area enclosed by the 50% SAR curve at 1 cm depth within the tissue [84], and the penetration depth, defined as the depth at which the SAR becomes $1/e^2$ of its surface value [85], are simulated for the antenna 7 (see Fig. 3.4b) and reported in Fig. 4.1. Specifically, Fig. 4.1a reports the simulated normalized SAR isolines at 1 cm depth within the tissue, when only the antenna 7 is fed (see the SAR map in Fig. 4.1b), while Fig. 4.1c shows the normalized SAR evaluated in the same configuration as a function of the depth inside the phantom along the central x-axis (0mm-depth means the surface of the phantom). The estimated values for the EFS and the penetration depth are 21.49 cm^2 and 37.32 mm, respectively.

The considered target region is a sphere with radius $r_t = 15$ mm located centrally within the neck phantom at spatial coordinates $(x_t, y_t, z_t) = (-30, -15, 0)$

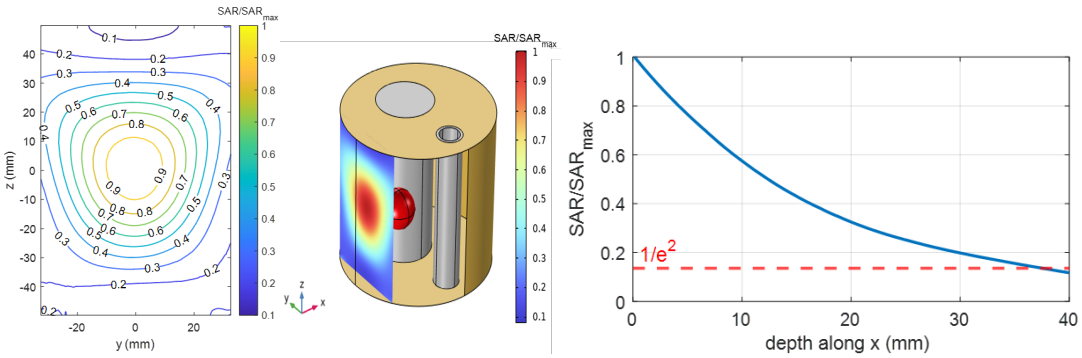

(a) (b) (c)

Figure 4.1: (a) Simulated normalized SAR contours at a depth of 1 cm within the phantom along the x axis. The 0.5 isoline encloses the region used to estimate the effective field size (EFS). (b) Normalized SAR map visualized on a plane at 1 cm depth within the phantom. (c) Normalized SAR values versus the depth inside the phantom, evaluated along the x-axis for constant $y = z = 0$ mm. All results refer to the case when only antenna 7 is fed (see Fig. 3.4b for details on the numbering used).

mm, being (0,0,0) the coordinates of the center of the neck cylinder. In the performed optimizations, we decided to consider all phases as relative to the antenna 1 (see Figure 3.4b for details on the numbering used), which means $\varphi_1 = 0°$; relative amplitude coefficients (ξ_n) were constrained to vary within 0.5 and 1; and the active reflection coefficient threshold (Γ_{th}) in (4.6) was set to -10 dB.

The resulting optimized antenna coefficients extracted for both cost functions used in this study, i.e., HTQ and $\mathcal{F}$, are reported in Table 4.1. Additionally, Table 4.1 presents the magnitude of the simulated active reflection coefficients $\left(\left|\Gamma^a_{n,sim}\right|\right)$ corresponding to each set of feeding coefficients.

The magnitude of the simulated active reflection coefficients listed in Table 4.1 highlights the mismatch issues associated with using the standard cost function (HTQ). Notably, except for the 6th antenna, all array elements exhibit active reflection coefficients higher than the specified threshold of $\Gamma_{th} = -10$ dB. In contrast, the magnitude of the simulated active reflection coefficients obtained using the proposed cost function ($\mathcal{F}$), as listed in the last column of Table 4.1, all fall below the -10 dB threshold since this criterion was directly incorporated into the proposed cost function ($\mathcal{F}$).

The optimization properties presented in Table 4.2 indicate that the final HTQ values for both optimization methods meet the typical threshold considered acceptable for clinical treatment—they are both less than 1. Moreover, there is no significant difference in computational demand between the two optimization methods.

Table 4.1: Antenna feeding coefficients (ξ_n, φ_n) and corresponding magnitude of the simulated active reflection coefficients $\left(\left|\Gamma^a_{n,sim}\right|\right)$

	Standard optimization approach			Proposed optimization approach		
$\boldsymbol{n}$	$\boldsymbol{\xi_n}$(-)	$\boldsymbol{\varphi_n}$ (°)	$\left\|\Gamma^a_{n,sim}\right\|$ (dB)	$\boldsymbol{\xi_n}$ (-)	$\boldsymbol{\varphi_n}$ (°)	$\left\|\Gamma^a_{n,sim}\right\|$ (dB)
1	0.69	0	-9.85	0.73	0	-12.76
2	0.50	73.41	-5.13	0.59	87.46	-13.38
3	0.50	76.24	-4.69	0.64	147.32	-10.00
4	0.50	0.00	-7.62	0.66	151.63	-10.00
5	0.50	47.04	-4.47	0.50	111.66	-10.00
6	0.79	1.89	-12.57	0.72	11.86	-15.73
7	1.00	-44.49	-9.69	0.99	-24.50	-12.32
8	1.00	-50.22	-9.53	1.00	-27.97	-12.00

Table 4.2: Comparison of the considered optimization approaches and their properties

	Standard (HTQ)	Proposed ($\mathcal{F}$)
Population size	100	100
Num. iterations	214	368
Total time (s)	139	203
HTQ (final)	0.906	0.959

Figure 4.2a illustrates the convergence behavior of the PSO algorithm while minimizing the standard cost function (HTQ) across multiple iterations. The subsequent plots in Fig. 4.2 depict the final normalized SAR distribution obtained in COMSOL Multiphysics using the optimized antenna coefficients presented in Table 4.1. These plots are displayed on three canonical planes passing through the target sphere at its centroid.

Similarly, Fig. 4.3a depicts the optimization process for minimizing the proposed cost function ($\mathcal{F}$) and standard HTQ over PSO algorithm iterations. Using the optimized antenna coefficients obtained with the proposed approach (see Table 4.1), subsequent plots of Fig. 4.3 illustrate the final normalized SAR distribution generated in COMSOL Multiphysics, displayed on the three canonical planes intersecting the target sphere at its centroid.

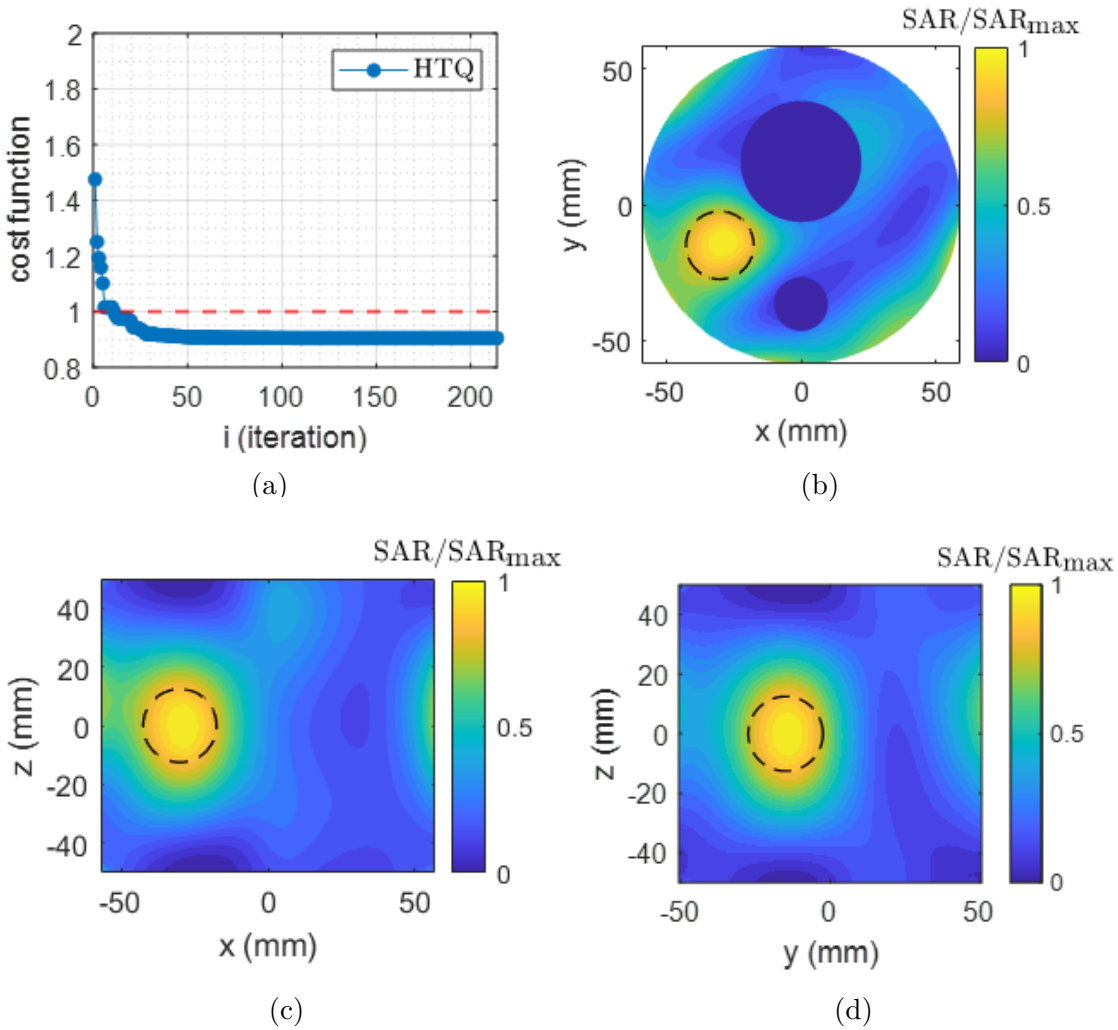

Figure 4.2: (a) Standard cost function (HTQ) evolution. Normalized SAR distribution obtained in COMSOL Multiphysics using the feeding coefficients corresponding to the minimization of the standard cost function (HTQ), displayed on the (b) xy plane , (c) xz plane , and (d) yz plane. The dash circle indicates the profile of the considered target spherical region.

It is worth noting that introducing the active reflection coefficient penalty term in the cost function (see eq. (4.6)) does not necessarily translate into a higher SAR concentration in the target region. This behavior is expected, as the penalty promotes stable power coupling and reduces backward power toward the RF amplifiers; however, part of the additional transmitted power can be dissipated in the lossy waterbolus rather than contributing to the target heating. Nevertheless, the resulting SAR distribution still satisfies the clinically accepted quality criteria: as shown in Fig. 4.3 and in the last row of Table 4.2, the computed HTQ remains below 1, ensuring that therapeutic energy is still appropriately concentrated within

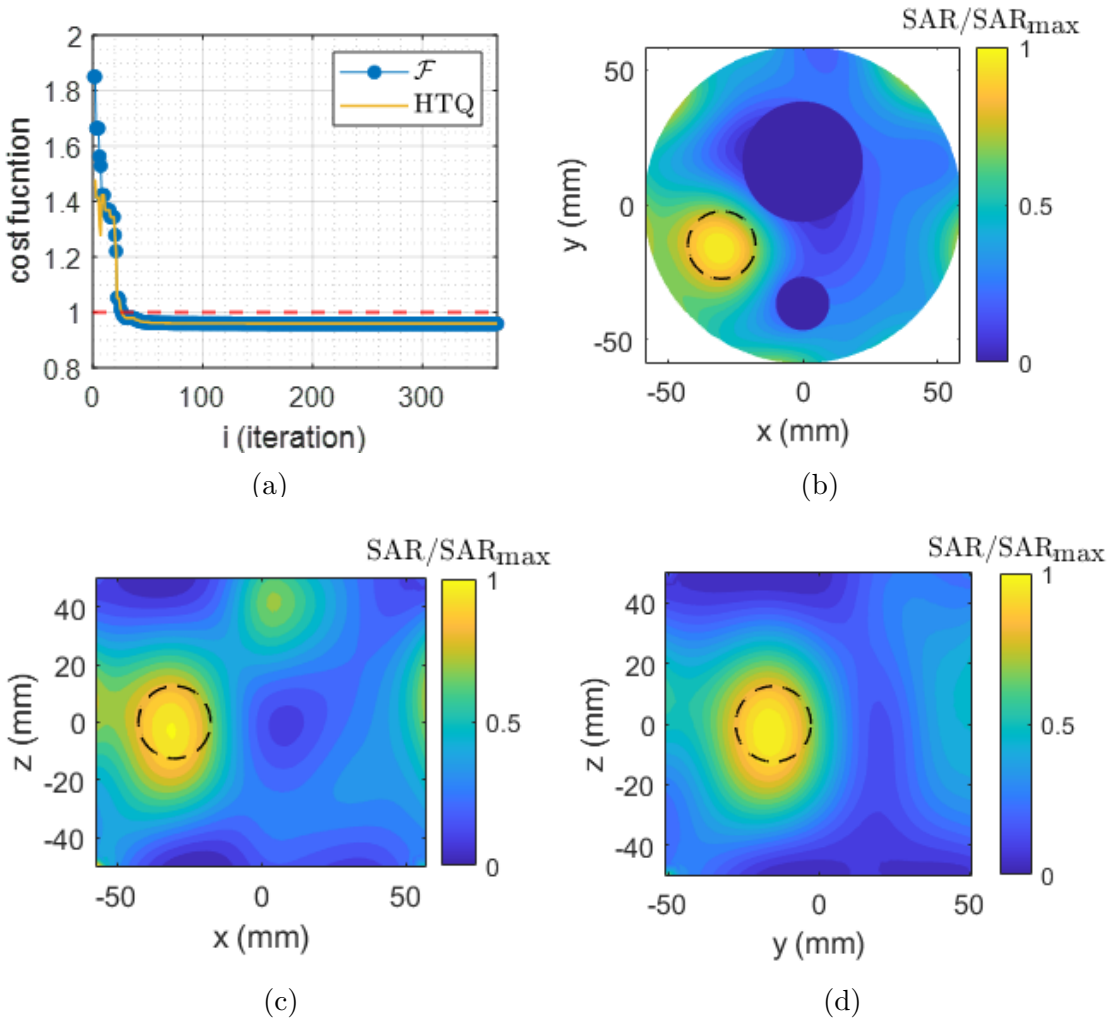

Figure 4.3: (a) Proposed cost function ($\mathcal{F}$) evolution alongside the corresponding HTQ. Normalized SAR distribution obtained in COMSOL Multiphysics using the feeding coefficients corresponding to the minimization of the proposed cost function ($\mathcal{F}$), displayed on the (b) xy plane , (c) xz plane , and (d) yz plane . The dash circle indicates the profile of the considered target spherical region.

the target. Future work will investigate tuning α and Γ_{th} in the expression of the cost function (eq. (4.6)) and/or adding a term penalizing power dissipation in the waterbolus to further improve energy transfer to the neck/target region.

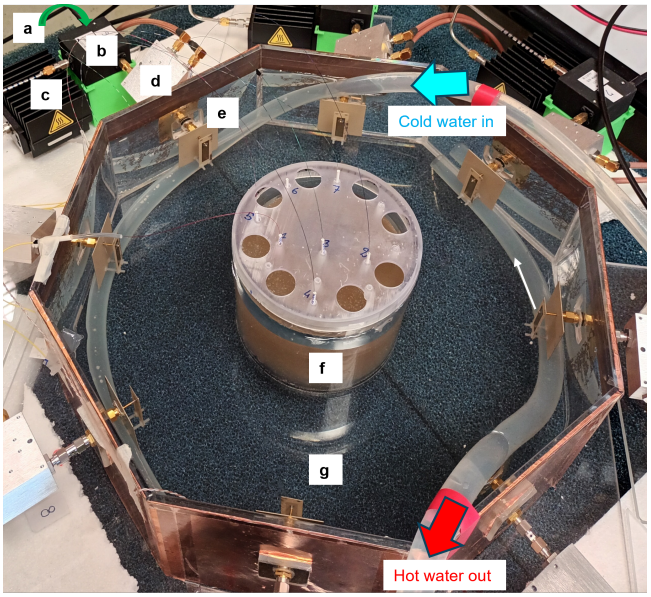

Figure 4.4: Setup of the experimental mock-up reproducing the HT applicator. Components are labeled as follows: a) RF signal coming from Power Amplifier (PA) – Variable Gain Amplifier (VGA) – Phase Shifter (PS) chain, b) Circulator, c) Dummy Load, d) Directional Coupler, e) Patch Antenna, f) Neck Phantom, g) Waterbolus with circulating water.

To apply the optimized feeding coefficients to the physical prototype, the experimental mock-up introduced in Sec. 3.3.1 was used. This mock-up, which reproduces a typical HT applicator, integrates the phantom, antenna array, waterbolus, and the complete electronic chain for signal distribution and control. A schematic of the setup with the labeled components is shown in Fig. 4.4. For details on the design and operation of the feeding network, including phase and amplitude control and cooling system, the reader is referred to Section 3.3.1.

During the experimental session, a real target sphere with radius $r_t = 15$ mm was introduced in the neck container before pouring the agar mixture reproducing the neck phantom (see details on section 3.2.1 and Figs. 3.2b,c), trying to place it in the same position as the target sphere considered in the COMSOL model when the SAR-based optimization was performed.

To monitor temperature variations across the implemented mock-up in real time and without interfering with the electromagnetic field, a system of Fiber Optic Sensors (FOSs) based on an array of Fiber Bragg Gratings (FBGs) has been implemented as detailed in Section 3.3.1. The use of optical fibers makes the sensors intrinsically free from artifacts induced by the interaction with microwaves, such as self-heating effects. Moreover, their small size does not appreciably alter the temperature distribution. Among all the various types of fiber optic temperature

Table 4.3: Antenna phases optimized using the proposed cost function ($\mathcal{F}$) and comparison of the simulated and measured magnitude of the active reflection coefficients

n	1	2	3	4	5	6	7	8
φ_n (°)	0	79.83	156.72	-156.06	-142.04	0	-43.86	-43.11
$\left\|\Gamma^a_{n,sim}\right\|$ (dB)	-18.42	-10.60	-11.90	-12.44	-10.81	-16.53	-16.23	-20.02
$\left\|\Gamma^a_{n,exp}\right\|$ (dB)	-15.99	-7.58	-10.11	-15.59	-18.24	-11.34	-23.89	-25.57

sensors, FBG-based devices stand out for the unique combination of properties, such as a well consolidated and reproducible fabrication, fast response, and robustness to noise [40]. Moreover, they are the only type that can be easily multiplexed along the same fiber to form several sensing points, obtaining a dense array of temperature sensors having good accuracy and reasonable cost. FBGs have already been proved to be well-suited for real-time temperature monitoring during medical thermal treatments [43]. However, FBGs – like other FOSs – are also sensitive to mechanical deformations. Therefore, to mitigate this cross-sensitivity, the fiber containing the FBGs has been enclosed in a small glass capillary sealed with epoxy. The final embodiment of the multipoint sensor is a small glass cylinder about 10 cm long, with an external diameter of 2 mm, embedding 13 sensing points with variable spacing from 5 mm to 10 mm to provide the best spatial resolution where the maximum thermal gradient is expected. The small dimensions of each multipoint sensor (volume of about 0.3 cm^3) has negligible perturbation effects both on the electromagnetic field and on the temperature distributions [43]. Each multipoint sensor has been calibrated against a traceable thermometer in the temperature range from 15°C to 45°C. After the calibration, the deviation from the fitting model was found to be below 0.1°C [86].

The SAR-based optimization process for the implemented mock-up was conducted using the proposed method (see Section 4.2). To maximize the delivered power with the available PAs (max 10 W each), staying within the safe operating areas of the electronic devices composing the chain, only the phase coefficients of the array (φ_n) were taken into account during the optimization process. A feedback control system was used to lock the optimized phases and the constant amplitudes provided to the antennas to the desired values for the entire heating session (130 minutes), with a maximum error lower than 0.3° for the phase and lower than 0.04 dBm for the amplitude. As a results, each antenna in the array delivered approximately 7.5 W for a total output power of 60 W for the entire array applicator.

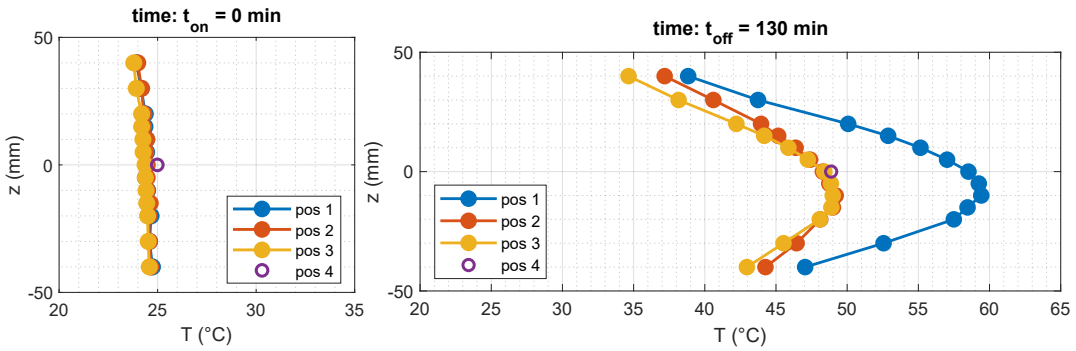

(a) (b)

Figure 4.5: Temperatures recorded by the FOS arrays at (a) the beginning , and at (b) the end of the heating session.

However, for the sake of simplifying the electronic chain, only phase coefficients of the array were taken into account during the optimization process.

The optimized phases along with the simulated and experimentally measured magnitude of the active reflection coefficients are reported in Table 4.3. A noteworthy level of agreement is observed between the simulated and experimental values, affirming the reliability of the model implemented in COMSOL in accurately reproducing the behavior of the realized prototype. Using the proposed approach, we achieved almost all active reflection coefficients below the -10 dB threshold, as shown in Table 4.3. The simulated SAR profile corresponding to the optimized antenna phases (Table 4.3) for a total input power $P_0 = 60$ W provides an average SAR of 33 W/kg in the tumor target region and of 10 W/kg in the surrounding healthy tissues.

The temperature measurements recorded at the start and at the end of the 130-minutes heating session are illustrated in Figure 4.5a and Figure 4.5b, respectively. We observe that the duration of the heating session is longer than commonly encountered in the clinic as it was necessary to achieve meaningful temperature elevation within the tumor target region with the powers available in our laboratory setup. The maximum available power output was limited to 10 W per antenna, which is significantly lower than the power levels used in clinical hyperthermia setups that typically operate at higher outputs and last 60–75 minutes [87]. Additionally, our experimental conditions required starting at room temperature, unlike clinical treatments that begin at basal body temperature. It is important to emphasize that these experimental constraints do not compromise the validity of the proposed method or its ability to achieve precise energy deposition. This is demonstrated by the measurements depicted in Figure 4.5b, which confirm accurate radiation focusing on the tumor target region, as indicated by the observed temperature changes of the array 1 (array passing tumor, see 3.8a). A detailed overview of the temperature increases in the array 1 is provided in Figure 4.6,

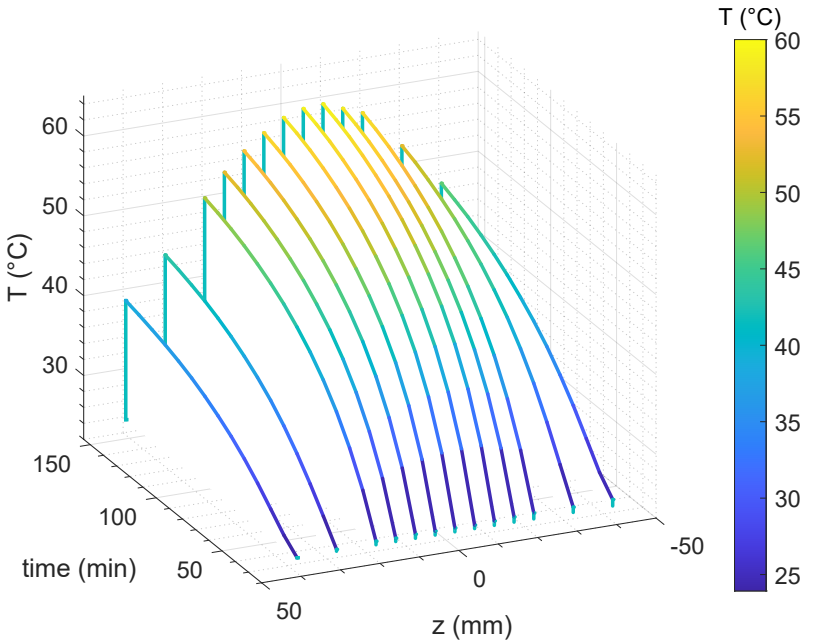

Figure 4.6: Temperature values read by the array of FBG sensors passing through the tumor target (array 1) as function of time and of the z-coordinate.

where the measured temperature profiles are reported over time and along the z-coordinate.

To simulate the heating session, a heat transfer study was introduced in the in-silico counterpart of the realized mock-up implemented in COMSOL Multiphysics and described in Section 3.3.2. The used heat transfer model follows the Pennes' Bioheat Equation (Eq. 2.11) and thermal boundary conditions (Eq. 3.1) were applied to account for the interactions of the neck phantom with the surrounding environment [27]. The convective heat flux boundary condition was used at the following interfaces: phantom upper boundary–air, phantom lower boundary–air, phantom lateral walls–waterbolus. Initial temperatures and external reference temperatures were set according to the measurements performed during the heating session.

As evidence of the agreement between the mock-up and its in-silico counterpart, the measured and simulated temperatures are shown as a function of time at the tumor center ($z = z_t = 0$ mm) in Figure 4.7. This figure also effectively demonstrates the success of our method in achieving a favorable temperature increment in the tumor region during the heating session.

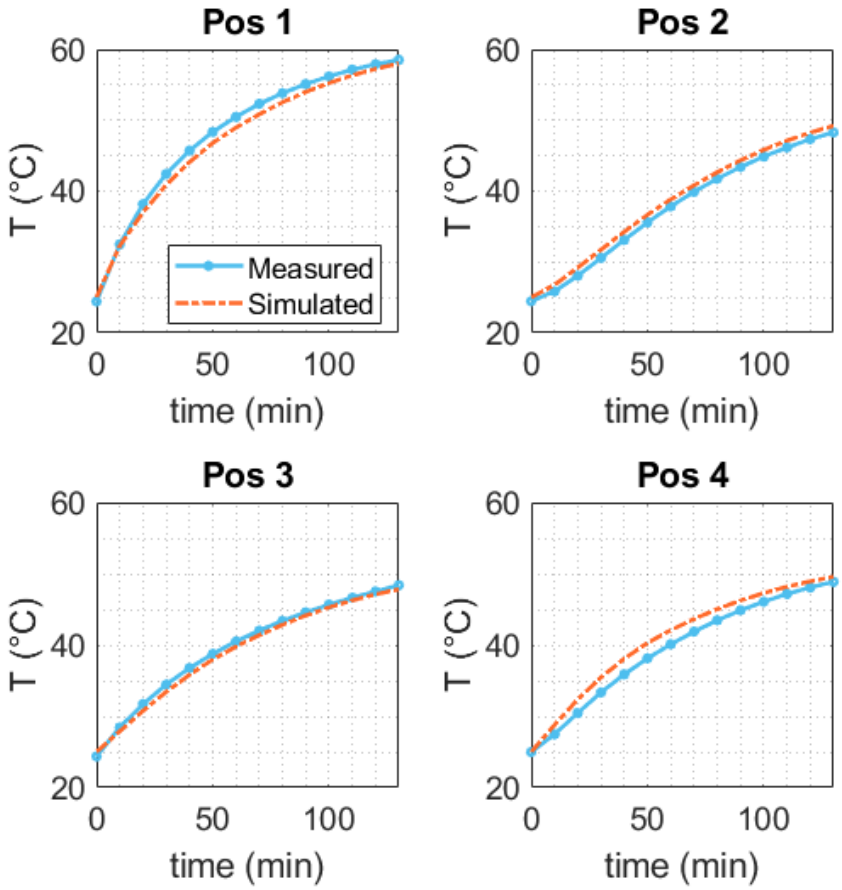

Figure 4.7: Measured temperatures and simulated values as function of time at the z coordinate corresponding to the tumor center ($z = z_t = 0$ mm).

4.4 Conclusions

In this study, we introduced and demonstrated a novel approach to optimization for patient-specific hyperthermia planning, in which array impedance matching is guaranteed. Our proposed optimization approach has demonstrated improvements in antenna performance during HT treatments, without altering the required spatial power deposition recommended performance. The method ensures that almost all active reflection coefficients remain below the -10 dB threshold, which is important for optimizing power coupling and maintaining electronic stability. By incorporating active reflection coefficient constraints, we achieved satisfactory SAR focusing on the tumor target while ensuring that the electronic system remains fully operational thanks to controlled mismacthing. The results show that our method significantly improves antenna matching without compromising the HTQ, achieving values within the recommended limits. Furthermore, the proposed approach is not

confined to SAR-based optimizations; it can also be adapted for temperature-based methods.

Chapter 5

Heat Focusing and Blood Flow Considerations

This chapter reports the results submitted at EuCAP 2025 [88]. It investigates how blood flow in major vessels affects temperature distribution during hyperthermia treatments in the head and neck (H&N) region. To do this, we used an in-silico model and a physical phantom of the neck region where a silicon tube with flowing water was introduced to simulate the presence of the two jugular veins and two carotid arteries. The results show that temperature variations of more than 5°C can affect temperature simulations when the effect of blood flow is not considered. The achieved results were confirmed by temperature measurements performed using the physical phantom and a full-operating mock-up reproducing an hyperthermia treatment in the neck region.

5.1 Introduction

Tissue mimicking materials (TMMs) are essential in medical research, providing a platform to test new devices and techniques without risks to humans or animals [50]. These materials, typically incorporated into phantoms, replicate human tissue properties and are invaluable in clinical simulations for imaging, therapy, and device performance validation. Microwave hyperthermia (HT) is among the medical applications requiring phantoms for design and testing.

However, one of the primary challenges in optimizing HT is accurately modeling heat transfer in biological tissues, where the effect of blood plays a critical role in temperature regulation. Despite significant advances in TMMs, the absence of physical phantoms for hyperthermia reproducing the effects of the blood system has limited experimental validation [50].

This gap limits the ability to experimentally validate and optimize microwave

hyperthermia treatments, leaving researchers to rely heavily on computational models to simulate blood flow and its thermal effects.

The present study introduces a head and neck (H&N) phantom that incorporates major vessels, i.e., the jugular veins and the carotid arteries. This allows for the assessment of vascular dynamics' impact on temperature focusing during microwave hyperthermia. While blood vessels have almost no effects on SAR focusing, their presence causes changes in the temperature maps due to the cooling effect of the flowing blood. Vessels introduce in fact thermal boundary conditions which can determine deviations of the temperature distribution compared to the corresponding specific absorption rate (SAR) map [89].

5.2 Methodology

The experimental testbed and its digital twin employed in this study are based on the setup described in Chapter 3. In this chapter, additional modifications were introduced to account for the thermal influence of blood flow and to analyze its impact on temperature distribution.

To replicate the influence of blood flow in the experimental setup, four silicone tubes were embedded in the neck phantom to represent the major vessels, i.e., the right and left jugular veins and the right and left carotid arteries, as shown in Fig. 5.1. The zoomed-in view in Fig. 5.1b, taken prior to pouring the agar-based

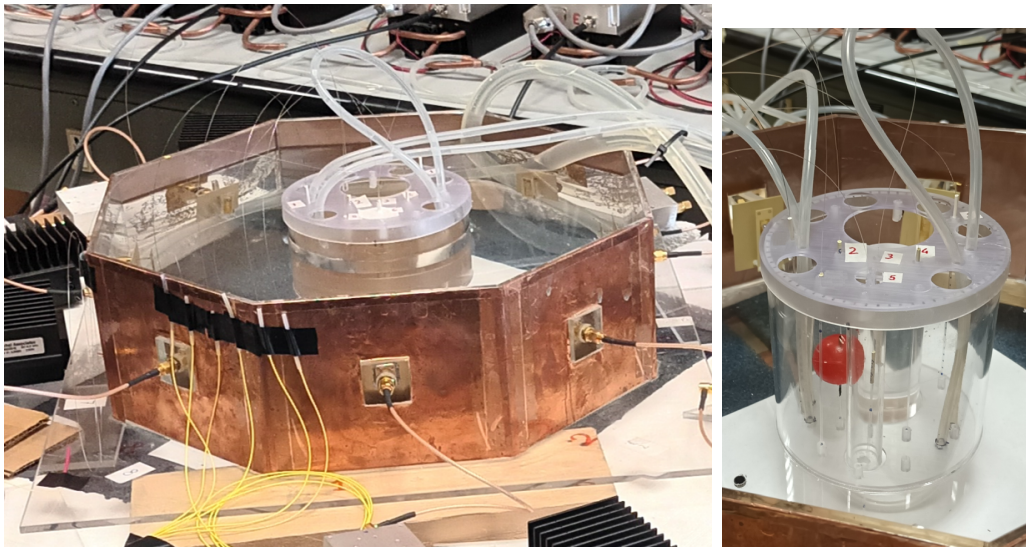

Figure 5.1: (a) Experimental setup of the HT mock-up. (b) Zoomed view of the central section showing the neck phantom prior to pouring the agar mixture, with embedded silicone tubes simulating the major blood vessels and the red sphere representing the tumor target.

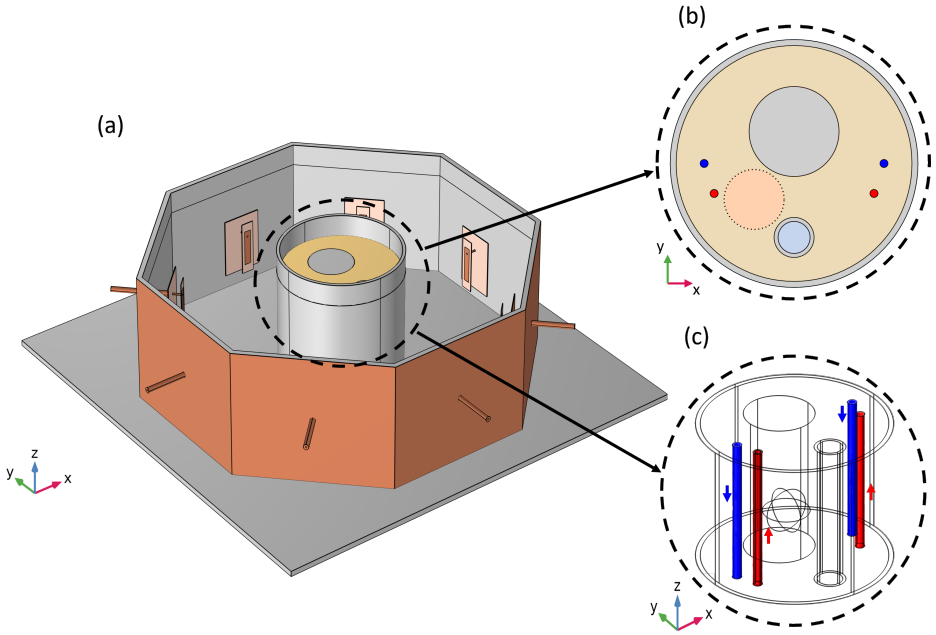

Figure 5.2: (a) Digital twin of the experimental setup implemented in COMSOL Multiphysics. (b) Cross-sectional view in the xy plane showing the four silicone tubes simulating blood vessels (blue: jugular veins; red: carotid arteries). (c) 3D visualization of the neck phantom highlighting vessel arrangement and blood flow directions.

mixture mimicking muscle tissue, highlights the presence of these tubes together with the red tumor target (refer to Section 3.2 for details of the phantom preparation and characterization).

The same modifications were introduced into the digital twin of the mock-up, as highlighted in Fig. 5.2b, which displays the xy cross-sectional plane with the four silicone tubes simulating the jugular veins (in blue) and carotid arteries (in red). The 3D visualization of the vessel arrangement and blood flow directions is shown in Fig. 5.2c. The center coordinates and diameters of the vessel-mimicking tubes and the tumor target are summarized in Table 5.1.

Table 5.1: Center coordinates and diameters of key elements within the neck phantom

Element	x (mm)	y (mm)	d (mm)
Right Jugular vein	-45	0	4
Left Jugular vein	+45	0	4
Right carotid artery	-40	-15	4
Left carotid artery	+40	-15	4
Tumor target	-20	-18	30

The thermal influence of the water circulating inside the vessel-mimicking tubes in the corresponding digital twin was reproduced using a convective heat flux boundary condition (as defined in (3.1)) applied on the outer surface of each tube. During the heating sessions, the circulating water was maintained at an approximately constant temperature of 25.6 °C, which was therefore used as the external temperature in the convective boundary condition. The convective exchange associated with the flowing water was captured through the heat transfer coefficient. This value was optimized in COMSOL by minimizing the discrepancy between all measured and simulated temperatures over the entire heating session, leading to a final value of $h = 10$ W/(m^2 °C). In this way, the induced cooling effect of water flow is incorporated into the model while preserving computational efficiency and accurately reproducing the experimentally observed temperature behaviour.

5.3 Results and Discussion

To evaluate the effect of blood vessels on temperature distribution during microwave hyperthermia, two heating sessions were conducted using the optimized antenna feedings obtained from the SAR-based optimization (see Section 4.3, Table 4.3). The first session was performed using the phantom without any vessels considered, while the second included the embedded silicone tubes simulating the jugular veins and carotid arteries.

5.3.1 Heating Session Without Vessels

The first heating session was carried out using the phantom without any vessel-mimicking elements. The heating session results are already presented in this thesis in Section 4.3, with the configuration described in Section 3.3. However, the experiment was repeated here to enable a direct and consistent comparison with the vascular case reported in the following section.

In this experiment, three arrays of Fiber Bragg Grating (FBG) sensors were used to monitor the temperature evolution along the vertical (z) direction. Figure 5.3 shows the location of the FBG arrays on the xy plane and the temperature values recorded at the beginning (top row) and at the end (bottom row) of the

Table 5.2: Coordinates of FBG sensors used during the heating session without vessels.

Array	x (mm)	y (mm)	z (mm)
1	-30	-15	(30, 20, 15, 10, 5, 0, -5, -10, -20)
2	0	-15	(40, 30, 20, 15, 10, 5, 0, -5, -10, -15, -20, -30, -40)
3	30	-15	(30, 20, 10, 0, -10)

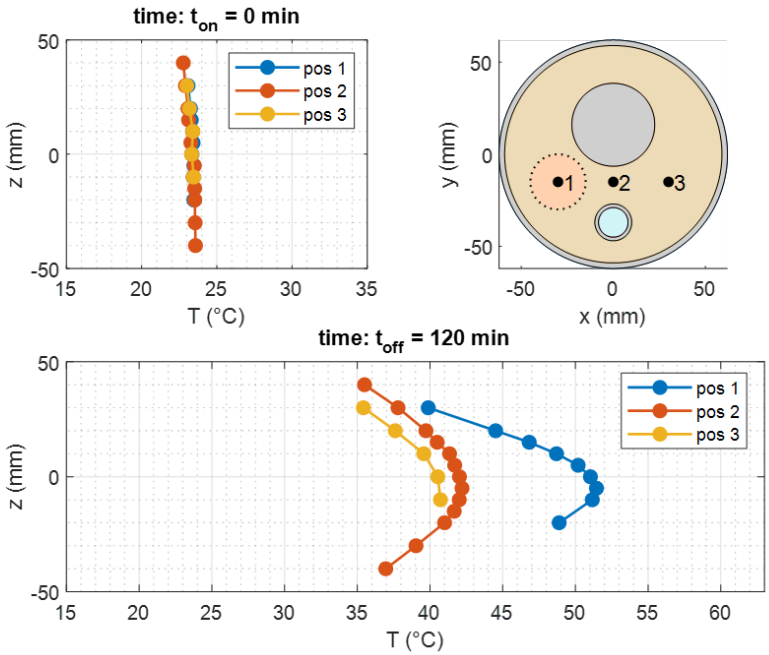

Figure 5.3: Heating session results for the phantom without vessels: Temperature read by the arrays of FBG sensors at the beginning (upper row) and at the end (lower row) of the heating session; the position of the different arrays on the xy plane is indicated in the upper row (right picture) and reported in Table 5.2, together with the z-coordinates of the corresponding FBG sensors.

heating session. The coordinates of all FBG sensors used in this configuration are summarized in Table 5.2. The maximum temperature recorded at the tumor center at the end of heating was approximately 51.4°C, indicating effective power focusing within the target region.

The comparison between experimental measurements and numerical simulations (Fig. 5.4) confirms a strong correspondence between the two. The top panels report temperature evolution over time at the tumor center ($z = z_t = 0$ mm), while the bottom panels show the temperature distribution along the z-axis after 120 minutes of heating.

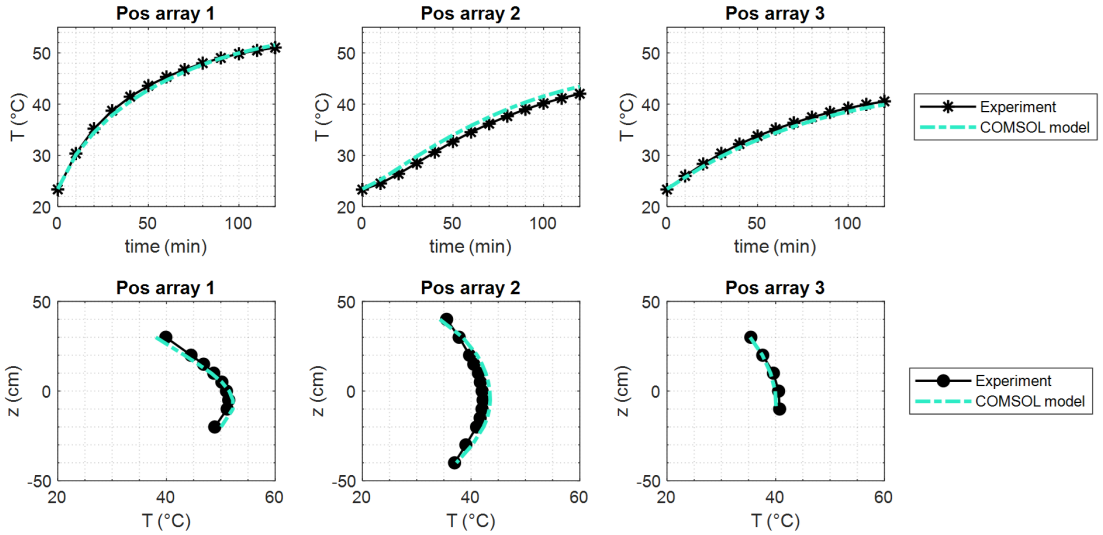

Figure 5.4: Heating session without vessels: comparison between experimental and simulated temperature results. Top: temperature evolution over time at the tumor center ($z = z_t = 0$ mm). Bottom: temperature distribution along the z-axis at the end of the heating session ($t = 120$ min).

5.3.2 Heating Session With Vessels

In the second heating session, four silicone tubes were embedded within the phantom to replicate the major blood vessels (jugular veins and carotid arteries), enabling the thermal assessment due to blood flow. The FBG array layout was slightly adjusted to avoid interference with the silicone tubes while maintaining similar measurement locations w.r.t heating session without vessels.

Figure 5.5 shows the temperature distribution measured at the beginning (top row) and end (bottom row) of the heating session, while Table 5.3 lists the exact coordinates of the FBG sensors used in this configuration. The comparison between experimental measurements and simulation results is reported in Fig. 5.6.

The introduction of the vessel-mimicking tubes caused a clear decrease in temperature within the tumor region, with the maximum value dropping to approximately 42.4°C—over 5°C lower than the case without vessels. This substantial cooling effect is primarily due to convective heat transfer from the circulating fluid

Table 5.3: Coordinates of FBG sensors used during the heating session with vessel-mimicking tubes.

Array	x (mm)	y (mm)	z (mm)
1	-20	-18	(40, 30, 20, 15, 10, 5, 0, -5, -10, -15, -20, -30, -40)
2	0	-18	(40, 30, 20, 15, 10, 5, 0, -5, -10, -15, -20, -30, -40)
3	20	-18	(40, 30, 20, 15, 10, 5, 0, -5, -10, -15, -20, -30, -40)

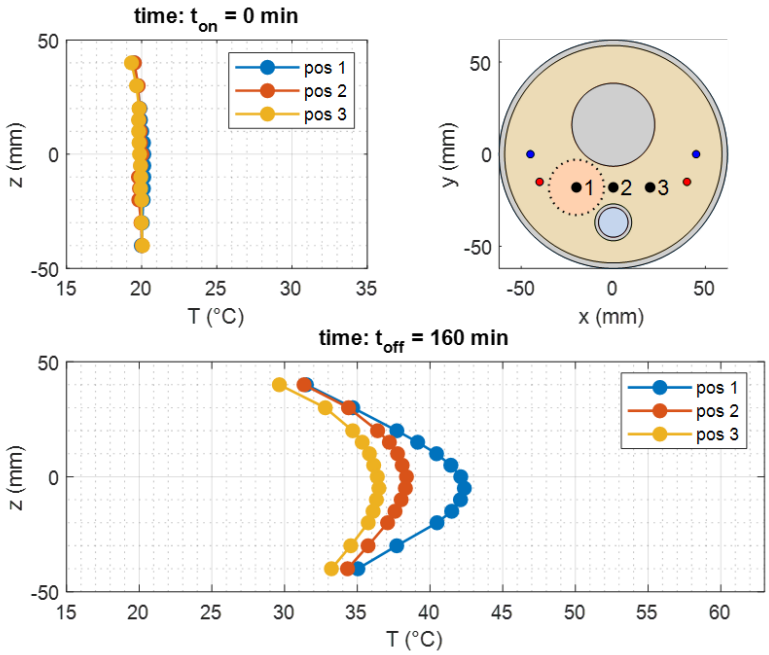

Figure 5.5: Heating session results for the phantom incorporating vessels: Temperature read by the arrays of FBG sensors at the beginning (upper row) and at the end (lower row) of the heating session; the position of the different arrays on the xy plane is indicated in the upper row (right picture) and reported in Table 5.3, together with the z-coordinates of the corresponding FBG sensors.

inside the tubes, most notably in regions near the carotid arteries, where thermal gradients were strongest.

A direct comparison between the two sessions (Figs. 5.4 and 5.6) clearly demonstrates the impact of vascular cooling on the resulting temperature distribution. Despite identical feeding conditions and total applied power, the inclusion of vessel-mimicking tubes led to a significant reduction in steady-state temperature within the target region, particularly along the paths adjacent to the carotid arteries.

These results confirm that neglecting major vessels in hyperthermia simulations can lead to an overestimation of achievable therapeutic temperatures in deep-seated tissues. The presented experimental validation thus provides an important framework for understanding and quantifying vascular cooling effects, improving the accuracy of treatment planning models, and guiding the design of next-generation perfused phantoms for hyperthermia research.

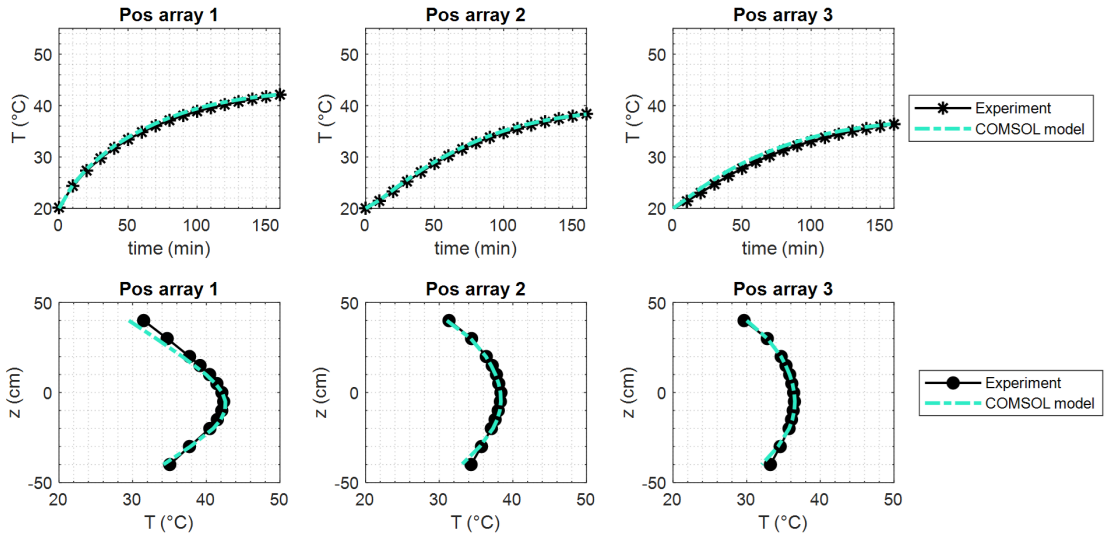

Figure 5.6: Heating session with vessels: comparison between experimental and simulated temperature results. Top: temperature evolution over time at the tumor center ($z = z_t = 0$ mm). Bottom: temperature distribution along the z-axis at the end of the heating session ($t = 160$ min).

5.4 Conclusion

This study underscores the importance of incorporating a vascular model within the phantom for microwave hyperthermia treatment for deep-seated tumors in the head and neck region. The results demonstrate how the presence of blood flow affects temperature maps starting from a certain SAR distribution. This shows how this effect should be included in simulations and physical phantoms to achieve more realistic temperature predictions.

Both simulations and experimental measurements demonstrate that temperature variations of more than 5°C can occur when blood flow is ignored, underscoring the importance of including vascular dynamics in hyperthermia treatment planning. Future work should focus on refining the physical phantom and to further investigate variable vessel geometries, to reproduce a more detailed discrete vasculature, and to design a more realistic anatomical model.

Chapter 6

Real-time 3D Temperature Reconstruction

This chapter reports the results published in *Nature Communications* [47]. The author's primary contribution focused on developing the method and its application within the in-silico testbed. However, for completeness and consistency with the published article, the application of the proposed method on experimental testbed is also reported in this chapter.

The current limitations oncological microwave hyperthermia mostly come from the inability to reliably predict, and hence control, temperature inside the patient during treatment, especially for deep-seated tumors. Simulations are employed in treatment planning, but due to related uncertainties invasive thermometry is necessary, usually via catheters. Being invasive, their use must be minimized and provides very limited spatial information. Here, we demonstrate an approach to obtain 3D temperature information in real time from few measurement points via massive use of high-performance simulations carried out prior to treatment. The proposed technique is tested both in a fully anthropomorphic in-silico scenario, and in an experimental controlled setting. The obtained results demonstrate the potential of the proposed method as a low-cost real-time temperature monitoring technique in cancer hyperthermia. Use with intra-luminal, minimally-invasive catheters is supported by the positive outcome experimentally obtained using data points directly acquired in the trachea-mimicking phantom structure.

6.1 Introduction

Cancer is one of the major causes of death in the world, and numbers are expected to significantly increase in the coming years also due to the population aging. In this scenario, research into techniques which allow to increase the effectiveness of current treatments and improve the quality of life (QoL) of cancer patients is of

primary importance and urgency.

As already mentioned in Chapter 2, thermal therapies currently play a significant role in cancer treatment, particularly when combined with other treatment methods. Depending on the temperature reached, the treatment duration, and the method of heat administration, heat therapies can be distinguished into microwave hyperthermia, ablation (RF, microwave, ultrasound), and laser therapy. While the aim of ablation is to shrink or destroy tumor cells with temperatures above 60 °C, administered for a duration usually less than 10 minutes [11], microwave hyperthermia (HT) consists in heating the tumor temperature to 42-44 °C for 60-90 min, which results in increased sensitivity of cancer cells to radiation and drugs. HT has been clinically demonstrated as a means for improving the treatment efficacy of radiotherapy and chemotherapy, without increasing their long-term side effects [90, 91, 1, 92, 93], proving particularly useful in the treatment of recurrent cancers [94, 95, 6].

The operational mechanism of hyperthermia consists in focusing the electromagnetic field generated by an antenna applicator on the tumor region, with minimal heating of the surrounding healthy tissues; for deep-seated and sub-superficial tumors, this is achieved using a phased array applicator [18, 96]. Hyperthermia treatment planning (HTP) simulations are used to predict the distribution of specific absorption rate (SAR) and temperature in the treated region of interest (ROI) and find the antenna feeding coefficients which allow to selectively heat the tumor region [38, 69, 71, 37]. This can be obtained by optimizing the SAR distribution in the ROI, using properly defined SAR-based objective functions, or, directly, the temperature; whether one approach is better than the other is still an open question in the scientific community, and both SAR-based and temperature-based optimization routines are nowadays used in the clinical practice leading to comparable results [97]. Although being the basis of HTP, simulations cannot be completely relied on for temperature monitoring, due to the high uncertainty of crucial tissue properties (such as perfusion), and even of some model equations [98, 27, 73, 99].

Currently, the most accurate method of controlling the effective temperature in clinical practice during HT treatments employs probes encased in closed-tip catheters, which provide very limited spatial information [38, 100]. A technology under development is based on measuring the temperature distribution by carrying out thermal treatments inside an MRI environment [101, 102]. MR thermometry is an evolving field, but at present only provides relative temperature change data, is hampered by field heterogeneity, subject to inaccuracies in the presence of (e.g., respiratory) motion, and has difficulties measuring in fatty tissues. Widespread application of MR thermometry is also limited by the high cost of operating MRI scanners, their scarce availability, and the challenges involved in applying thermal therapies inside an MRI system. Other limitations of MR thermometry which affect more ablation than hyperthermia (due to the higher temperatures reached) are the artifacts induced by local susceptibility changes, temperature-induced variations

in tissue electrical conductivity, and gas bubble formation [103, 104]. Electrical impedance tomography (EIT) has also been proposed [105, 106, 107, 108] for non-invasive and cost-effective thermometry, but it relies on sophisticated simulations that suffer from large uncertainties.

The current lack of a method that allows to provide a real-time temperature map in all points of the treated region is therefore evident, and it is a problem that concerns not only HT but all thermal therapies. The method proposed in this article consists in creating a patient-specific set of temperature simulations in the ROI, corresponding to different combinations of the constituent parameters (which are known within large uncertainty ranges), and then match this set to the scarce and limited data provided by a single closed-tip catheter to obtain a realistic 3D temperature map of the patient in real time.

Computations are often not reliable *per se* since a large uncertainty may affect how the parameters describing the underpinning physical system are known [99], and measurements are often scarce and affected by unavoidable noise; hence complementing information from computational science and from experimental measurements has recently gained interest in the broad topic of "digital twin" [109, 110, 111, 112, 113, 114]. This article describes a coherent framework to seamlessly integrate these two sources of information without resorting to the full machinery of Bayesian inference that is often employed—thus avoiding the related computational burden in the online monitoring phase—and provide experimental validation of its performance in the case of temperature monitoring during a hyperthermia treatment using few temperature sensors. We used low-discrepancy sequences for picking the combinations of the constituent parameters when populating the set of patient-specific simulations. We remark that the interest here is in exploring the space of different combinations as much as possible and not in deriving any statistical measure, as it is done in instances of the Monte Carlo method [99].

Few attempts are reported in the literature aimed at enhancing the accuracy of temperature simulations while minimizing invasive thermometry. The approach proposed in this article leverages few measured samples to continuously adapt the predicted temperature distribution to better match the measured data, providing an updated estimate of the patient's temperature in real time. This differs from another method reported in the literature [27, 115], where tissue parameters are estimated by fitting the simulated maps to temperature measurements and used to predict the temperature evolution without any explicit real-time check that the expected temperature matches the real one. Existing approaches that explore the possibility to find a full 3D temperature map require optimization routines to run in post-treatment, involving iterative thermal simulations and measured data [27, 116]; these techniques are indeed not intended to offer a real-time feedback on the actual 3D temperature distribution, but rather to provide benefits in subsequent treatments. The proposed method, conversely, shifts the computational burden to the pre-treatment stage, creating a patient-specific library of temperature maps

that can be used starting from the first application and allows to reconstruct the temperature even in the case where crucial parameters, such as perfusion, vary over time. Another line of research [117] blends a compact representation of the time evolution of the temperature in the ROI (based on a library of simulations, similarly to the method proposed here) with data from MR thermometry. At a difference from the approach proposed in this article, however, that compact representation does not consider the relevant issue of parameter uncertainty and MR thermometry provides more data points than temperature probes in a single closed-tip catheter, at the price of requiring a more complex equipment. As a further difference, the method proposed here may use any code to populate the simulations library, commercial or developed ad-hoc, without assuming a level of access to the inner working of the software used to build the library of temperature maps that is difficult to achieve without developing an in-house code [117].

Tests carried out both in a simulation scenario and in an experimental testbed, specifically built to simulate a hyperthermia treatment in the H&N region are presented in this chapter to prove the feasibility of the proposed method. An estimate of the true state of the system is provided using the limited information from a single catheter, which can also be far from the tumor site and even external to the ROI, i.e. inserted in the part of the phantom that simulates the trachea, so as to mimic a non-invasive intraluminal catheter. The technique demonstrated represents an efficient way of implementing a feasible, real-time, full-3D thermometry in a minimally invasive way (if not even non-invasive in the case of intraluminal catheters). Unlike MR thermometry, the proposed approach also represents a low-cost and easy-to-deploy method, which could favor, in the future perspective, widespread use in the clinic of thermal therapies, leading to a further step forward in the battle against cancer.

6.2 Methodology

The standard HTP approach starts with the generation of a 3D segmented model of the patient, obtained from CT and MRI scans (see Figure 6.1), which is then imported in a multiphysics simulation environment together with the model of the antenna applicator. Numerical solvers in HTP involve the solution of Maxwell's equations and the bioheat thermal equation, using a set of dielectric and thermal parameters. The tissue properties assigned to relevant tissues and organs of the segmented phantom are typically found in the literature, where they are reported with considerable uncertainty [98, 27, 73, 99]. These parameters, here named $\boldsymbol{s}_{base}$ (Figure 6.1), are indeed estimated as averages over different studies and measurements, and their values can vary significantly [27] under HT treatments, being temperature-dependent. The simulated temperature map at time t, indicated as

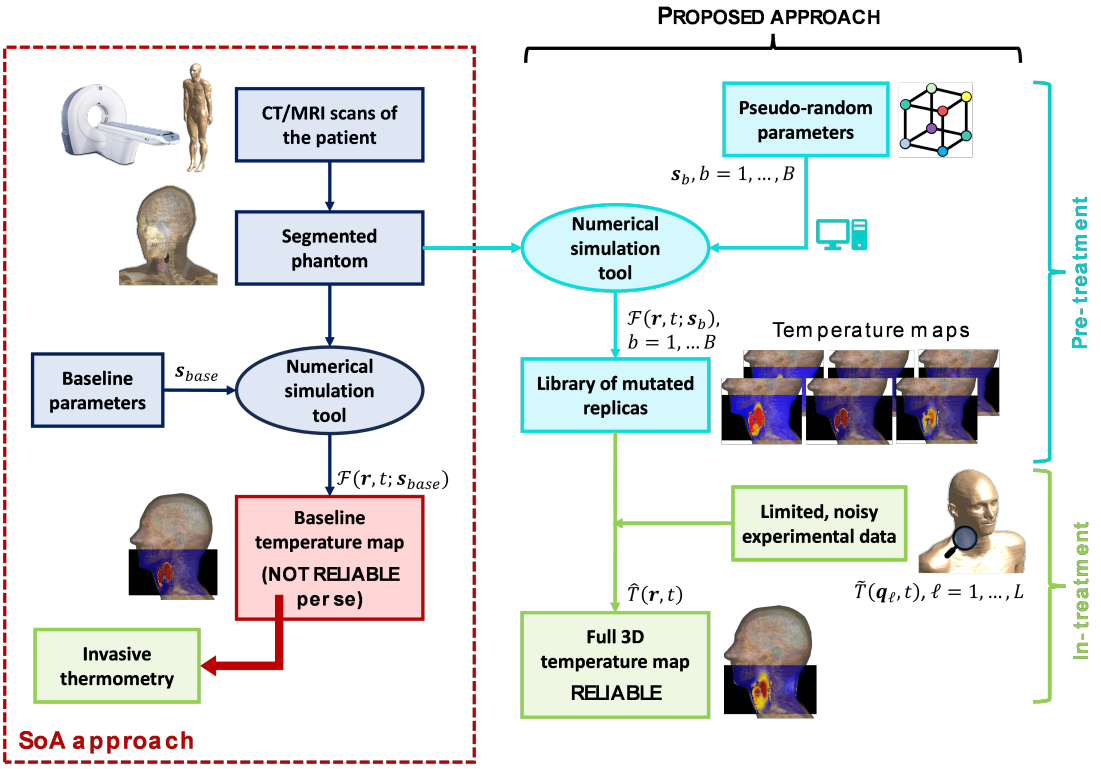

Figure 6.1: Proposed method. Flow chart reporting the approach used nowadays in the clinic to perform HT treatments (State-of-the-Art (SoA) approach) and the proposed methodology.

$\mathcal{F}(\boldsymbol{r}, t; \boldsymbol{s}_{base})$, where $\boldsymbol{r}$ belongs to the set of mesh points in the ROI, is not reliable *per se*, due to the inherently uncertainty affecting the model's constituent parameters. This makes interstitial thermometry advisable during treatment [100], although it allows to control the effective temperature in a very limited number of points—this means that a hotspot that the patient does not yet perceive as pain could be present far from the temperature probes and be dangerous especially in highly thermosensitive regions (e.g., spinal cord).

The technique proposed in this chapter has the goal to use few localized temperature measurements to provide a reliable temperature map at any time and in the whole ROI. As depicted in Figure 6.1, the core of the proposed procedure lies in two fundamental steps:

1) the creation in a pre-treatment stage of a library of multiphysics simulations reproducing the heating process in the ROI, obtained by purposely mutating the constituent parameters $\boldsymbol{s}_b$, $b = 1, \dots, B$, within realistic variation ranges according to a low-discrepancy sequence (Sobol sequences are used);

2) the acquisition of few measurement points $\tilde{T}(\boldsymbol{q}_\ell, t)$, $\ell = 1, \ldots, L$, during treatment. The challenge of providing real-time maps of the temperature in the entire ROI during treatment is then addressed by selecting and combining the elements of the ensemble of multiphysics simulations in the way that best matches the scarce measurement data, leveraging the available data to reduce the uncertainty that affects simulations. The reconstruction process entails recovering the temperature map in the 3D space from a limited (noisy) set of real-time temperature measurements acquired along the direction of a fiber-optic thermometer. From a mathematical point of view, this corresponds to solve a constrained least squares problem involving the set of multiphysics simulations and the scarce available measurement points.

The feasibility of the proposed technique is here demonstrated in two different *scenarios*. The *first* scenario is in a completely in-silico testbed detailed in section 6.3, designed following the ESHO guidelines [14], realized in the simulation software Sim4Life [118] using state-of-the-art anthropomorphic human body phantoms, where the effect of blood perfusion is included. The *second* scenario is an experimental mock-up described throughout this thesis, and in particular detailed in Chapter 3, which has the main purpose of demonstrating the validity of the method in a system affected by real experimental errors. Now we follow up and delve deeper in the details of the proposed method.

As outlined in Section 2.3, in HTP simulations, a set of constituent parameters needs to be assigned to the different tissues forming the patient's segmented phantom within the ROI to solve Maxwell's equations and the bioheat thermal equation. This applies to any situation where the heating of human tissues due to electromagnetic radiation needs to be studied. Concerning the electromagnetic analysis, the essential parameters include the effective conductivity σ (S/m) and the real relative permittivity ε_r (dimensionless). These parameters play a critical role in governing the behavior of electromagnetic fields within the tissues and are essential for accurately predicting the SAR distribution during HT simulations.

It's important to note that the temperature T in (2.11) depends on both time t and the position vector $\boldsymbol{r}$, and tissue-specific parameters $(\sigma, \varepsilon_r, \mu_r, k, \rho, C_p, \omega)$ depend on the position vector $\boldsymbol{r}$.

The thermal model needs to be completed by a proper boundary conditions (B.C.), which describe the thermal interaction of the system with the surrounding environment [89]. After properly defining the ROI, a convective heat flux boundary condition as defined in (3.1), has been used to describe the thermal interaction with the borders of domain.

The temperature distribution extracted following Pennes' Bioheat Equation (2.11) and with properly applied B.C. described in (3.1) is denoted with $T(\boldsymbol{r}, t)$ at the spatial point $\boldsymbol{r}$ and time t.

To describe the mathematical formulation of the proposed method, let us consider L temperature values $\tilde{T}(\boldsymbol{q}_\ell, t)$ are available in the spatial points $\boldsymbol{q}_\ell, \ell = 1, \ldots, L$. These values mimic the temperature measurements from sensors along the catheter and are inherently affected by measurement uncertainties.

Based on these data, our goal is to approximate the temperature distribution $\hat{T}(\boldsymbol{r}, t)$ in the whole ROI as a finite superposition of B reconstruction functions ϕ_b, i.e.:

$$\hat{T}(\boldsymbol{r}, t) = \sum_{b=1}^{B} \mathrm{w}_b(t)\phi_b(\boldsymbol{r}, t), \tag{6.1}$$

where $\mathrm{w}_b(t)$ are the corresponding weights. The reconstruction functions $\phi_b(\boldsymbol{r}, t)$ used in (6.1) are temperature distributions obtained with multiphysics simulations performed according to the clinical practice by reproducing the hyperthermia applicator and the patient's ROI in a simulation environment [39], where a set of constituent parameters is assigned to the model. Indicating with the N-tuple $\boldsymbol{s}_b$ a set of values assigned to N relevant parameters used in the simulation solver, the reconstruction function ϕ_b in (6.1) can be expressed with the notation $\mathcal{F}(\boldsymbol{r}, t; \boldsymbol{s}_b)$, where $\boldsymbol{r}$ belongs to the set of mesh points in the simulated ROI.

The main goal of the proposed method is the possibility to obtain a real-time 3D reconstruction of the temperature distribution in the patient's region of interest (ROI) treated with a hyperthermia applicator, using few spatially-limited (noisy) measurement points acquired along the direction of a fiber-optic thermometer.

To mitigate the ill-posed nature of this inverse problem, regularization techniques are employed. The weights w_b in (6.1) are determined by minimizing the discrepancy between the data points $\tilde{T}(\boldsymbol{q}_\ell, t)$, $\ell = 1, \ldots, L$, and the approximation given by (6.1) evaluated at the same spatial positions and at the same time, namely $\hat{T}(\boldsymbol{q}_\ell, t)$. Among the different regularization techniques tested [119, 120, 121], the most robust method was found to be the linear least squares problem, given by:

$$\min_{\mathrm{w} \in \mathbb{R}^B} \sum_{\ell=1}^{L} \left(\sum_{b=1}^{B} \mathrm{w}_b(t)\mathcal{F}(\boldsymbol{q}_\ell, t; \boldsymbol{s}_b) - \tilde{T}(\boldsymbol{q}_\ell, t) \right)^2 \tag{6.2}$$

with the following additional constraints:

$$\sum_{b=1}^{B} \mathrm{w}_b = 1 \quad \text{and} \quad \mathrm{w}_b \geq 0 \quad \forall b = 1, \ldots, B. \tag{6.3}$$

The constrained least squares (CLS) method expressed by Equations. 6.2 and 6.3 is the approach used in all the examples reported in this article to obtain the reconstructed 3D temperature map 6.1 from a set of few noisy temperature values. This CLS problem is solved using the Matlab routine lsqlin, that recasts the problem as a quadratic one with linear constraints and uses an interior-point method to solve it [122, 123].

6.3 Realistic In-silico testbed

As outlined in HTP guidelines mentioned in Section 2.4, an in-silico testbed was implemented using the simulation software Sim4Life V7.0.2 [118] to reproduce realistic treatment conditions. The simulations were conducted using the fully anthropomorphic Duke V3.0 and Ella cV3.1 phantoms from the Sim4Life virtual population, representing a 34-year-old male and a 26-year-old female body, respectively. These anatomically accurate models were reconstructed from high-resolution MRI data and include 305 segmented tissues with specific dielectric and thermal properties [124].

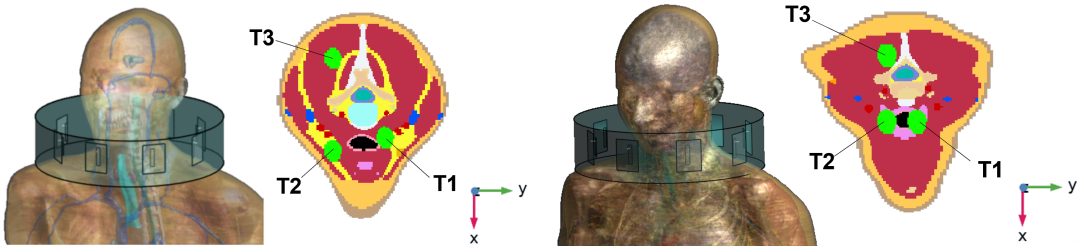

(a) (b)

Figure 6.2: Fully-anthropomorphic phantoms and target positions: (a) Fully-anthropomorphic male phantom Duke V3.0 and different positions of the target region displayed on the xy-plane; (b) Fully-anthropomorphic female phantom Ella cV3.1 and different positions of the target region.

Table 6.1: coordinates of the tumor target centroid.

	x_c **(mm)**	y_c **(mm)**	z_c **(mm)**
Duke, T1	18.02	16.15	1574.9
Duke, T2	28.02	-23.85	1574.9
Duke, T3	-41.98	-23.85	1574.9
Ella, T1	3.02	16.15	1424.0
Ella, T2	3.02	-3.85	1424.0
Ella, T3	-41.98	-3.85	1424.0

The tumor considered in this study is an anatomically realistic, non-uniform target with a shape resembling an irregular prolate spheroid. To investigate spatial variability, three distinct tumor positions were defined across two different phantoms. Figure 6.2 illustrates the spatial distribution of these tumor targets within the phantoms. The centroid coordinates of each tumor target position are reported in Table 6.1. The overall dimensions of the tumor targets are reported in Fig 6.3a.

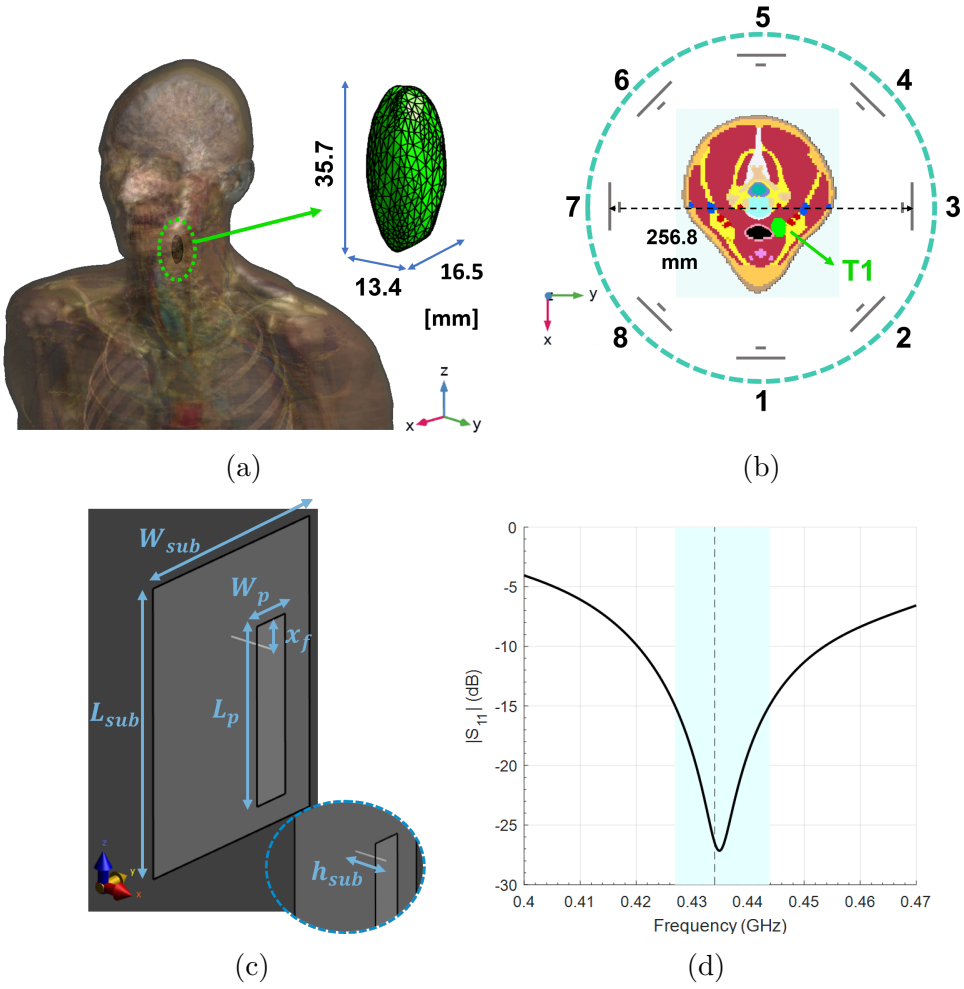

Figure 6.3: (**a**) Fully anthropomorphic phantom Duke and tumor mass with irregular shape inserted in the neck of the phantom; the overall dimensions of the tumor mass are reported in the inset. (**b**) Top view of the phased array applicator surrounding the segmented phantom visualized on the xy plane; the reported number are used to index the antennas of the array; the tumor target (T1) is highlighted in green. (**c**) Employed patch antenna and optimized dimensions. (**d**) Optimized reflection coefficient; a bandwidth (−10 dB) of about 30 MHz is achieved around the central frequency (434 MHz) (dashed line).

Following the HTP workflow, the dielectric properties were assigned to the segmented tissues according to their baseline values, i.e., the values reported in the literature [26], at the operating frequency of 434 MHz.

Later, a common hyperthermia applicator used to treat deep-seated and superficial tumors in the H&N region [18, 59] was reproduced and optimized to heat the target volume placed inside the realistic human phantoms in Sim4Life. As illustrated in Figure 6.3b, the considered HT applicator is a uniform circular

array with a diameter of 256.8 mm consisting of eight patch antennas immersed in water, positioned around the neck of the phantom. The antennas are designed to work in the so-called waterbolus, a doughnut-shaped bag filled with circulating demineralized water at a constant temperature in the range of 20-25 °C , used in the clinical practice to avoid overheating of the skin and favour radiation coupling into the body [125, 66]. The geometrical parameters of the antennas have been optimized to resonate properly at the operating frequency. The dimensions of each antenna, as depicted in Fig. 6.3c, are: $L_{sub} = 50$ mm, $W_{sub} = 40$ mm, $L_p = 31.0$ mm, $W_p = 7.2$ mm, $h_{sub} = 8.4$ mm, and the distance of the feed to the edge $x_f = 4.96$ mm. The reflection coefficient of the optimized antenna element (illustrated in Figure 6.3d), simulated as part of the entire array, shows a bandwidth (-10 dB) of about 30 MHz around the operating frequency (434 MHz), proving to be sufficient for the purposes of the presented simulation study.

First, the antenna feeding coefficients were found by applying an optimization approach briefly reviewed in the section 6.4. The temperature map in the ROI is then obtained after assigning the thermal parameters to the different tissues, setting the thermal boundary conditions, and using the optimized SAR distribution as source term of the bioheat equation. In the in-silico testbed implemented in Sim4Life, thermal boundary conditions were defined in accordance with values reported in the literature [27, 126]. Specifically, a convective heat flux boundary condition (Eq. (3.1)) was applied at the interface between the neck and the waterbolus, with $h = 82$ W/(m$^2 \cdot$ °C) and $T_{ext} = 20$ °C, and on the internal boundary of the trachea, with $h = 50$ W/(m$^2 \cdot$ °C) and $T_{ext} = 30$ °C. Moreover, the initial temperature T_{in} in the tissues was set to 37 °C.

6.4 SAR-based optimization

Following the standard HTP workflow, we begin by optimizing the antenna feeding coefficients of the array applicator using a SAR-based optimization approach, which is commonly employed in hyperthermia [69]. This process determines the optimal amplitude and phase settings that maximize power deposition in the tumor while minimizing heating in surrounding healthy tissues. The same optimization procedure described in Section 4.2 was applied here to the in-silico testbeds and required 13.7 thousand iterations and 39 min to reach the convergence on an Intel Core i7-7700 workstation, with 64 GB RAM.

The optimized sets of feeding coefficients are reported in Table 6.2 for two phantoms (Duke and Ella) and 3 target positions (T1,T2 and T3).

The simulated SAR distribution corresponding to the optimized set of phases and amplitude is shown in Fig. 6.4 for target position T1 and both phantoms Duke (top row) and Ella (bottom row), with the input power $P_0 = 52$ W and $P_0 = 63$ W respectively. The total input power for each phantom has been set to achieve a

sufficient of $T50$ parameter of 42 °C and a maximal healthy tissue temperature of 43 °C [127], using the baseline thermal tissue parameters [26].

Table 6.2: optimized antenna amplitudes and phases for different phantoms and target positions.

	n	1	2	3	4	5	6	7	8
Duke, T1	ν_n (-)	0.70	0.90	0.90	1.00	0.83	0.74	0.10	0.90
	φ_n (°)	-46.27	-31.21	0.01	51.10	84.70	86.33	77.15	26.90
Duke, T2	ν_n (-)	0.54	0.79	0.74	0.48	0.60	0.68	0.94	0.89
	φ_n (°)	0.00	130.18	-143.44	-152.53	-163.35	151.14	43.99	0.00
Duke, T3	ν_n (-)	0.00	0.60	0.94	0.51	0.86	0.81	0.84	0.48
	φ_n (°)	15.84	-75.03	-125.11	122.32	0.00	0.00	78.52	-131.00
Ella, T1	ν_n (-)	0.72	0.65	0.72	0.90	0.82	0.85	0.68	0.69
	φ_n (°)	0.00	-15.81	0.00	59.95	110.50	115.63	88.24	53.69
Ella, T2	ν_n (-)	0.43	0.90	0.71	0.96	0.91	1.00	0.79	0.85
	φ_n (°)	0.00	-35.39	0.00	38.46	71.82	63.63	0.00	-14.76
Ella, T3	ν_n (-)	0.30	0.63	0.56	0.49	0.54	0.88	0.28	1.00
	φ_n (°)	-151.42	-150.71	164.35	25.64	11.20	35.28	102.67	-175.59

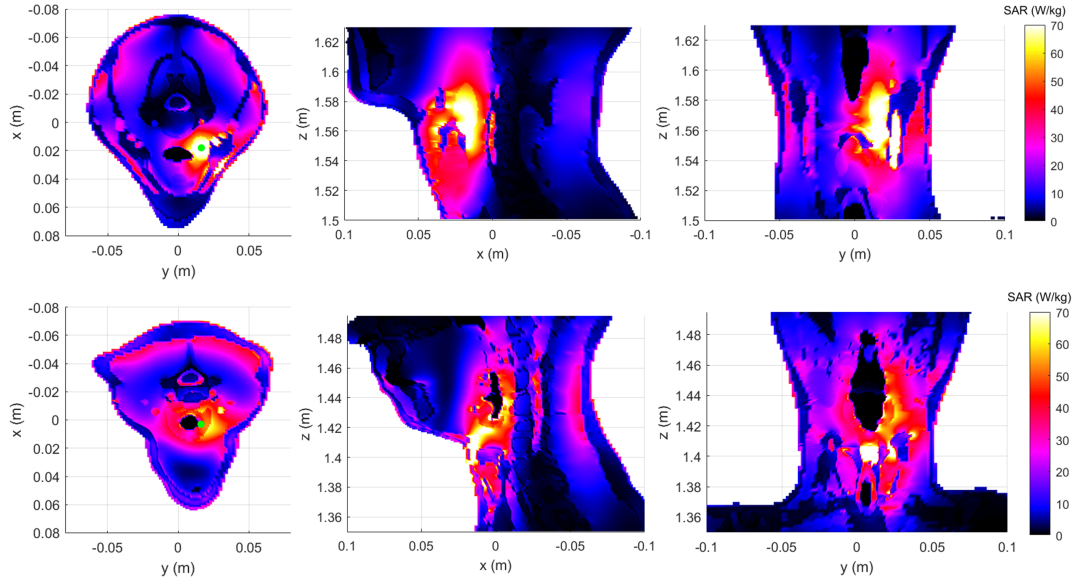

Figure 6.4: Optimized SAR distribution simulated in Sim4Life for both phantoms Duke (top row) and Ella (bottom row), displayed on the three canonical planes cutting the tumor sphere at its centroid. The green dot on the SAR distribution displayed on the xy plane indicates the position T1 of the tumor's centroid.

6.5 Validation of the method using the in-silico testbed

Among the dielectric and thermal parameters assigned to the different tissues of the phantom, perfusion is crucial for the calculation of the temperature profile, being characterized by the largest uncertainty [73].

In the considered testbed, the proposed method described in Section 6.2 is applied to mitigate the uncertainty introduced by thermal conductivity (k) and perfusion (ω) of the most relevant tissues in the ROI (i.e., muscle, fat + subcutaneous adipose tissue (SAT), skin and tumor). To build the library of multiphysics simulations the selected 8 parameters (two thermal parameters for each of the four tissues) are changed by employing a Sobol sequence to explore the parameters space within the ranges of variation reported in Table 6.3 (in accordance with what is reported in the literature), while the other properties are assigned to the tissues according to their baseline values [26]. Choosing rather wide ranges for the considered parameters as reported in Table 6.3 allows the method to handle their uncertainty even under thermal stress.

The goal of this process is to determine the temperature values at a given point $\boldsymbol{r}$ based on a set of parameters $\boldsymbol{s}$. Since the steady-state form of the bioheat equation is employed in this case, we adopt the notation t_{ST} instead of t in the previously

Table 6.3: Considered tissues' properties, baseline values, and the extreme range of the variation

	k (W/m°C)			ω (ml/(min kg)))		
Tissue	Baseline	min	max	Baseline	min	max
Muscle	0.49	0.40[a]	0.56	39.1[b]	19	442.8[a]
Fat(+SAT)	0.21	0.18	0.50[a]	33	20	255[a]
Skin	0.37	0.32	0.50	106	49	175
Tumor	0.51[a]	0.41[c]	1.5[a]	72.3[b]	36.15[d]	848[a]

The values without a specific reference are derived from the IT'IS database [26]. The values marked as **a**: are derived from [27], the values marked as **b**: are derived from [53]. The lower bounds of thermal conductivity (k) and perfusion (ω) for the tumor have been fixed proportionally to the percentage of variation in the corresponding skin ranges, i.e., **c**: 80% of the baseline value; **d**: 50% of the baseline value.

defined time-dependent expression $\mathcal{F}(\boldsymbol{r}, t; \boldsymbol{s}_b)$, to explicitly indicate that a steady-state solution is considered. Accordingly, the resulting steady-state temperature map evaluated at a given spatial position $\boldsymbol{r}$ for a specific set of input parameters $\boldsymbol{s}$ is denoted as $\mathcal{F}(\boldsymbol{r}, t_{ST}; \boldsymbol{s})$. To achieve this, we utilized two distinct Sobol' sequences. The first sequence, denoted as $\boldsymbol{s}_b$ for $b \in \{1, \ldots, B\}$, was used to generate $B = 70$ reconstruction functions (ϕ_b in Eq. 6.1). These functions serve as the basis for approximating the temperature distribution. Using a desktop computer with i7-7700 processor and 64 GB RAM, the computation of this set of maps took less than 5 hours, considering 3.771 MCells in the ROI. The second sequence, denoted as $\boldsymbol{\xi}_a$ for $a \in \{1, \ldots, A\}$, was employed to create the *target maps*—synthetic temperature distributions corresponding to parameter sets that are treated as "unknown", which we want to reconstruct in the entire ROI using few known temperature values affected by noise. Figure 6.5 shows a comparison between the temperature map obtained by using the baseline values of the parameters $\boldsymbol{s}_{base}$, i.e., $\mathcal{F}(\boldsymbol{r}, t_{ST}; \boldsymbol{s}_{base})$, and two target maps indicated as $\mathcal{F}(\boldsymbol{r}, t_{ST}; \boldsymbol{\xi}_a)$, a = 1,2, clearly showing how parameters variation can lead to significantly different temperature predictions in the ROI. The objective is to reconstruct these target maps (as indicated with $\mathcal{F}(\boldsymbol{r}, t_{ST}; \boldsymbol{\xi}_a)$) across the entire ROI using a limited number of noisy temperature measurements.

To emulate realistic acquisition conditions, the proposed reconstruction method assumes access only to temperature values at discrete limited spatial points $\boldsymbol{q}_\ell$, $\ell = 1, \ldots, L$, located along a catheter. These values are affected by measurement noise, modeled according to a Gaussian distribution with mean μ and standard deviation σ. The noisy temperature data used for reconstruction are thus given by:

$$\tilde{T}(\boldsymbol{q}_\ell, t_{ST}) = \mathcal{F}(\boldsymbol{r}, t_{ST}; \boldsymbol{\xi}_a) + f_{\mathcal{N}}(\boldsymbol{q}_\ell; \mu, \sigma^2), \tag{6.4}$$

here, $f_{\mathcal{N}}$ is a function generating an array of random errors, normally distributed

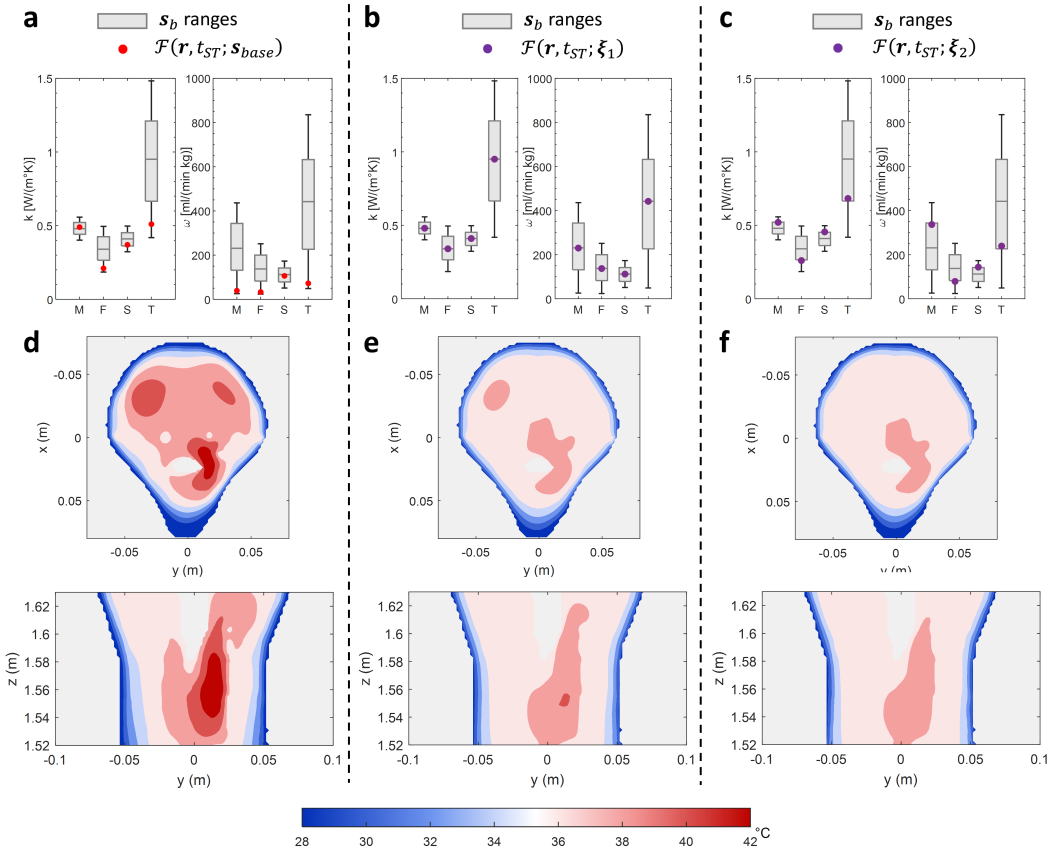

Figure 6.5: Temperature maps variation. (a-c) Boxplots showing the distribution of the considered sets of thermal parameters (k and ω) of the four most significant tissues in the ROI (i.e., muscle (M), fat + SAT (F), skin (S) and tumor (T)). The dots show the set of parameters corresponding to the baseline values (a), and two target sets, $\boldsymbol{\xi}_1$ (b) and $\boldsymbol{\xi}_2$ (c). (d-f) Temperature maps obtained from steady-state bioheat equation, displayed on the xy (upper row) and the yz (lower row) planes passing through the tumor at its centroid, corresponding to: (d) the baseline set of parameters $\boldsymbol{s}_{base}$; (e) the target set $\boldsymbol{\xi}_1$; (f) the target set $\boldsymbol{\xi}_2$.

with mean μ and variance σ^2. In this study, the noise parameters were fixed to $\mu = 0.1°\text{C}$ and $\sigma = 0.2°\text{C}$, according to the characteristics of the experimental setup and FBG sensing system described earlier in this thesis. This noise model accounts for the uncertainties introduced by the acquisition process and sensor limitations.

To assess the robustness of the proposed method in the presence of noisy data, we introduce the following goodness function $g(\chi)$:

$$g(\chi) = \frac{\text{Vol}\left(\{\boldsymbol{r} \in \text{ROI} : \Delta T \leq \chi\}\right)}{\text{Vol}\left(\text{ROI}\right)}, \tag{6.5}$$

where ΔT denotes the absolute temperature difference between the Target temperature map and the reconstructed map $\hat{T}(\boldsymbol{r}, t)$ within ROI. The function $g(\chi)$ thus represents the relative size of the region where the absolute difference ΔT is below a certain threshold χ (°C). It should be noted that $g(\chi) = 1$, $\forall \chi$, denotes perfect reconstruction.

Considering Duke phantom and target in position T1, we performed the reconstruction of the considered target maps using L acquisition points $\boldsymbol{q}_\ell, \ell = 1, \ldots, L$, equally distributed along a direction (x or y) passing through the tumor's centroid, as depicted in Figure 6.6b. The reconstructed target maps are obtained with the CLS method (Eqs. 6.2 and 6.3 of the section 6.2), using $B = 70$ reconstruction functions and 2000 realizations of Gaussian noise (see Eq. 6.4). The target maps considered in Figure 6.6 correspond to two examples of Sobol's extraction of the parameters $\boldsymbol{\xi}_a$ already visualized in Fig. 6.5. For each of the considered cases, the normalized goodness function $g(\chi)$ is reported in Figure 6.6 when the reconstruction is performed without noise (blue-dot line), and for the different realizations of the Gaussian noise (see the envelope). The curves corresponding to the median and the 95th percentile of the functions $g(\chi)$ evaluated for the different noise realizations are also reported, together with the function $g(\chi)$ obtained by considering the baseline temperature map (red-dot line). As can be observed, for all the considered cases, the curves corresponding to the 95th percentile in Figure 6.6e indicates that 95% of the ROI has an error lower than 1°C for 95% of the realizations.

When a large set of cases is included in the study, we denote as $L(\chi, \zeta)$ the likelihood that a specified fraction (ζ) of the ROI has an error below a certain threshold χ, i.e.,$L(\chi, \zeta) = \mathbb{P}(g(\chi) \geq \zeta)$, where $g(\chi)$ is the normalized goodness function defined in (6.5). We finally indicate as χ_{95} the minimum χ such that $L(\chi,0.95) = \mathbb{P}(g(\chi) \geq 0.95)$, which represents the minimum error threshold χ such that there is a 95% chance of having at least 95% of the ROI with an error lower than χ (among the number of cases considered). Lower values of χ_{95} correspond to a better reconstruction.

In the more general study reported in Figure 6.7, the reconstruction procedure was implemented by performing 10 permutations of 256 elements of a Sobol' sequence, such that 70 maps served as reconstruction functions, while the remaining maps were treated as target maps. This was repeated for 3 tumor positions (See Table 6.1), two phantoms (Duke and Ella), 100 noise realizations and 8 catheters configurations (See Fig. 6.7a) arranged along the $x-$ and $y-$axes starting from $z_c - 20$ mm to $z_c + 10$ mm, being z_c the z-coordinate of the tumor centroid. Table 6.4 reports the number of sensors along the considered catheters (i.e., the number of acquisition points $\boldsymbol{q}_\ell, \ell = 1, \ldots, L$, used in the reconstruction) for two different sensor spacings: 6 mm and 2 mm. The table also specifies the catheter orientation — $\boldsymbol{x}$ indicates catheters aligned along the x-axis at $y = y_c$, while $\boldsymbol{y}$ indicates catheters aligned along the y-axis at $x = x_c$, where (x_c, y_c) are the tumor centroid coordinates in the xy-plane — and their positions along the z-axis relative to the

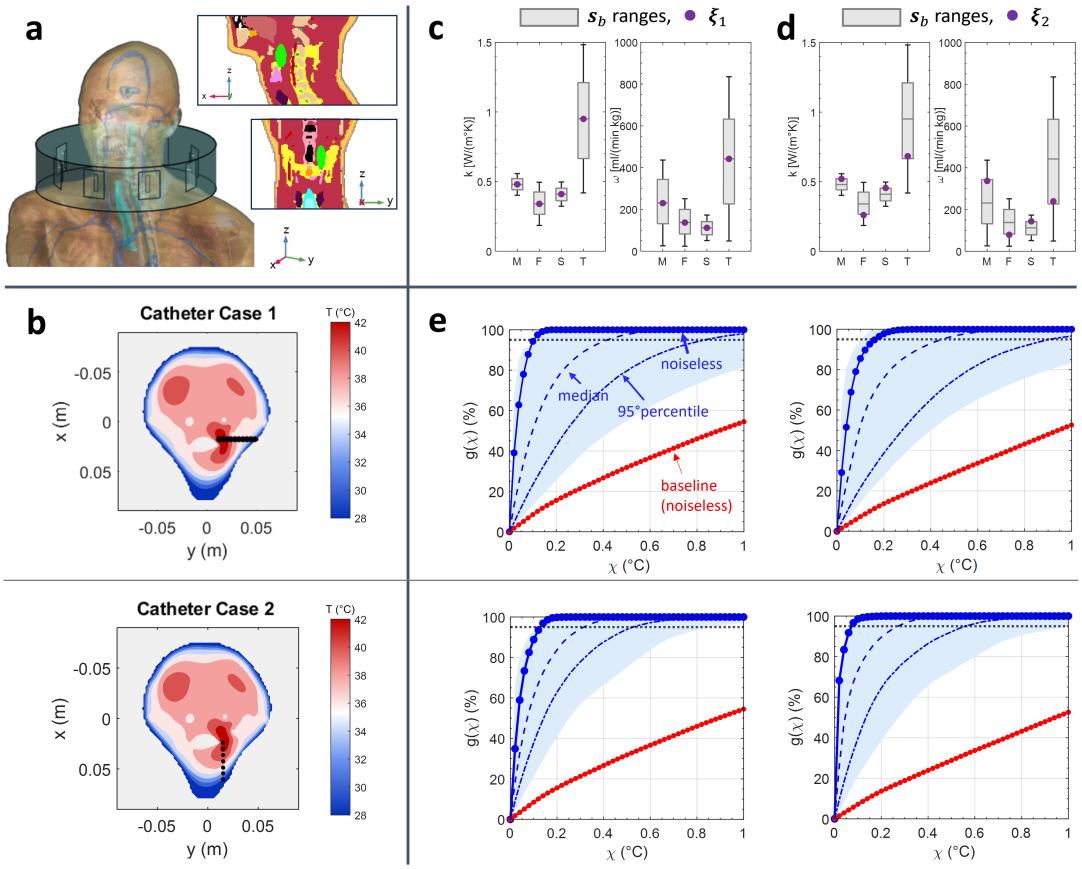

Figure 6.6: visualization of the reconstruction error for two target maps and different number of points along the catheter. (a) The phantom Duke employed to simulate an HT treatment; the insets show the tumor target position T1 (highlighted in green). (b) Different configurations of the acquisition points $\boldsymbol{q}_\ell$ in the transversal (xy) plane passing through the tumor at its centroid (showed on the baseline map); where the number of points considered are: L= 20 (case 1) and 7 (case 2). (c, d) Boxplots showing the distribution of the considered sets of thermal parameters (k and ω) corresponding to key tissues in the ROI (M = muscle, F = fat + SAT, S = skin, T = tumor); superimposed blue dots represent the combinations of parameters $\boldsymbol{\xi}_a$ of two target maps, $a = 1$ (c), $a = 2$ (d). (e) Normalized goodness function $g(\chi)$ (see Equation 6.5): rows refer to the catheter cases (b), and columns represent the target maps (c, d); the blue-dot line corresponds to the reconstruction of the target map without noise, the blue-shadow region includes 2000 realizations of the Gaussian error $f_{\mathcal{N}}$, with $\mu = \pm 0.1°\text{C}$ and $\sigma = 0.2°\text{C}$, with the blue dashed line denoting the median and the dash-dotted line indicating the 95th percentile, the red-dot line expresses the discrepancy between the target field and the baseline map.

tumor centroid z-coordinate (z_c).

In the analysis reported in Figure 6.7d, we considered 40 target maps obtained by varying the effective conductivity and the real relative permittivity of muscle, fat (+SAT), skin and tumor according to a Sobol sequence within ±20% and ±10% of their baseline values [99], respectively, and 8 target maps corresponding to a displacement of the phantom of $(-5, -2, +2, +5)$ mm along the vertical z-axis.

Table 6.4: Position and characteristics of the 8 catheters used for each tumor's position; z_c is the z-coordinate of the tumor centroid.

Catheter	**Sensors** (6mm spacing)	**Sensors** (2mm spacing)	**Direction**	**z (mm)**
1	7	20	$\boldsymbol{y}$	z_c
2	8	23	$\boldsymbol{x}$	z_c
3	7	20	$\boldsymbol{y}$	$z_c + 10$
4	10	30	$\boldsymbol{x}$	$z_c + 10$
5	7	20	$\boldsymbol{y}$	$z_c - 10$
6	6	18	$\boldsymbol{x}$	$z_c - 10$
7	7	20	$\boldsymbol{y}$	$z_c - 20$
8	6	18	$\boldsymbol{x}$	$z_c - 20$

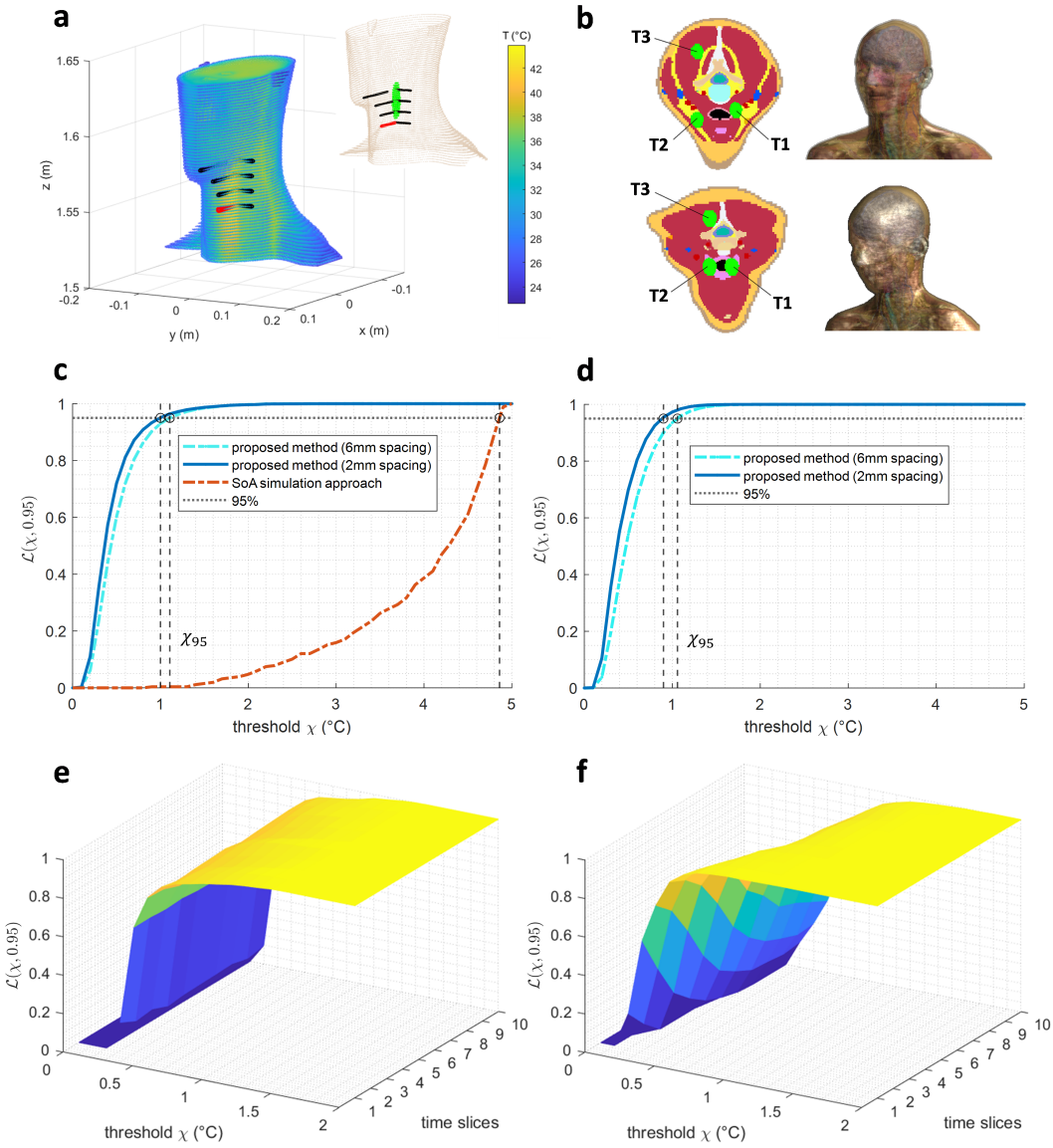

Figure 6.7: General validity and robustness of the proposed method. (a) Candidate catheter positions considered for the single catheter, e.g., the red one in the picture, inserted in the ROI of the anthropomorphic phantoms and used for the reconstruction. (b) Different positions of the tumor target regions in the two phantoms Duke (top) and Ella (bottom). (c-d) $L(\chi,0.95)$ where the reconstruction procedure is applied to a large number of cases, involving 1860 combinations of the target and reconstruction maps, 100 noise realizations and the two phantoms with different tumor's positions (c), and to a set of target cases that exhibit variations in the dielectric parameters, as well as in the phantom geometry (d). (e-f) $L(\chi,0.95)$ obtained at different times by considering transient reconstruction functions, the phantom Duke with the tumor in position T1, 100 noise realizations, 8 catheters configurations and two target maps: (e) $\mathcal{F}(\boldsymbol{r}, t; \text{Model1})$ and (f) $\mathcal{F}(\boldsymbol{r}, t; \text{Model2})$.

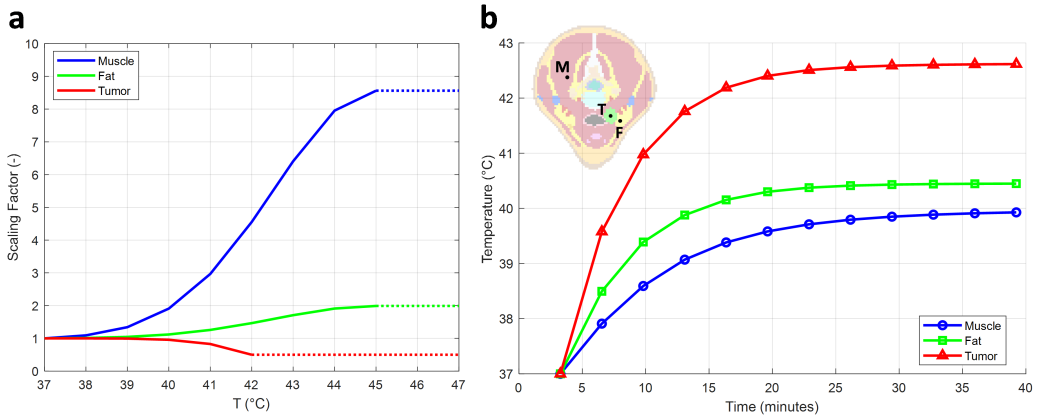

Figure 6.8: Piecewise linear temperature dependent perfusion model. (a) Perfusion scaling factors used for muscle, fat (+SAT), and tumor [53, 128]. (b) Simulated temperature evolution of the target map $\mathcal{F}(\boldsymbol{r}, t; \text{Model2})$ in the indicated probe points for the phantom Duke with the tumor in position T1.

For the transient study presented in Figure 6.7e and Figure 6.7f, we considered 140 reconstruction functions ($\mathcal{F}(\boldsymbol{r}, t; \boldsymbol{s}_b)$) solving the transient Pennes' bioheat equation with constant perfusion values, at 10 evenly spaced times between 6 min and 36 min after the power-on, the reconstruction was performed in 800 cases, obtained by considering 100 noise realizations and 8 catheters configurations with a 6 mm spacing between the sensor points.(Figure 6.7a). Two different transient target temperature maps, $\mathcal{F}(\boldsymbol{r}, t; \text{Model1})$ and $\mathcal{F}(\boldsymbol{r}, t; \text{Model2})$ were extracted from Sim4Life to demonstrate the robustness of the method when different perfusion models are considered. The first target $\mathcal{F}(\boldsymbol{r}, t; \text{Model1})$ is derived from optimized thermal parameters reported in the literature [27], employing a constant perfusion model for each tissue type. The corresponding perfusion values are $\omega = 442.8\,,255\,,848$ (ml/(kg $\cdot$ min)), and thermal conductivities are $k = 0.4\,,0.5\,,1.5$ (W/m°C) for muscle, fat (+SAT), and tumor tissues, respectively. The second target, $\mathcal{F}(\boldsymbol{r}, t; \text{Model2})$, follows a piecewise linear temperature dependent perfusion model [53, 128] for muscle, fat (+SAT), and tumor tissues, as shown in Figure 6.8a.

In this approach, the local perfusion at a given temperature is obtained by multiplying the baseline perfusion at 37 °C ($\omega_0 = 39.1\,,32.7\,,72.3$ ml/(kg $\cdot$ min)) for muscle, fat (+SAT), and tumor tissues, respectively) with the temperature-dependent scaling factor shown in Figure 6.8a. Figure 6.8b presents the temperature evolution of the target map $\mathcal{F}(\boldsymbol{r}, t; \text{Model2})$ at three distinct probe locations, placed in the muscle, fat (+SAT), and tumor tissues (see the inset).

Table 6.5: Median and inter-quartile range (IQR) of the standard estimators using the proposed method and the SoA approach

Case study		$\Delta T50$ (°C)			$\Delta T90$ (°C)		
		Method (2 mm)	**Method** (6 mm)	**SoA**	**Method** (2 mm)	**Method** (6 mm)	**SoA**
Figure 6.7c	Median	0.2	0.2	3.7	0.2	0.2	4.2
(8.9M cases)	IQR	0.4	0.4	4.7	0.4	0.4	4.5
Figure 6.7d	Median	0.2	0.2	3.2	0.2	0.2	3.6
(38.4k cases)	IQR	0.2	0.3	0.5	0.3	0.3	0.5

6.6 Discussion of the in-silico results

In addition to the proposed metrics introduced in Section 6.5, it is important to evaluate standard hyperthermia metrics commonly used in the literature to comprehensively assess the accuracy of the reconstruction results. In this section, we introduce these standard metrics—alongside the previously presented ones—for a more thorough discussion and comparison.

To this end, we consider the median of the absolute temperature difference ΔT between the target map and the reconstructed temperature map $\hat{T}(\boldsymbol{r}, t)$ in the ROI, and the absolute difference of the T50 and T90 parameters [27, 14], i.e., the temperature exceeded by 50% and 90% of points in the tumor region. Although these median values are measures of inaccuracy, we will refer to them as accuracies as common in the related literature [27].

As previously mentioned, the result reported in Figure 6.6 is concerning the application of the proposed method to two target maps, for two different set of the points used for the reconstruction and 2000 realizations of the Gaussian error ($\mu = \pm 0.1$°C and $\sigma = 0.2$°C). The curves displayed in Figure 6.6e clearly show that the error obtained by reconstructing the target maps with the proposed method is on average lower that 0.6°C in 95% of the ROI, in each of the reported cases (see the dashed blue lines), although the scarce points used in the reconstruction are affected by noise. Figure 6.6e also shows that 95% of the ROI has an error lower than 0.9°C for 95% of the realizations. Moreover, for all the considered noise realizations (blue shaded region), the achieved error is always significantly lower than what would be obtained by simply using the baseline values (red-dot line). The accuracy of the reconstructed temperature can be quantified by the median of the difference ΔT evaluated over the noise realizations, which is always lower than 0.1°C—while reaches about 0.9°C when the baseline map is used. The T50 and T90 parameters can instead be predicted with a median accuracy lower than 0.4°C and 0.3°C, respectively, with the proposed method, and higher than 3°C using the baseline map.

To provide a more comprehensive demonstration of the proposed method, we

applied the reconstruction procedure in a vast set of cases including 8 catheters configurations (see Figure 6.7a), 1860 combinations of the target and reconstruction maps, 100 noise realizations, reproduced for 3 different positions of the tumor target in the phantom Duke and Ella (Figure 6.7b). In each case, the reconstruction was performed using a single catheter, and a set of spatial points $\boldsymbol{q}_\ell$ spaced 2 mm and 6 mm apart. This results in 18 to 30 sensor points along each catheter in the first case, and 6 to 10 points in the second case, depending on the position considered. The χ_{95} parameter evaluated over this large set of cases is visualized in Figure 6.7c: it is lower than 1.1°C with the proposed method while can reach 4.9°C using the baseline map. The feasibility of the proposed approach within this large set of cases can be quantified by the T50 and T90 estimators (Table 6.5): these parameters can be predicted with a median accuracy of 0.2°C with the proposed method, reaching about 4°C using the baseline map. Further increasing the spacing between the sensors to approximately 1 cm, resulting in only 4 sensors along the single catheter [16], the accuracy of the T50 and T90 parameters does not change significantly (0.3°C, IQR 0.5°C).

To investigate the robustness of the proposed technique when some of the patient parameters are not included in the library of multiphysics simulations, we applied our method to a set of target cases that exhibit variations in the dielectric parameters compared to the baseline values, as well as in the phantom geometry. We considered 8 catheters configurations (see Figure 6.7a), 100 noise realizations, and 48 target maps including the unexpected variations (See Sec. 6.2), using the Duke phantom with the tumor in the position T1 (Figure 6.7b). We introduced variations of 10%-20% in the dielectric parameters, and geometric displacements in the range ±5 mm. The computed χ_{95} parameter (0.9°C, Figure 6.7d) and the standard estimators (Table 6.5) confirm the effectiveness of the reconstruction process.

While it cannot be formally excluded the existence of two sets of parameters that correspond to two temperature distributions that are similar at the measuring positions—and thus indistinguishable—and different at all the other locations, this extensive numerical investigation shows that such problematic cases occur very rarely, if they even occur at all, as the proposed method can reconstruct the temperature distribution on a large portion of the ROI (95%) in almost all the tested cases (95%) with an error lower that 1.0°C.

The method's capability to reconstruct temperature in real-time and manage nonlinearities in key tissue parameters, such as perfusion, is demonstrated in Figures 6.7e and 6.7f, where transient thermal reconstruction functions are used to reconstruct two target maps [53]: one with constant perfusion—as done so far—and the other incorporating a piecewise linear temperature dependent perfusion for muscle, fat and tumor. For both target maps, the reconstruction was performed in 800 cases, obtained by considering the phantom Duke with the tumor in position T1, 100 noise realizations and 8 catheters configurations with 6 mm spacing. The

computed χ_{95} parameter is always lower than 1°C for all the considered times (Figures 6.7e and 6.7f), while the T50 and T90 parameters show a median accuracy in the range 0.1÷0.3°C (IQR 0.2°C) for both target maps.

6.7 Experimental Testbed

To experimentally validate the proposed technique, a fully functional mock-up reproducing a hyperthermia treatment in the H&N region was developed. The experimental setup and its digital twin, implemented in COMSOL Multiphysics, have been comprehensively described in Chapter 3.

To enhance the realism of the reproduced phantom, as detailed in Chapter 5, a system of pipes with flowing water was inserted in the neck phantom to reproduce the cooling effect of blood flow in the major vessels, i.e., the jugular veins and carotid arteries.

The dielectric and thermal properties of the material used in the model of the prototype at 434 MHz were experimentally characterized in our laboratories [49], and their measured values are reported in Table 3.4.

A SAR-based optimization approach (detailed in Chapter 4) was used to find the set of antenna coefficients which maximize the deposited power (SAR) in a target region while minimizing the presence of hotspot in surrounding healthy tissues (See Table 4.3).

To measure the temperature at different locations within the realized mock-up and in real time, a system of Fiber Optic Sensors (FOS) based on Fiber Bragg Grating (FBG) sensors was employed (detailed in Sec. 3.3.1). The FBG arrays were inserted along the vertical (z) axis, as illustrated in Fig. 3.8b. The positions of the inserted arrays on the xy-plane are shown and numbered in the inset of Fig. 6.9. Table 6.6 reports the xy-plane coordinates of the used arrays (numbered as in the inset of Fig. 6.9) together with the positions along the z-axis of the corresponding FBG sensors. The Array 2 was inserted in the center of the tumor target sphere, while the Array 5 was positioned in the hollow cavity of the cylinder reproducing the trachea.

Figure 6.9 reports the temperature measurements read by the arrays of FBG sensors at the beginning (top row) and at the end (lower row) of the heating session,

Table 6.6: Coordinates of the FBG sensors along the different arrays.

Array	x (mm)	y (mm)	z (mm)
1	33.94	33.94	(25, 20, 15, 10, 5, 0, -5, -10, -15, -20, -25, -30, -35, -40)
2	-20	-18	(40, 30, 20, 15, 10, 5, 0, -5, -10, -15, -20, -30, -40)
3	0	-18	(40, 30, 20, 15, 10, 5, 0, -5, -10, -15, -20, -30, -40)
4	20	-18	(40, 30, 20, 15, 10, 5, 0, -5, -10, -15, -20, -30, -40)
5	0	-37	(40, 30, 20, 15, 10, 5, 0, -5, -10, -15, -20, -30, -40)

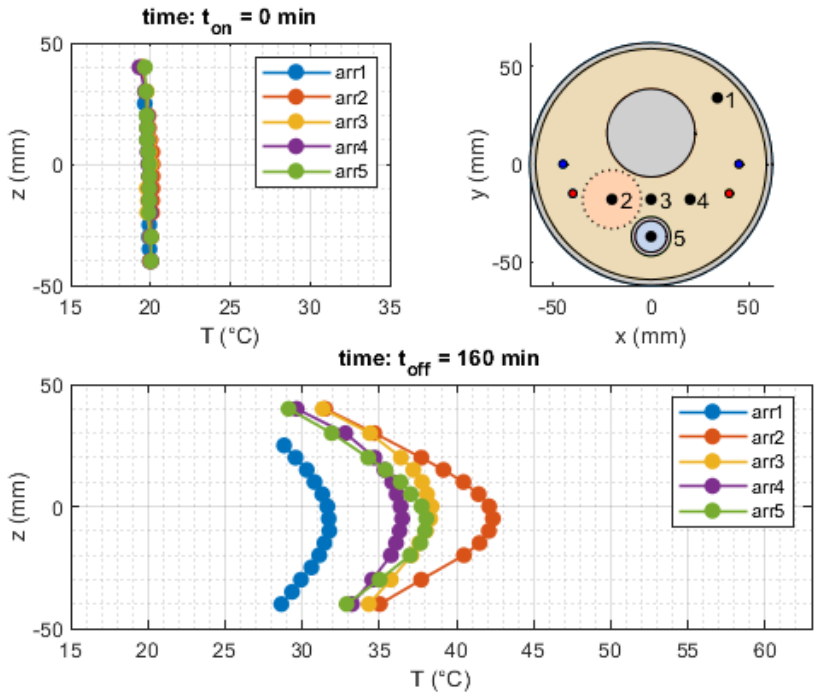

Figure 6.9: Temperature read by the arrays of FBG sensors at the beginning (upper row) and at the end (lower row) of the heating session; the position of the different arrays on the xy plane is indicated in the upper row (right picture) and reported in Table 6.6, together with the z-coordinates of the corresponding FBG sensors.

where $t_{on} = 0$ min and $t_{off} = 160$ min respectively indicate the moments at which the power supply (60 W) was turned on/off. As can be observed, at the initial time, all sensors were almost at the same temperature, proving that the system was at the thermal equilibrium with an average initial temperature $T_{in} = 20$ °C. At the final time t_{off}, the temperature on the Array 2 placed in the tumor sphere is at its maximum approximately 10°C higher than on the Array 1, which is the most distant from the target region. This confirms how the feeding coefficients obtained by maximizing the SAR in the tumor sphere led to a selective and significant heating of the target region.

As previously described in Sec. 3.3.2, to obtain an ideal simulation model (i.e., the "digital twin") of the implemented prototype, a realistic boundary condition analysis was performed in COMSOL. Convective heat flux boundary conditions, as defined in Eq. (3.1), were applied at all relevant interfaces, including the phantom upper boundary–air (h_{tn}), phantom lower boundary–air (h_{bn}), and phantom lateral walls–water bolus (h_{wb}). The initial temperature in the simulated phantom was fixed according to the average temperature measured by the FBG sensors at the beginning of the heating session, namely $T_{in} = 20$ °C (see Fig. 6.9, time $t = t_{on}$). The external reference temperatures T_{ext} in Eq. (3.1) were set to 21 °C for the

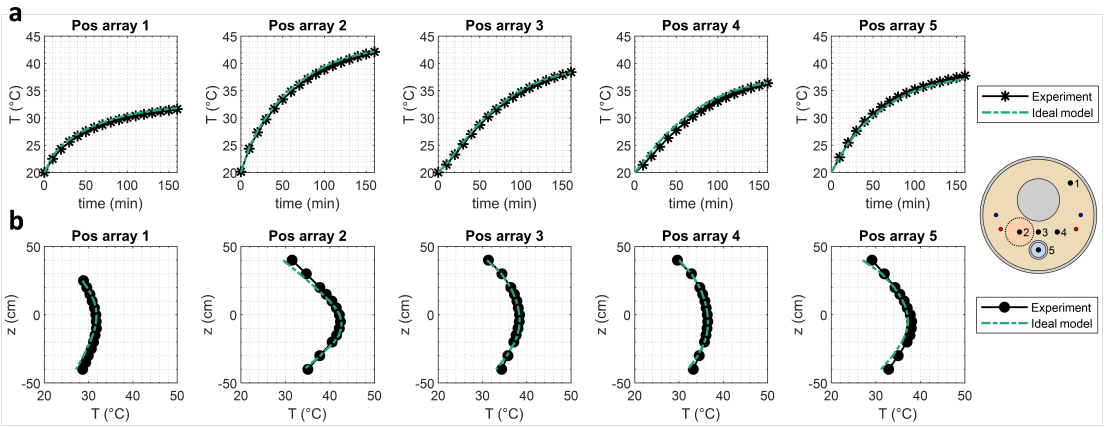

Figure 6.10: Measured temperatures and simulated values corresponding to the COMSOL model that best reproduces the experimental mock-up in correspondence of the different arrays' positions ("Pos") on the xy-plane, (a) as a function of time at $z = z_t = 0$ mm, and (b) as a function of the z-coordinate at $t = t_{off} = 160$ min.

surrounding air and 19.8 °C for the waterbolus, as measured during the heating session. Furthermore, an additional convective heat flux boundary condition was applied at the outer surfaces of the silicone pipes reproducing the main vessels, using a heat transfer coefficient of $h = 10$ W/(m^2 °C) and a controlled external temperature of 25.6 °C to account for the cooling effect induced by vessel-mimicking pipes. The final heat transfer coefficients adopted in the ideal simulation model were $h_{tn} = 30$ W/(m^2 °C), $h_{bn} = 20$ W/(m^2 °C), $h_{wb} = 55$ W/(m^2 °C), and $h_{pipes} = 10$ W/(m^2 °C).

Fig. 6.10a shows the comparison between the ideal model estimations and the experimental measurements as a function of time, at the target's center z-coordinate ($z = z_t = 0$ mm), for 17 time samples equally distributed from $t_{on} = 0$ min and $t_{off} = 160$ min. Fig. 6.10b reports the same comparison for all the points along each array, at the end time $t = t_{off} = 160$ min. As can be observed, a good agreement is obtained, which allows on one hand to validate the implemented modeling approach, and on the other hand to set a bound on the achievable accuracy when the COMSOL model is used to reproduce the experiment in the best possible (ideal) scenario, i.e. when all the available measurement points are known.

6.8 Validation of the Method Using the Experimental Testbed

Following the procedure previously applied to the in-silico anthropomorphic model, the information along a single array inserted in the phantom is used to

Table 6.7: measured dielectric properties of the materials used in the prototype and ideal estimates of the heat transfer coefficients with the corresponding variation ranges.

	ε_r (–)			σ (S/m)		
Material	Measured	Min	Max	Measured	Min	Max
Muscle phantom	58.69	46	70	0.95	0.6	1.1
Target phantom	52.16	46	70	1.30	0.6	1.8
				h **(W/(m^2 · °C))**		
Region				Ideal	Min	Max
Top neck (h_{tn})				30	10	80
Bottom neck (h_{bn})				20	10	80
Water bolus (h_{wb})				55	10	80

reconstruct the temperature in all the available points, using a set of purposely mutated replicas of the system; this set of reconstruction functions is generated in COMSOL Multiphysics by solving the transient version of the heat equation.

In this scenario, the simulated temperature distribution is more affected by uncertainties characterizing the dielectric properties of the phantoms used in the prototype (i.e., the muscle-mimicking phantom forming the neck and the tumor target), and by the heat transfer coefficients introduced to describe the heat exchange between the system and the external environment. The involved parameters and the considered variation ranges are reported in Table 6.7 and are changed according to a Sobol sequence to build the library of multiphysics simulations (as detailed in Sec. 6.2). It is noteworthy that the presence of PMMA walls of non-negligible thickness around the neck phantom makes it difficult to estimate the heat transfer coefficients. Given this high level of uncertainty, most of the heat transfer coefficients were included in the proposed reconstruction procedure and were allowed to vary within wide ranges ($10 \div 80$ W/(m^2 °C)), as reported in Table 6.7) for the creation of the set of mutated replicas of the system.

Concerning the application of the proposed method to the experimental testbed, the reconstruction functions in Eq. (6.1) are temperature maps $\mathcal{F}(\boldsymbol{r}, t; \boldsymbol{s}_b)$, $b \in \{1, \ldots, B\}$, provided by COMSOL Multiphysics using combinations of parameters $\boldsymbol{s}_b$ varied according to a Sobol sequence within the ranges reported in Table 6.7. To mitigate errors in the positioning of the array system along the z-axis, the reconstruction functions $\mathcal{F}_k(\boldsymbol{r} + \Delta z_k \hat{z}, t; \boldsymbol{s}_b)$, where Δz is a vector of shifts, are included in Eq. (2). In the described application of the proposed method, we considered $B = 200$ Sobol sequence variations $\boldsymbol{s}_b$, $b \in \{1, \ldots, B\}$, and a vector of shifts $\Delta z = (-5, -2{,}0{,}2{,}5)$ mm, which resulted in having 1000 reconstruction functions. Using the L acquisition points along one of the arrays to retrieve the weights with the CLS method (Eqs. (6.2) and (6.3)), the other temperature values

provided by the FBG sensors are used as benchmarks to establish the accuracy of the reconstruction.

The goal of the proposed procedure is to use the experimental temperature values provided by the FBG sensors at the time t in a set of points $\boldsymbol{q}_\ell$, $\ell = 1, \ldots, L$, along *one of the arrays* (see Table 6.6) to obtain the temperature distribution in the *entire phantom* and then use all the experimentally available points to validate the reconstruction process.

The difference between the reconstructed map and the experimental measurements is analyzed in terms of the normalized goodness function $g(\chi)$ defined in Eq. (6.5). Figure 6.11 shows $g(\chi)$ evaluated when the temperature measurements along the Arrays from 1 to 5 are used individually to perform the reconstruction at the end time $t = t_{off} = 160$ min (solid red-dot curves); Fig. 6.11 also reports the normalized goodness function $g(\chi)$ obtained by computing the error between the experiment and the ideal simulation model (dash-diamond green line), obtained in COMSOL using the measured dielectric properties and the heat transfer coefficients derived by directly fitting the model to all the available data (see Table 6.7). The gray shaded region in Fig. 6.11 corresponds to the envelope of the functions $g(\chi)$ obtained by considering the difference between each reconstruction function and the experimental data. To estimate the effectiveness of the reconstruction (solid red-dot lines in Fig. 6.11) it is necessary to consider the similarity with the green curve, which provides the best possible representation of the experiment with the implemented model. As can be observed, the curves corresponding to the reconstruction (solid red-dot lines in Fig. 6.11) closely approximate the curve of the ideal model for almost all the arrays used for the reconstruction, and the error remains lower than what would occur on average by not applying the proposed method (dashed black line in Fig. 6.11).

Figure 6.12 reports the reconstructed temperature profiles along all the available arrays, obtained by applying the constrained least squares (CLS) method to the points of a) the Array 2 (Fig. 6.12 placed inside the tumor target, b) the Array 4 (Fig. 6.12, and c) the Array 5 (Fig. 6.12, at the final time $t = t_{off} = 160$ min. Figs. 6.12a-c also show the available experimental points provided by the FBGs sensors and the temperature profiles corresponding to the ideal simulation model (dash-dotted green curve). A good agreement is observed in all the reported comparisons, even when the reconstruction is performed using the points of the Array 5 (Fig. 6.12c) inserted into the trachea. Referring to the results shown in Fig. 6.12a, the Array 2 exhibits the largest gradient, but its error is similar to that of the other arrays, such as the Array 4, which experiences a milder temperature distribution. Furthermore, the error between the experimental and simulated temperatures does not consistently have the same sign, even when similar gradients are present. Therefore, there is no clear evidence to suggest that measurement errors are directly related to the gradient and, by extension, to the presence of capillaries. As a consequence, in the presented study the capillary's dimensions and material

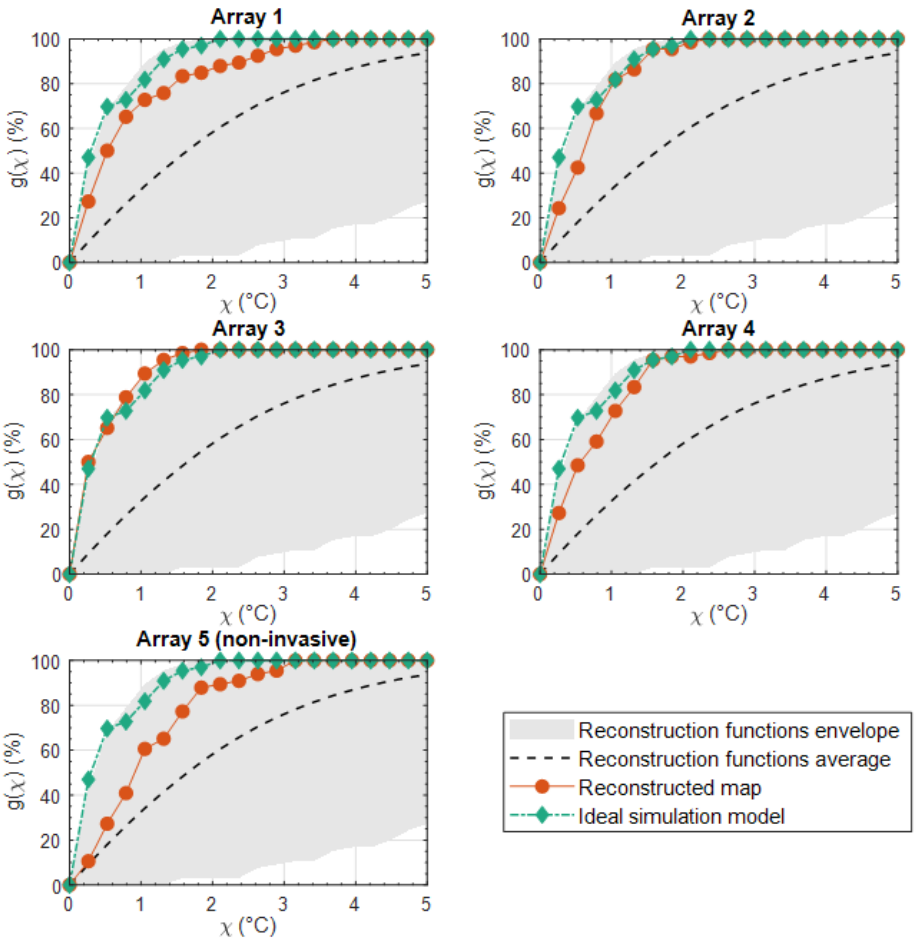

Figure 6.11: Reconstruction error indicating the fraction of points with an error below the threshold χ. The temperature map is reconstructed using the experimental data along each array (from 1 to 5, as indicated in the title of the different frames) and the normalized goodness function $g(\chi)$, Eq. (6.5), is evaluated in all the available points, at the end time $t = t_{off} = 160$ min (solid red-dot lines). The function $g(\chi)$ obtained by computing the error between the experiment and the ideal simulation model (dash-diamond green line) is reported for comparison, together with the envelope (gray shaded region) and the average (dashed black line) of the functions $g(\chi)$ evaluated by considering the difference between each reconstruction function and the experimental data (note that $g(\chi) = 1$, $\forall\chi$, denotes perfect reconstruction).

do not seem to have a significant impact on the observed discrepancies.

To analyze the quality of the reconstruction at different times, the following

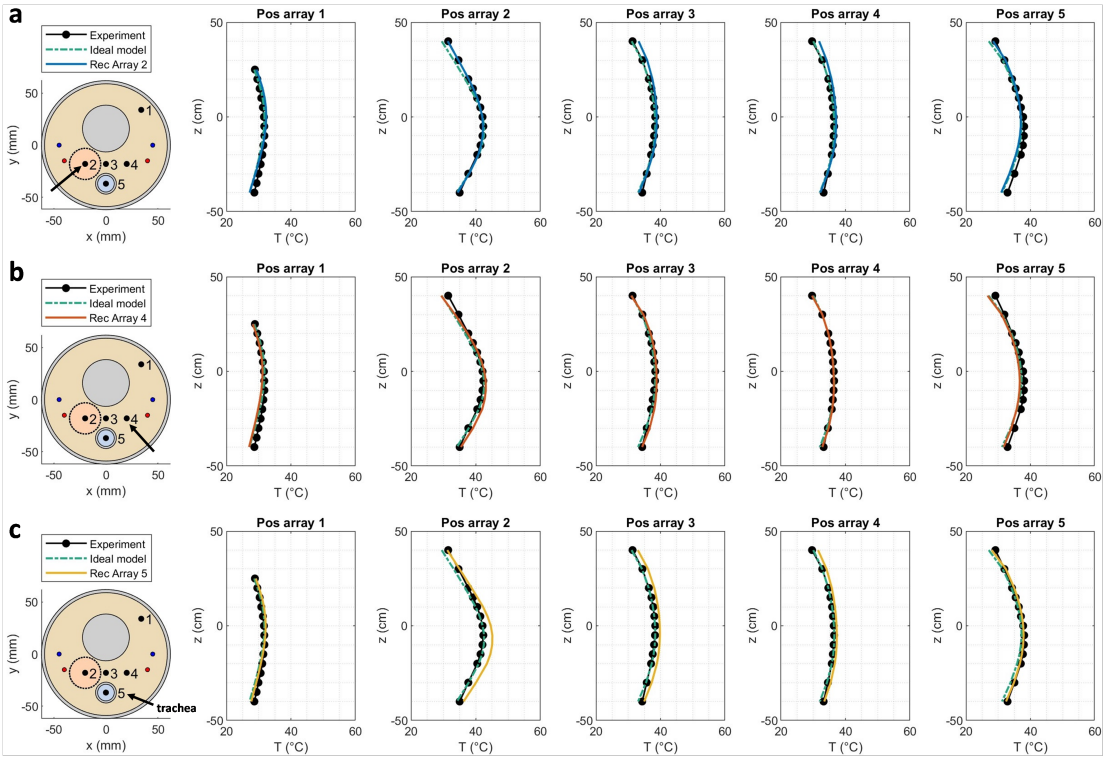

Figure 6.12: Reconstructed temperature profiles versus experimental values and ideal profiles. Temperature profiles at $t = t_{off} = 160$ min along all the available arrays at the different positions ("Pos") on the xy-plane, reconstructed by applying the CLS method using the experimental points along (a) the Array 2 , (b) the Array 4 and (c) the Array 5, where the last one is inserted in the phantom's region mimicking the human trachea. For direct comparison, the measured temperatures are also reported (black-dot line), together with the temperature profiles corresponding to the ideal simulation model (dash-dotted green line), which is the model obtained in COMSOL by directly measuring the dielectric properties of the materials used in the experiment and using heat transfer coefficients derived by fitting the model to all the available experimental data.

error metric (ℓ^2-norm) was computed:

$$h(t) = \frac{1}{\sqrt{M}} \left(\sum_{m=1}^{M} \left| \hat{T}(\boldsymbol{r}_m, t) - \tilde{T}(\boldsymbol{r}_m, t) \right|^2 \right)^{1/2}, \tag{6.6}$$

where $\hat{T}$ is the reconstructed map, while $\tilde{T}(\boldsymbol{r}_m, t)$, $m = 1, \ldots, M$, indicates all the available experimental points ($M = 66$). The difference reported in Eq. (6.6) is the estimator ΔT evaluated at each spatial point and at each time. Expressions similar to Eq. (6.6) are obtained by replacing $\tilde{T}(\boldsymbol{r}_m, t)$ with the temperature map corresponding to the ideal simulation model and the reconstruction functions. The results are reported in Fig. 6.13. As can be observed, the errors corresponding to the

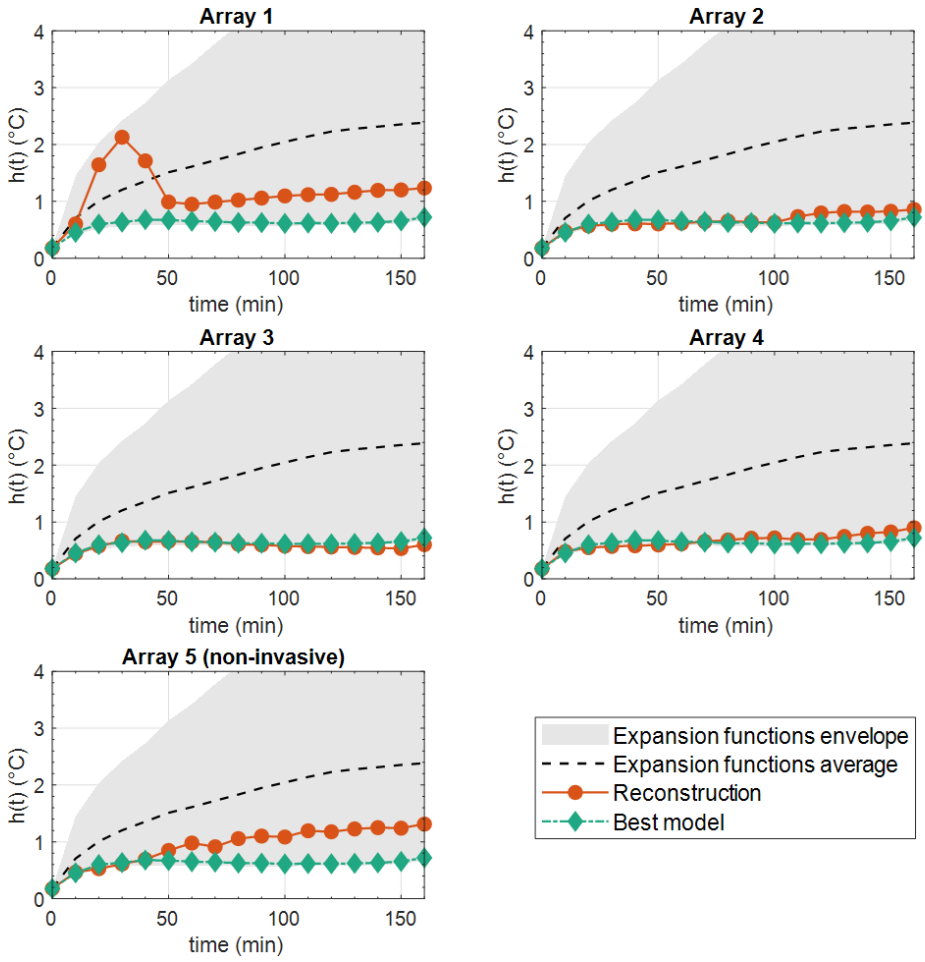

Figure 6.13: ℓ^2-norm error $h(t)$ evaluated in all the available points as a function of time. The red-dot lines report the ℓ^2-norm error $h(t)$, Eq. (6.6), computed by comparing the reconstructed temperature values and the experimental measurements in all the available points when the reconstruction is performed using the information along the Arrays from 1 to 5, at 17 time samples between the initial and final time of the heating session. The error is also reported for the ideal simulation model and the reconstruction functions (envelope and average).

application of the reconstruction method tend to approximate the errors affecting the ideal model in almost all cases; this demonstrates how the proposed technique is able to provide satisfactory results in real time. The ripple in correspondence of the Array 1 (which is the farthest from the tumor target) is only observed in the initial stage of the heating phase, and the curve tends to stabilize over time, approaching the ideal curve as expected.

Table 6.8: Temperature reconstruction accuracy over all probes and the complete heating session duration

	ΔT (°C)				
	Array 1	Array 2	Array 3	Array 4	Array 5
Median	0.5	0.4	0.4	0.4	0.6
IQR	0.9	0.6	0.5	0.6	0.9

The accuracy of the predicted temperature is here estimated using the absolute difference (ΔT) between measured and reconstructed temperature values over all the available probes and during the complete heating session (we considered 17 time samples). Table 6.8 show the median and the IQR of ΔT evaluated when each array is individually considered to perform the reconstruction. As can be observed, the error achieved is included in the range $0.4 \div 0.6$ °C, resulting reasonably higher for the array farthest from the target region (Array 1) and for the one inserted in the trachea (Array 5).

6.9 Conclusion

One of the major drawbacks to widespread application of microwave hyperthermia in cancer therapy is the lack of a temperature monitoring system able to reliably trace (and even predict) the temperature in the whole ROI throughout the entire duration of the treatment (60-90 min). Invasive thermal probes provide accurate thermometry (about 0.2°C accuracy [129]), but the information is strictly limited to a scarce number of locations [38], and their use must be reduced to the bare minimum to avoid severe treatment-related morbidities [130]. Simulations, while able to provide the needed spatial information, are not reliable: the main hurdle is the large uncertainty characterizing thermal tissue properties, which vary among patients and under thermal stress [27]. Other solutions to the temperature monitoring problem are still at the research stage and often involve expensive and complex equipment, as an MRI scanner [102, 15].

In this chapter, we have proposed a method which allows to obtain a real-time 3D temperature map in the patient's region of interest from few, noisy, measurement points, which can also be intraluminal (non-invasive), thus circumventing the issues of the other techniques. The reliable reconstructed temperature map is intended to be used by a treatment-supervising physician, or as feedback for automatic real-time-adaptive treatment approaches [69, 75], to increase the efficacy and safety of the procedure. The proposed method has been verified in a specific context, which is that of microwave hyperthermia, but the applicability of the proposed technique

extends to heat therapies in general, where the ability to monitor temperature accurately becomes increasingly crucial as the involved temperatures rise, along with the associated risk of irreversible tissue damage (e.g., in ablation treatments [104, 131]). Moreover, we focused our demonstration on the H&N region, a challenging site due to tissue heterogeneity and the presence of thermosensitive regions like the spinal cord; however, the presented technique could be generally applied to all other regions where thermal therapies are used [1, 14].

To demonstrate the validity of the proposed method, we have considered two different scenarios reproducing an HT treatment in the H&N region. In the first scenario, we tested our procedure using fully anthropomorphic phantoms; here, we reconstructed the temperature map corresponding to a combination of thermal parameters of the major tissues involved (*target map*) starting from few noisy points along a fixed direction. To perform an exhaustive analysis, the method was applied to about two thousand target maps in a wide range of cases (Figures 6.7a-c). The T50 and T90 treatment quality parameters exhibit a median accuracy of 0.2°C (IQR 0.4°C) over the large set of cases considered (Table 6.5), strongly outperforming the performance achieved with simulations based on literature values (SoA), i.e., 4°C median accuracy. The achieved accuracies align with the estimates considered promising in the relevant literature [27], suggesting that the proposed method is a particularly good candidate for accurate 3D temperature dosimetry in HTP. The method proved to be significantly robust against unexpected variations in parameters not included in the reconstruction process, as well as against geometric displacements (Figure 6.7d). The T50 and T90 parameters can be predicted with a median accuracy of 0.2°C, even introducing variations of 10%-20% in the dielectric parameters, and displacements of the phantom in the range ±5 mm (Table 6.5).

In the second scenario, the possibility to apply the proposed technique in a non-invasive way, i.e., using RF-compatible intraluminal thermometry, has been addressed; here, the procedure was experimentally tested using a mock-up reproducing a HT treatment in the neck region. Temperature monitoring was performed using arrays of FBGs sensors. The median temperature accuracy reached when each array is individually considered as known when performing the reconstruction for all probes (along all the arrays) and for the complete treatment duration is in the range $0.4 \div 0.6$ °C (Table 6.8), demonstrating acceptable values even when the array used for the reconstruction is inserted into the phantom's structure mimicking the trachea. Being obtained in a real environment, these values represent an upper bound to the accuracies estimated in this article, which could likely be further enhanced by increasing control over the implemented setup.

In the proposed technique, mutated replicas of the simulated system are used for the creation of a framework where these replicas coexist and interact with scarce measurements, to provide an estimate of the true state with reduced uncertainty. In this perspective, the proposed method could be applied in principle also when the measured data is only indirectly related to the physical quantities of interest,

by modeling the target system along with the measurement process. This would allow the proposed method to be used not only with fiber-optic temperature probes, but also with a set of scarce and indirect measurements provided by non-invasive methods such as the electrical impedance tomography [105, 106, 107, 108].

Possible limitations of the proposed technique are related to the level of accuracy of the model used to describe the physics of the system, which is the Pennes bioheat equation [35] in the presented work. The method could be applied in principle to more complex models [132, 133], where high-performance computing techniques will likely be required to handle the higher computational burden. Further studies are also planned to test the robustness of the proposed method in the presence of spatial inhomogeneities of crucial tissue parameters such as perfusion.

The validation of the method using phantoms presented in this article provides the necessary initial testing of the proposed technique. The proposed method proves to be an effective solution to address the problem of temperature monitoring: it strongly outperforms SoA simulations based on literature values; it provides comparable accuracies as the optimization methods currently proposed in the literature [27] but in real-time; it is low-cost and does not present the issues of MR thermometry; it is low-cost and has shown to be effective with non-invasive measurements.

In light of the achieved results, we believe that this work and future tests with clinical data could pave the way for the implementation of an effective means to plan and control HT treatments, enhancing the application of HT in cancer therapies.

Chapter 7

SAR-based Optimization via Local Power Synthesis Algorithm

This chapter reports the published article [134].

As already mentioned, one of the preliminary steps in microwave hyperthermia treatment planning is the optimization of antenna feeding coefficients, which aims to maximize the specific absorption rate (SAR) within the tumor while minimizing unwanted heating in surrounding healthy tissues. Conventionally, this optimization relies on meta-heuristic global algorithms such as the Particle Swarm Optimization (PSO). In this study, we consider a deterministic alternative to PSO in microwave hyperthermia SAR-based optimization which is based on the Alternating Projections Algorithm (APA). This method iteratively projects the electric field distribution onto a set of constraints to shape the power deposition within a predefined mask, enforcing SAR focusing within the tumor while actively suppressing deposition in healthy tissues. To address the challenge of selecting appropriate power levels, we introduce an adaptive power threshold search mechanism using a properly defined quality parameter, which quantifies the excess of deposited power in healthy tissues. The proposed method is validated on both a simplified numerical testbed and a realistic anatomical phantom. Results demonstrate that the proposed method achieves heating quality comparable to PSO in terms of tumor targeting, while significantly improving hotspot suppression.

7.1 Introduction

As detailed in the previous chapters, Hyperthermia Treatment Planning (HTP) is a key step in microwave hyperthermia (HT) preparation [67]. HTP uses patient-specific anatomical models and detailed EM simulations to optimize the feeding amplitude and phase of each antenna in the array applicator [38], with the aim of selectively focusing energy within the tumor while limiting exposure in healthy

tissues.

Various optimization techniques have been developed for HTP [135, 136, 137, 37, 138, 69]; among them, specific absorption rate (SAR)-based methods [69, 70, 71, 63, 89] remain the most practical and widely adopted in clinical settings, typically implemented using global meta-heuristic algorithms such as the particle swarm optimization (PSO) algorithm [81]. While global meta-heuristic algorithms provide robust solutions, they are computationally demanding and may require many iterations to converge. This high computational cost can hinder real-time adjustments or re-optimizations, even though the initial optimization is usually performed during the pre-treatment planning phase.

In recent years, an alternative class of algorithms—local power synthesis techniques—has been explored for SAR-based optimization [139, 140]. Inspired by far-field antenna array synthesis [141, 142], these methods attempt to directly shape the field/SAR distribution by constraining the electric field within a spatially defined "power mask".

Related deterministic strategies for shaping field/SAR intensity distributions in inhomogeneous scenarios have also been proposed across biomedical electromagnetics and antenna synthesis literature, including the multi-frequency constrained SAR focusing framework developed for patient-specific hyperthermia to improve control of off-target heating [143] and the auxiliary-model / control-point paradigm that exploits unknown phase shifts between the fields at selected control points [144]. Other complementary contributions originally developed for beamforming and scalar field shaping [145, 146] share with the present work the general idea of enforcing spatial field specifications in complex environments.

In this study, we propose a deterministic SAR-based optimization method based on the Alternating Projections Algorithm (APA). In the formulation adopted here, the field samples are represented in a magnitude–phase space following the framework of [142]. Under this framework, at each sampling point, the masking procedure is applied only to the field magnitude, while the phase is left unconstrained. However, general convergence guarantees are not expected, since the APA update alternates amplitude-only masking in the field domain with an excitation update through a pseudo-inverse radiation operator, and this mapping does not, in general, preserve convexity of the involved sets [142]. Despite this, stable behavior was observed in the investigated hyperthermia scenarios. This approach has demonstrated to provide precise shaping of the SAR pattern, facilitating tumor targeting while actively suppressing energy in healthy tissues.

To overcome the practical challenge of selecting appropriate power thresholds, we introduce an adaptive threshold selection mechanism guided by a SAR-based hotspot suppression indicator, denoted as V^H, which quantifies the percentage of healthy tissue volume exceeding a relative SAR level.

The proposed APA-based method is validated through simulations in both a simplified numerical testbed and a realistic anatomical model of the H&N region.

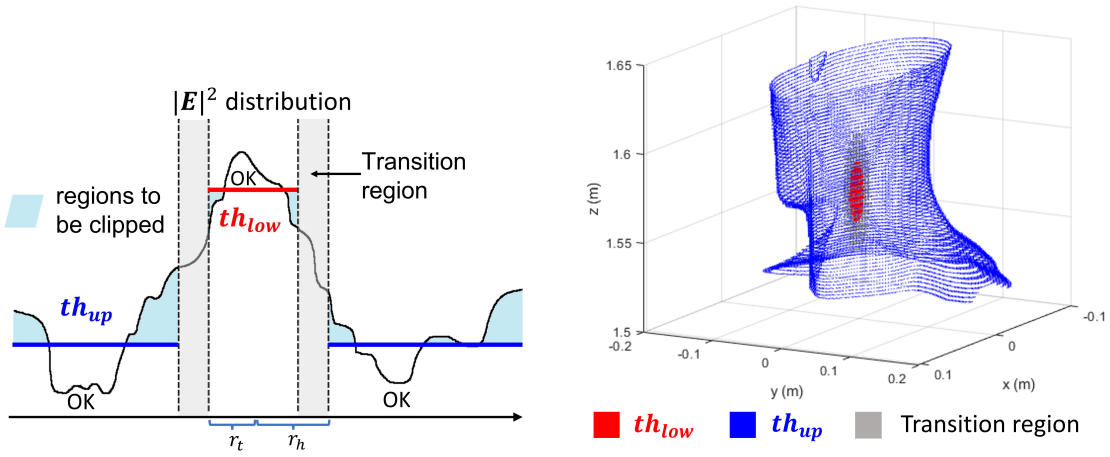

(a) (b)

Figure 7.1: (**a**) Clipping of a generic 1D function using a two-level mask, where values are confined between two thresholds th_{low} and th_{up} through smooth transitions. The distances r_t and r_h are the maximum radial distances from the tumor center that define, respectively, the boundary of the tumor region and the outer edge of the transition (gray) region. (**b**) APA mask defined on a 3D phantom: red points correspond to the tumor region where the th_{low} is applied; gray points denote the transition region where no constraints are imposed; blue points indicate the healthy region (outside the transition zone) where the th_{up} is enforced. For visualization clarity, only the boundary of the healthy region is shown in blue.

Its performance is compared to that of the PSO-based SAR optimization in terms of tumor coverage, hotspot suppression, and computational efficiency.

7.2 Optimization method

The primary objective of SAR-based optimization is to maximize power deposition within the tumor region while minimizing the risk of overheating in the surrounding healthy tissues. In deep hyperthermia, the electromagnetic field must inevitably propagate through layers of healthy tissue before reaching the tumor—this is precisely what makes selective heating challenging. The optimization procedure adjusts the feeding coefficients of the antenna array to exploit constructive interference in the tumor and destructive interference elsewhere, thereby focusing the absorbed power where it is needed.

The total electric field can be written as the superposition of the individual electric fields generated by each antenna element when excited individually, weighted

by their corresponding complex excitation coefficients. Accordingly:

$$\boldsymbol{E}(\boldsymbol{r}) = \sum_{n=1}^{N} b_n \, \boldsymbol{e}_n(\boldsymbol{r}), \tag{7.1}$$

where $\boldsymbol{e}_n(\boldsymbol{r})$ denotes the electric field at point $\boldsymbol{r}$ generated by the nth antenna with unit excitation (all others turned off), and b_n is the complex excitation coefficient (amplitude and phase) of the nth antenna in an N-element array. In the present work, we considered an array of patch antennas [17], linearly polarized along the vertical (z) axis, as common in deep hyperthermia systems [18].

To optimize the excitation coefficients $[b]$, we apply the Alternating Projections Algorithm (APA). We discretize the electric fields defined in Equation (7.1) over a set of M sampling points $\boldsymbol{r}_m$, corresponding to the mesh points in the simulated volume of interest. The matrix:

$$[E_N] = [[\boldsymbol{e}_1], [\boldsymbol{e}_2], \ldots, [\boldsymbol{e}_N]], \tag{7.2}$$

collects the simulated electric fields generated by each unit-excited antenna. The field distributions are calculated only once at the beginning of the optimization. These fields are obtained from full-wave simulations in a heterogeneous anatomical model, where each tissue is assigned its own dielectric properties. Each column $[\boldsymbol{e}_n]$, $n = 1, \ldots, N$, contains the values of the electric field vector $\boldsymbol{e}_n(\boldsymbol{r})$ estimated in the set of spatial points $\boldsymbol{r}_m$, $m = 1, \ldots, M$, arranged by stacking the three Cartesian components as:

$$[\boldsymbol{e}_n] = \begin{bmatrix} [e_{n,x}] \\ [e_{n,y}] \\ [e_{n,z}] \end{bmatrix}, \tag{7.3}$$

with:

$$[e_{n,k}] = \begin{bmatrix} e_{n,k}(\boldsymbol{r}_1) \\ \vdots \\ e_{n,k}(\boldsymbol{r}_\mathrm{M}) \end{bmatrix}, \quad k = x, y, z. \tag{7.4}$$

To reproduce a power pattern focused on the tumor mass, a starting target field $[E_t]$ (e.g., a Gaussian field centered on the tumor region) is considered and projected onto the column space of the matrix $[E_N]$ to find a reconstructed field $[E_t^{rec}]$. Before generating the initial target field $[E_t]$, we assess the polarization of the unit-excited fields $\boldsymbol{e}_n$ by examining the dominant component in the matrix $[E_N]$. In our setup, the z-component entries are about one order of magnitude larger than the x- and y-components, reflecting the intrinsic polarization of the chosen antenna type. The Gaussian target $[E_t]$ is then generated using this dominant component, ensuring that its polarization matches that of $\boldsymbol{e}_n$. The amplitude and width of this starting

Gaussian target field were properly fixed to fit an optimized power distribution in the region of interest. Since the first reconstructed field was considerably different from the target field, an iterative procedure was implemented to adapt its profile to the desired focused pattern.

First, following common HTP procedures, the tumor ($\mathcal{T}$) and healthy ($\mathcal{H}$) tissue regions are identified; this step is performed in clinical practice using patient-specific anatomical segmentations obtained from CT or MRI scans. Then, at each step of this procedure, the squared norm of the reconstructed field is compared to a power mask with two threshold levels (see for reference Fig. 7.1 and Sec. 7.3.2 for details). To ensure a sufficient field focusing on the target, the first level th_{low} is enforced within the tumor tissue $\mathcal{T}$, defined as a region with maximum radial extent r_t. To avoid hotspots, the second level th_{up} is applied in the healthy tissue $\mathcal{H}$ located outside r_h, where r_h denotes the outer edge of the transition region measured radially from the tumor centroid. The transition region is thus a shell region defined between r_t and r_h where no constraints are imposed, allowing for a more gradual tapering of the field (see Fig. 7.1b).

When the squared modulus of the reconstructed field is below th_{low} for $\boldsymbol{r}_m \in \mathcal{T}$, or exceeds th_{up} for $\boldsymbol{r}_m \in \mathcal{H}$, its value is adjusted (clipped) to the corresponding mask threshold, and the new field is projected again onto the columns of $[E_N]$, providing a vector of complex antenna feedings b_n, $n = 1, \ldots, N$, which is normalized at each step to fix the total input power to 1 W. This normalization includes the parameters P_0, the total power fed to the array, R_0, the reference input resistance, and $\| [b] \|^2$, the squared norm of the complex excitation vector.

The detailed steps of the APA optimization procedure are outlined in Algorithm 1.

To monitor convergence and determine the stopping point of the iterative process, we adopt a well-established criterion from the literature [69], aimed at minimizing the Hotspot-to-Target SAR Quotient (HTQ), defined as:

$$\mathrm{HTQ} = \frac{\langle \mathrm{SAR}_{\,\mathrm{V1}} \rangle}{\langle \mathrm{SAR}_{\,\mathrm{TARGET}} \rangle}, \tag{7.5}$$

where $\langle \mathrm{SAR}_{\,\mathrm{V1}} \rangle$ is the average SAR in V1, being V1 the 1% of the healthy volume with the highest SAR [66, 77], and $\langle \mathrm{SAR}_{\,\mathrm{TARGET}} \rangle$ is the average SAR in the target region. It should be noted that, for the evaluation of the HTQ metric, the healthy tissue region is defined to include both the outer healthy region $\mathcal{H}$ and the transition region (see Fig. 7.1), i.e., all tissues outside the tumor, in accordance with the standard definition [66].

The developed APA algorithm includes a dynamic stopping criterion based on the evolution of the HTQ parameter and the number of field points exceeding the power mask. Specifically, the optimization is stopped when the HTQ reaches a plateau, or begins to increase, and when the number of out-of-mask points starts increasing persistently indicating that no further meaningful improvement can be

Algorithm 1 APA Optimization Algorithm

procedure APA Optimization
  Inputs: Electric field matrix $[E_N]$, Gaussian initial guess $[E_t]$, tumor region $\mathcal{T}$, healthy region $\mathcal{H}$, th_{low}, th_{up}, input power P_0, reference input resistance R_0
  Output: Optimized antenna excitation vector $\left[\tilde{b}\right]$

  Initialization:
  Compute pseudo-inverse: $[E_N]^{\dagger} = \text{pinv}([E_N])$

  $[b] = [E_N]^{\dagger} \cdot [E_t]$
  $C = P_0/(\|[b]\|^2/(2R_0))$
  $\left[\tilde{b}\right] = \sqrt{C}\,[b]$
  $[E_t^{rec}] = [E_N] \cdot \left[\tilde{b}\right]$
  while stopping criterion not met **do**
    for each voxel $r_m \in \mathcal{T}$ **do**
      if $|\,[E_t^{rec}]_m\,|^2 < th_{low}$ **then**
        $[E_t^{rec}]_m = \sqrt{th_{low}} \cdot \dfrac{[E_t^{rec}]_m}{|\,[E_t^{rec}]_m\,|}$
      end if
    end for
    for each voxel $r_m \in \mathcal{H}$ **do**
      if $|\,[E_t^{rec}]_m\,|^2 > th_{up}$ **then**
        $[E_t^{rec}]_m = \sqrt{th_{up}} \cdot \dfrac{[E_t^{rec}]_m}{|\,[E_t^{rec}]_m\,|}$
      end if
    end for
    $[b] = [E_N]^{\dagger} \cdot [E_t^{rec}]$
    $C = P_0/(\|[b]\|^2/(2R_0))$
    $\left[\tilde{b}\right] = \sqrt{C}\,[b]$
    $[E_t^{rec}] = [E_N] \cdot \left[\tilde{b}\right]$
  end while
end procedure

achieved. This safeguards against unnecessary iterations and ensures timely convergence within a maximum of 4000 iterations.

7.3 Results

7.3.1 Reference testbed

To validate the APA-based SAR optimization, a simplified numerical phantom of the human neck and an HT applicator were modeled in COMSOL Multiphysics® [48]. The setup, illustrated in Fig. 7.2a, consists of a cylindrical phantom mimicking the human neck, surrounded by a circular array of $N = 8$ patch antennas, immersed in water to emulate the clinically used waterbolus [18]. This device is a plastic bag filled with circulating demineralized water to enhance electromagnetic coupling into tissues, preventing superficial heating, and improve patient comfort [18].

The neck phantom is composed of concentric tissue layers, each assigned electromagnetic properties representative of typical H&N anatomy, following the widely accepted dielectric model for biological tissues [26, 24, 25]. As illustrated in Fig. 7.2b, the tissues include skin, fat, muscle, bone, spinal cord, and a tumor region. The tumor is modeled as a sphere with radius $r_t = 6$ mm and is embedded within the phantom at coordinates $(-18, -18, -15)$ mm relative to the center of the cylindrical phantom. For the tumor tissue, dielectric properties have been tailored for realistic H&N HTP according to [27] ($\varepsilon_r = 59$ and $\sigma = 0.89$ S/m). Moreover, to mimic the influence of the shoulders and minimize air–water boundary effects, the phantom is positioned on a 4-cm thick muscle layer [17]. For APA optimization, the outer radius of the transition region was assumed to be almost 1 cm greater than the extent r_t of the tumor, i.e., $r_h = 18$ mm [147].

The array of patch antennas was designed and optimized to operate efficiently

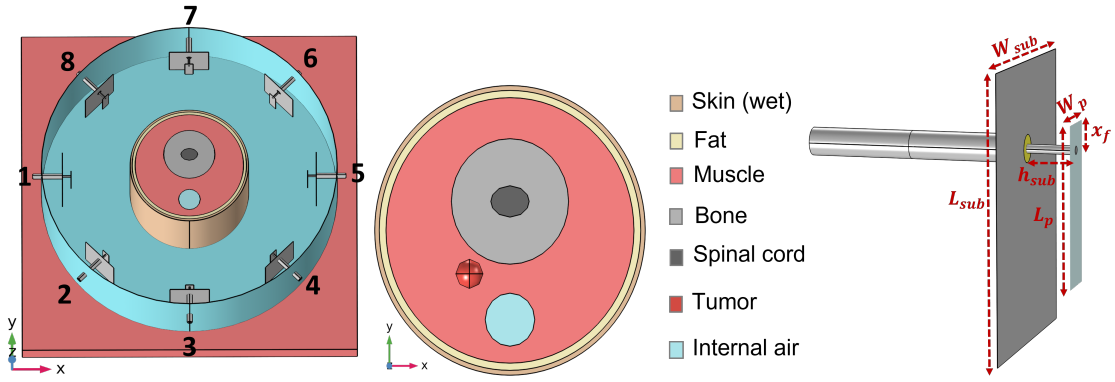

(a) (b) (c)

Figure 7.2: (**a**) Circular array of patch antennas surrounding the simple neck model immersed in the waterbolus. (**b**) Middle top view ($z = 0$ plane) of the simplified neck model with all the considered tissues. (**c**) Employed patch antenna and optimized dimensions.

Algorithm 2 Adaptive Threshold Search for APA Optimization

Inputs: Electric field matrix $[E_N]$, input power P_0, reference input resistance R_0, tumor region $\mathcal{T}$ with radius r_t, healthy region $\mathcal{H}$ with radius r_h
Fixed Gaussian peak amplitude A_0 at tumor center (x_t, y_t, z_t) with the maximum achievable intensity
Candidate set $\{th_{up}^{(i)}\}$ to control hotspot suppression
Outputs: Optimal excitation vector $\left[\tilde{b}\right]^{\star}$ and selected threshold $th_{up}^{\star}$
Determine the dominant polarization component ν of $[E_N]$
for each $th_{up}^{(i)}$ in candidate set **do**
    Compute standard deviation $\sigma_0 = r_h \left(2 \log \left(A_0 / th_{up}^{(i)}\right)\right)^{-1/2}$
    Compute $th_{low}^{(i)} = A_0 \cdot \exp\left(-r_t^2/(2\sigma_0^2)\right)$
    Construct Gaussian field $[E_t]$ with parameters A_0 and σ_0 and polarization ν
    Run APA Optimization (Algorithm 1) with $\left([E_t], th_{low}^{(i)}, th_{up}^{(i)}\right)$
    Compute metrics $V_{10\%}^{H}$ and $V_{50\%}^{H}$
    Store results in $\mathcal{Q}(th_{up}^{(i)}, V_{10\%}^{H}, V_{50\%}^{H})$
end for
Identify $th_{up}^{\star}$ via Pareto trade-off between $V_{10\%}^{H}$ and $V_{50\%}^{H}$
Return corresponding excitation vector $\left[\tilde{b}\right]^{\star}$

at the frequency $f = 434$ MHz, as commonly used in clinical hyperthermia systems [17]. With reference to Fig. 7.2c, the optimized antenna geometry includes a ground plane of dimensions $L_{sub} = 50$ mm, $W_{sub} = 40$ mm. The patch is placed at a distance $h_{sub} = 8.8$ mm from the ground and has dimensions $L_p = 28.8$ mm and $W_p = 8.4$ mm. The antenna is fed by a coaxial probe located at an offset distance $x_f = 4.8$ mm from the patch edge.

In the implemented model, the electromagnetic and thermal distributions are computed using the finite element method (FEM) [48]. A tetrahedral mesh is employed, with maximum element sizes of 5 mm in the neck tissues and 1 mm in the antenna applicator, as chosen to find a suitable trade-off between computational cost and solution accuracy [14].

7.3.2 Power levels search

The effectiveness of the APA algorithm in maximizing power deposition in the tumor region while suppressing unwanted hotspots in healthy tissues depends critically on the proper selection of the power mask thresholds. As illustrated in Section 7.2, the first threshold th_{low} is applied in the tumor region $\mathcal{T}$ to ensure sufficient field focusing, while the second threshold th_{up} is defined in the healthy tissues $\mathcal{H}$ to suppress the formation of hotspots. A transition region between these levels

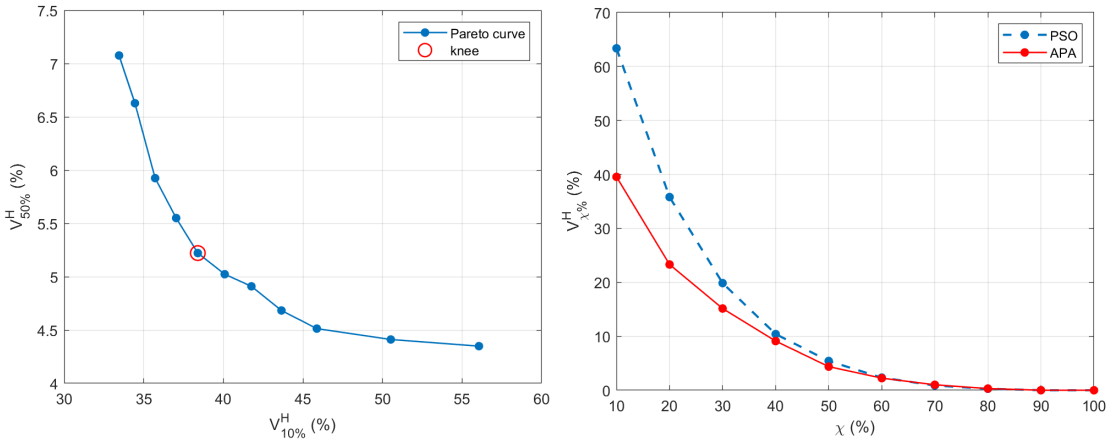

(a) (b)

Figure 7.3: (**a**) Pareto front generated during the APA threshold selection process, showing the trade-off between SAR confinement ($V^H_{10\%}$) and hotspot suppression ($V^H_{50\%}$). The knee point (highlighted in red) indicates the optimal point, corresponding to $(th_{low},\ th_{up}) = (9.08,\ 4.2) \times 10^3$ V^2/m^2. (**b**) Comparison of the $V^H_{\chi\%}$ performance across increasing $\chi\%$ for the APA (using the thresholds corresponding to the knee point) and PSO-based SAR optimization.

allows smooth clipping, avoiding abrupt constraint changes in the field pattern (see Fig. 7.1a).

To identify suitable values for these thresholds for the simplified testbed described in Sec. 7.3.1, we introduce a metric denoted as $V^H_{\chi\%}$, which measures the percentage of healthy tissue volume experiencing SAR values above $\chi\%$ of the maximum SAR within the tumor. The $V^H_{\chi\%}$ metric, computed for different χ values, provides a more detailed understanding of SAR distribution than scalar performance metrics such as the HTQ. Two values of this metric are primarily used: $V^H_{10\%}$ to assess overall SAR spillover into healthy tissues, and $V^H_{50\%}$ to highlight the presence of high-intensity hotspots.

The adaptive power mask search starts with generating a Gaussian field initial guess as detailed in the Algorithm 2. A fixed peak amplitude $A_0 = 10^4$ V^2/m^2 is imposed at the tumor center (x_t, y_t, z_t), ensuring a predefined maximum intensity at the focal point. An upper bound to this quantity may be obtained by evaluating the values of squared modulus of the electric field that can be reached inside the tumor region by each field $\boldsymbol{e}_n$ in (7.1), combining these values assuming complete constructive interference and taking into account the bound on the total input power (lines 7 and 8, and 22 and 23 of Algorithm 1).

For each candidate upper threshold $th^{(i)}_{up}$, which controls hotspot suppression in the healthy tissues, the standard deviation σ_0 of the Gaussian distribution is computed so that the field intensity at the end of the transition region (distance r_h from the tumor center) corresponds to $th^{(i)}_{up}$, i.e., $\sigma_0 = r_h \left(2 \log \left(A_0 / th^{(i)}_{up}\right)\right)^{-1/2}$.

The corresponding threshold $th_{low}^{(i)}$, applied within the tumor region of radius r_t, is then derived from the same Gaussian distribution as $th_{low}^{(i)} = A_0 \cdot \exp\left(-r_t^2/(2\sigma_0^2)\right)$.

Once defined the mask parameters ($th_{low}^{(i)}$, $th_{up}^{(i)}$), the APA optimization (Algorithm 1) is performed, and the resulting SAR distribution is assessed using the $V_{10\%}^H$ and $V_{50\%}^H$ metrics. These two metrics capture, respectively, the volume of healthy tissue exposed to moderate and high levels of SAR relative to the tumor maximum.

A natural trade-off emerges: decreasing th_{up} suppresses hotspots but may also reduce tumor coverage, while increasing it enhances energy delivery to the tumor at the expense of greater off-target exposure. To resolve this, a Pareto front is built by plotting all candidate solutions in the ($V_{10\%}^H$, $V_{50\%}^H$) space, and the final configuration is chosen from the knee of the curve—where both objectives are reasonably balanced (see Fig. 7.3a). The knee point (highlighted in red) indicates the optimal point, which corresponds to (th_{low}, th_{up}) = $(9.08, 4.2) \times 10^3$ V^2/m^2. The corresponding APA excitation vector $\left[\tilde{b}\right]^\star$ is retained as the optimal solution. It has been verified that varying the most critical parameters involved in the adaptive threshold search, such as the amplitude A_0 and the transition region radius r_h, by 10% of the selected values did not change the achieved results. This indicates a fair stability of the implemented optimization process.

7.3.3 SoA comparison

To assess the effectiveness of the proposed APA algorithm, we compare its performance with that of a conventional PSO-based SAR optimization, a widely used state-of-the-art (SoA) metaheuristic method. The PSO algorithm is implemented with the same testbed (detailed in Sec. 7.3.1) with the goal of focusing the SAR within the tumor while reducing energy deposition in the surrounding healthy tissues by minimizing the cost function HTQ defined in (7.5).

Figure 7.3b illustrates the $V_{\chi\%}^H$ curves for the PSO benchmark and APA with selected threshold configuration (corresponding to the knee point of Fig. 7.3a). It is evident that APA shows improved spatial control, with lower SAR leakage into healthy tissues across multiple χ values. This trend confirms that the threshold-guided adaptation in APA yields more consistent control over energy distribution than the global optimization behavior of PSO.

The optimized complex excitation coefficients (amplitudes and phases) for each antenna element resulting from APA and PSO optimization methods are summarized in Table 7.1. These values represent the final configuration used to drive the antenna array for each method.

From a computational standpoint, the PSO algorithm (with a swarm size of 100) required approximately 140 seconds to converge, on a Intel Core i9 workstation with 128 GB RAM. In contrast, a single APA optimization run completed in less than 10 seconds. Including the time required for the adaptive threshold selection procedure (approximately 120 seconds), the overall APA computational time remains comparable to that of PSO. Notably, the APA achieves superior hotspot suppression while maintaining comparable computational performance. Note that the time required to compute the electromagnetic field matrices—which is common to both methods—is approximately 23 minutes and not included in the optimization timings. Table 7.2 summarizes the key properties of the APA and PSO optimizations, including the number of iterations, the total computational time, and the final HTQ values.

Table 7.1: Optimized antenna excitation coefficients (amplitudes and phases) for APA and PSO

n	APA Optimization		PSO Optimization	
	Amplitude (V)	Phase (°)	Amplitude (V)	Phase (°)
1	4.68	45.3	3.591	318.0
2	5.06	29.4	2.270	288.3
3	3.37	33.2	3.053	298.3
4	3.77	76.1	3.568	349.6
5	3.15	124.4	4.686	57.5
6	1.05	120.6	2.680	359.9
7	1.08	128.4	2.912	326.2
8	3.84	92.4	4.719	0.0

Table 7.2: Comparison of the convergence indicators for APA and PSO

	APA Optimization	PSO Optimization
Num. iterations	1001	266
Total time (s)	128	140
HTQ (final)	0.8089	0.7998

Qualitative results from the normalized SAR maps—with respect to the maximum SAR within the tumor region ($\mathcal{T}$)—for a given input power are reported in Fig. 7.4. While both PSO and APA provide good target heating, APA offers a tighter confinement of the high-SAR regions, minimizing off-target exposure. This reflects the benefits of using adaptive power thresholding during optimization. Together, these results indicate that APA not only achieves comparable tumor targeting performance to PSO but also improves safety by suppressing undesired SAR levels in the surrounding healthy tissues.

To obtain the temperature distributions, a thermal simulation was performed in COMSOL Multiphysics by solving the heat transfer study based on Pennes' bioheat equation [35], where the locally computed SAR served as the electromagnetic power deposition source term (see Sec. 2.3). As common in HTP, we considered the steady-state version of the bioheat equation (Equation 2.11), which implies a vanishing time-dependent term ($\partial T/\partial t$) [14].

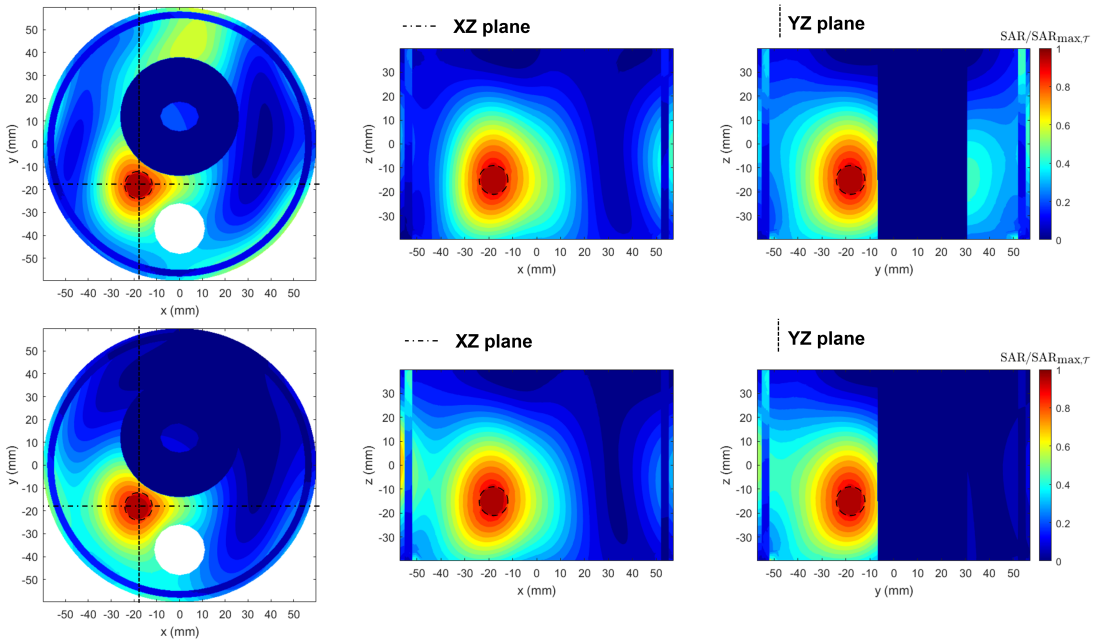

Figure 7.4: Normalized SAR maps comparison between PSO (upper row) and APA (lower row), displayed on the three canonical planes cutting the tumor sphere at its centroid. The black dashed circle indicates the tumor sphere region. The APA thresholds considered are $(th_{low},\, th_{up}) = (9.08, 4.2) \times 10^3$ V^2/m^2. While both methods achieve good tumor coverage, the APA solution results in more confined SAR patterns, reducing hotspots outside the target.

The model incorporated tissue-specific thermal properties and applied convective boundary conditions to mimic heat exchange with the surrounding environment [27, 47]. A convective heat flux boundary condition was applied at the interface between the neck and the waterbolus, using a heat transfer coefficient of $h = 82$ W/(m^2·°C) and an external reference temperature of $T_{\text{ext}} = 20$°C. Additionally, a convective boundary condition was imposed on the internal surface of the trachea, with $h = 50$ W/(m^2·°C) and $T_{\text{ext}} = 30$°C. The initial tissue temperature was uniformly set to $T_{\text{in}} = 37$°C.

The corresponding temperature maps in Fig. 7.5 further illustrate that APA achieves comparable tumor heating to PSO with a lower total input power ($P_0 = 16$ W vs. $P_0 = 26$ W). These power levels were selected to ensure that the target temperature of 42°C was reached within the tumor region. The reduced power requirement in the APA case highlights the algorithm's superior ability to localize energy deposition more effectively within the tumor, thereby improving treatment efficiency while minimizing off-target heating in surrounding healthy tissues.

To demonstrate that the selected power levels ensure adequate thermal coverage, Table 7.3 reports the standard thermal estimators T90, T50 and T10, defined as the temperature exceeded by 90%, 50% and 10% of points in the tumor region [14].

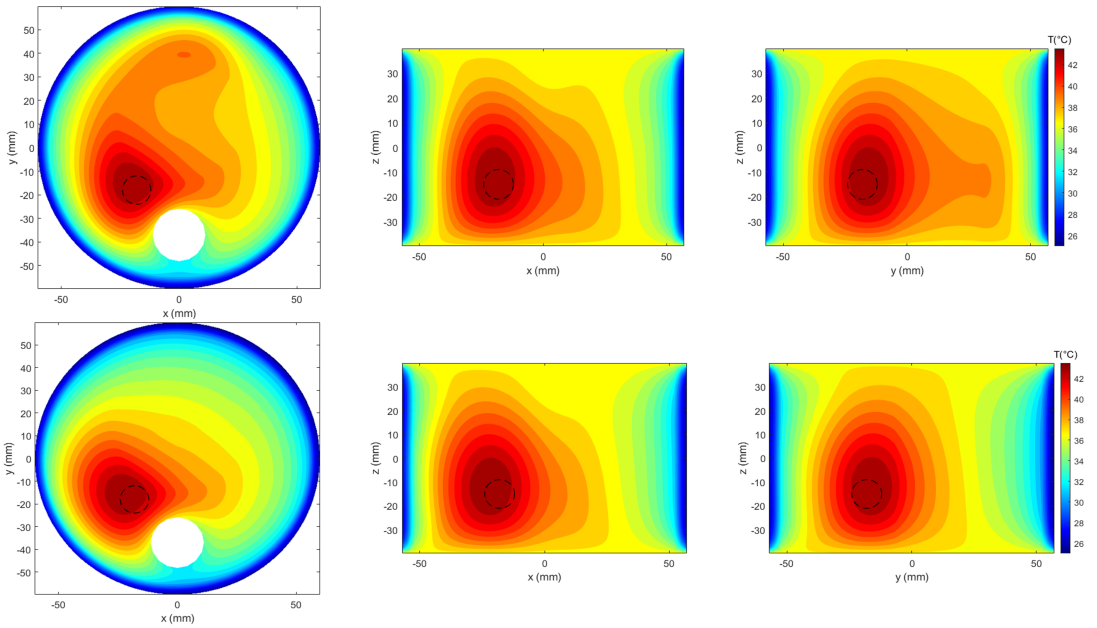

Figure 7.5: Temperature map comparison between PSO (upper row) and APA (lower row), visualized on the three canonical planes intersecting the tumor centroid. The maps correspond to the SAR distributions shown in Fig. 7.4, obtained with $P_0 = 26$ W for PSO and $P_0 = 16$ W for APA.

Table 7.3: Standard thermal estimators obtained with the different methods

Method	T90 (°C)	T50 (°C)	T10 (°C)
PSO	42.62	43.14	43.48
APA	42.55	43.14	43.51
APA (finer mesh)	42.63	43.13	43.46

The bottom line of Table 7.3 refers to the case where the feeding coefficients optimized with the APA approach (Table 7.1) are used in a COMSOL model with the maximum mesh size reduced from 5 mm to 2 mm in the all the neck tissues. A variation of less than 0.2% between values reported in the top and bottom lines of the table demonstrates the robustness of the mesh used to perform the optimization (Sec. 7.3.1).

7.3.4 Realistic testbed

To evaluate the performance of the APA-based optimization under anatomically realistic conditions, we also considered an HT setup implemented in the Sim4Life simulation platform [118], as illustrated in Fig. 7.6a. The numerical model is based on the phantom Duke V3.0 [124], a member of the Virtual Population (ViP), which was developed from high-resolution magnetic resonance imaging (MRI) scans of healthy volunteers. The phantom includes 305 anatomically segmented tissues, offering a comprehensive and physiologically accurate representation for electromagnetic and thermal simulations.

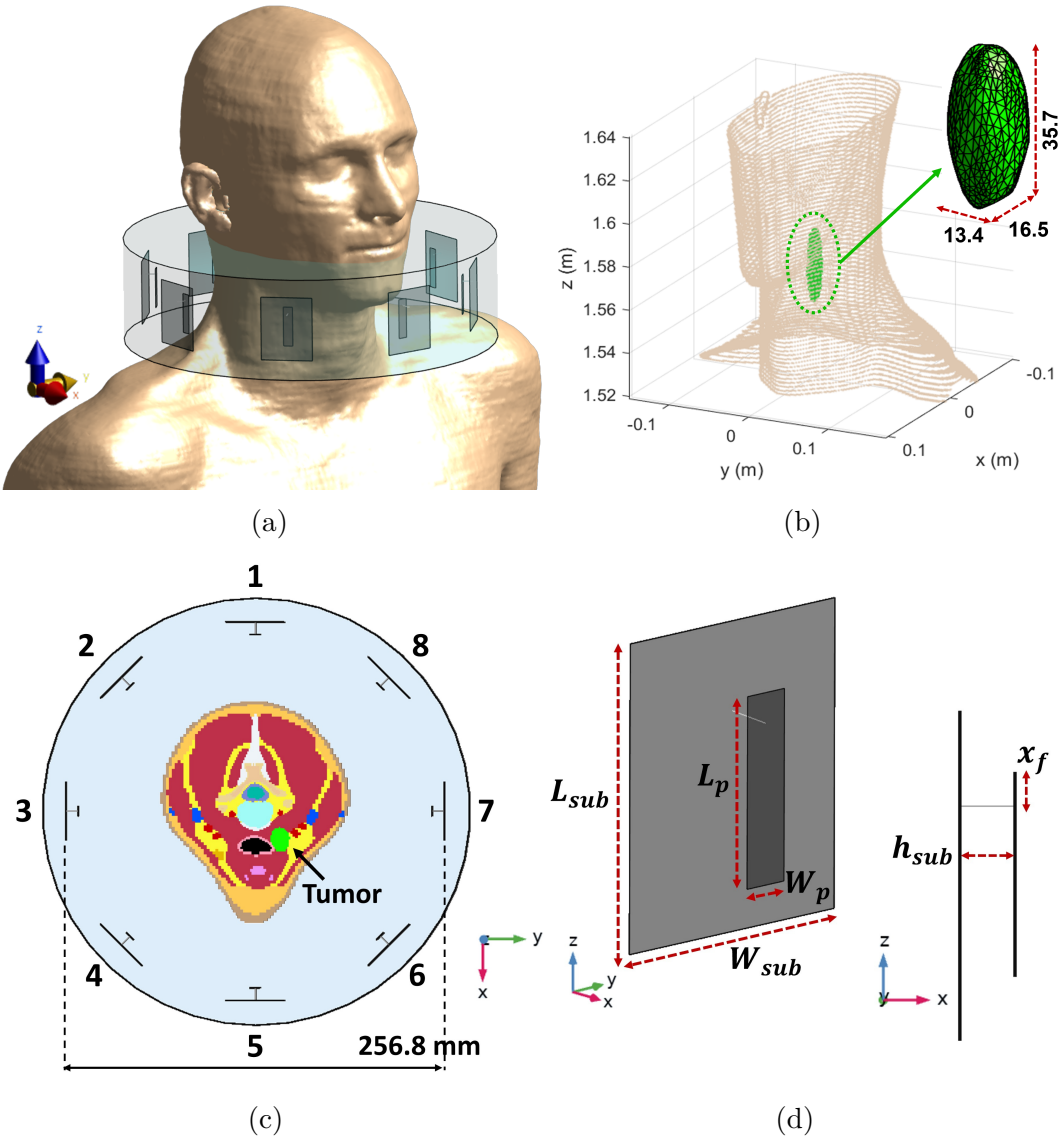

Figure 7.6: (**a**) Circular array of patch antennas surrounding the neck of the realistic phantom Duke V3.0 [124] and immersed in the waterbolus. (**b**) Tumor target size (expressed in mm) and its position near to the larynx of Duke. (**c**) Top view of the phased array applicator surrounding the segmented phantom visualized on the xy plane; the reported number are used to index the antennas of the array; the tumor target is highlighted in green. (**d**) Employed patch antenna and optimized dimensions.

A tumor region with irregular geometry—approximated as a deformed prolate spheroid—was inserted into the laryngotracheal area (centroid at $x_t = 18.02$ mm, $y_t = 16.15$ mm, $z_t = 1574.9$ mm), as shown in Fig. 7.6b. This placement enables the evaluation of SAR deposition performance in a clinically relevant scenario where

anatomical heterogeneity presents significant targeting challenges.

The treatment applicator consists of a uniform circular array of $N = 8$ patch antennas, optimized to operate at $f = 434$ MHz. While based on the same design principles as in the simplified testbed, the antenna dimensions were re-optimized to fit the anatomical features of the realistic phantom. The design parameters of each antenna, shown in Fig. 7.6d, include: $L_{sub} = 50$ mm, $W_{sub} = 40$ mm, $L_p = 31.0$ mm, $W_p = 7.2$ mm, $h_{sub} = 8.4$ mm, and $x_f = 4.96$ mm. As in the previous setup, a waterbolus surrounds the applicator (see Fig. 7.6c) [18].

In the Sim4Life model, the electromagnetic and thermal simulations are performed using the finite-difference time-domain (FDTD) method. A rectilinear mesh is employed, with a uniform voxel size of 2 mm in the phantom tissues and 1 mm in the antenna applicator, in compliance with the ESHO guidelines [14].

To apply the proposed APA algorithm, as described in Sec. 7.2, to this anatomically realistic testbed, the two thresholds must be defined according to the procedure outlined in Sec. 7.3.2, which provided the Pareto front displayed in Fig. 7.7a. For this setup, the thresholds were found to be: $(th_{low}, th_{up}) = (9.41, 5.8) \times 10^3$ V^2/m^2 for the mask shown in Fig. 7.1b. The $V^H_{\chi\%}$ indicator reported in Fig. 7.7b for the APA method using the selected thresholds shows an overall better SAR confinement than the PSO. The lower values achieved by the $V^H_{\chi\%}$ parameter in Fig. 7.7b with respect to Fig. 7.3b are due to the fact that the defined indicator is a relative parameter expressed over the total number of points in the healthy region,

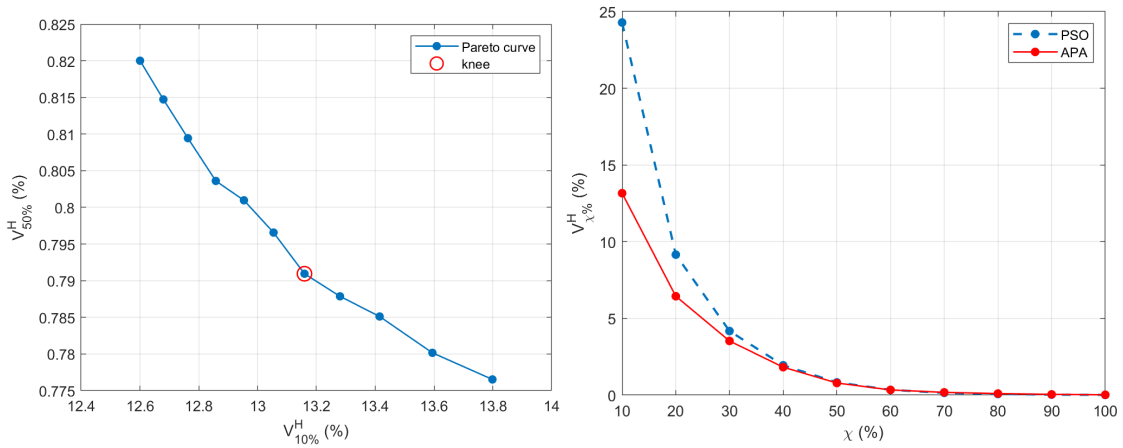

(a) (b)

Figure 7.7: (**a**) Pareto front generated during the APA threshold selection process, showing the trade-off between SAR confinement ($V^H_{10\%}$) and hotspot suppression ($V^H_{50\%}$). The knee point (highlighted in red) indicates the optimal point, corresponding to $(th_{low}, th_{up}) = (9.41,\ 5.8) \times 10^3$ V^2/m^2. (**b**) Comparison of the $V^H_{\chi\%}$ performance across increasing $\chi\%$ for the APA (using the thresholds corresponding to the knee point) and PSO-based SAR optimization.

which is significantly greater in the realistic case (1.13M points) with respect to the simplified model (56k points). For the realistic model, the computational time required by the APA, including the search algorithm, was less than 80 minutes as in the case of the PSO algorithm, here applied for comparison.

The resulting normalized SAR distributions—with respect to the maximum SAR within the tumor region ($\mathcal{T}$)—for a given input power are shown in Fig. 7.8. The maps, displayed on the three canonical planes intersecting the tumor centroid (marked by the green dot), compare PSO (upper row) and APA (lower row). While both methods achieve adequate energy focusing on the tumor region, the APA results exhibit a more spatially confined SAR pattern with significantly reduced hotspots in healthy tissues. This improvement arises from APA's ability to enforce adaptive spatial constraints through the use of a two-level power mask, which simultaneously enhances energy focusing on the tumor and suppresses power deposition in surrounding healthy regions.

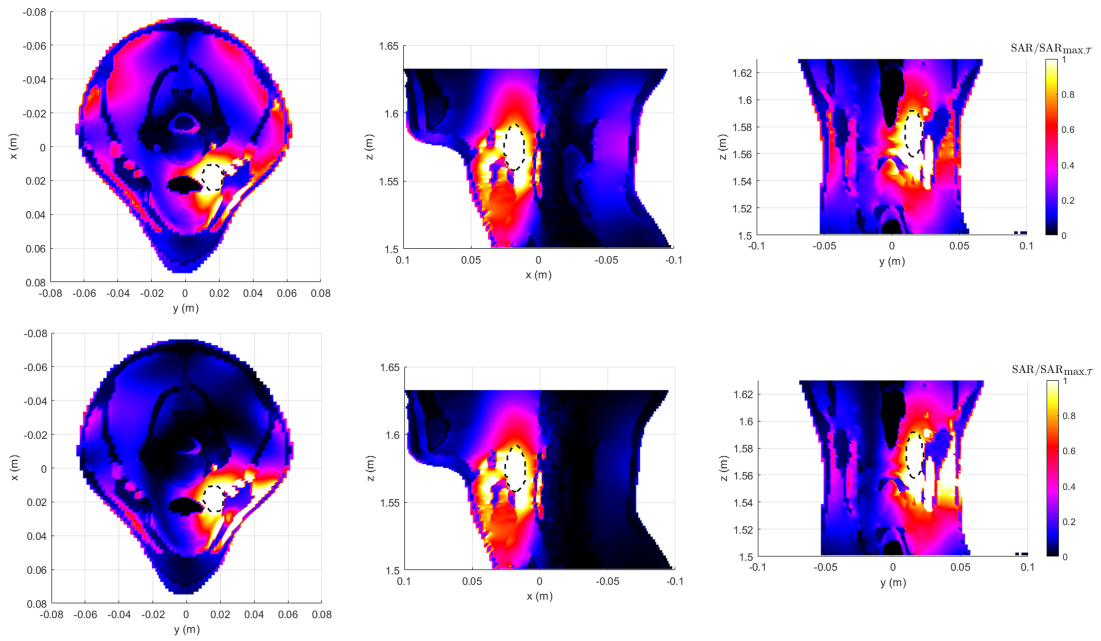

Figure 7.8: Normalized SAR maps comparison between PSO (upper row) and APA (lower row), displayed on the three canonical planes cutting the tumor sphere at its centroid. The black dashed line indicates the contour of the target tumor. The APA thresholds considered are $(th_{low}, th_{up}) = (9.41, 5.8) \times 10^3$ V^2/m^2. While both methods achieve good tumor coverage, the APA solution results in more confined SAR patterns, reducing hotspots outside the target.

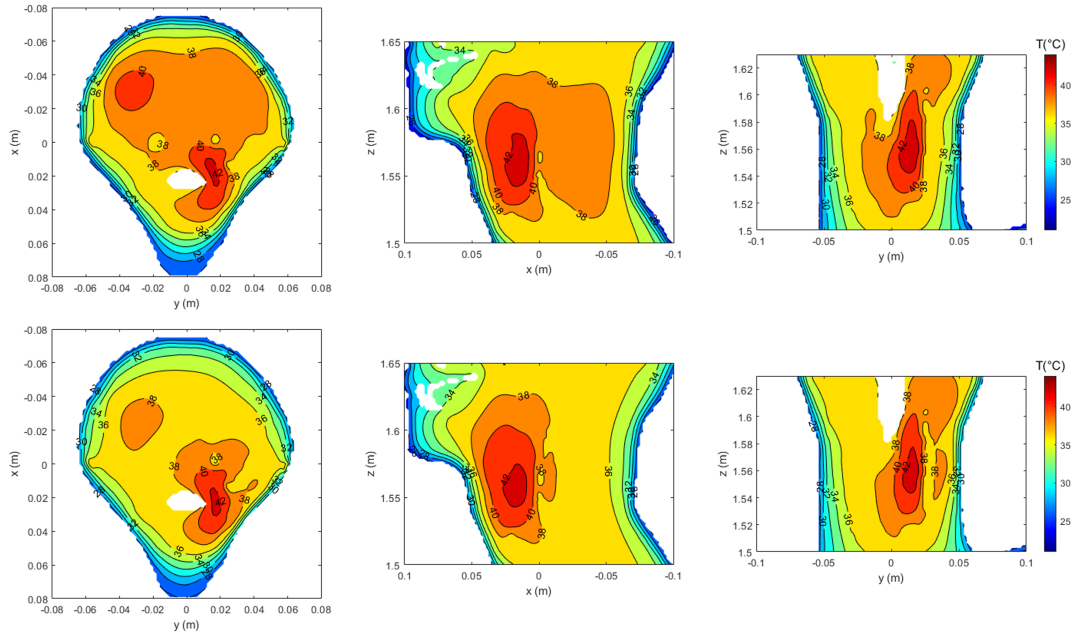

Figure 7.9: Temperature map comparison between PSO (upper row) and APA (lower row), visualized on the three canonical planes intersecting the tumor centroid. The maps correspond to the SAR distributions shown in Fig. 7.8, obtained with $P_0 = 60$ W for PSO and $P_0 = 44$ W for APA. Thanks to better energy focusing, APA achieves comparable tumor heating with lower input power, while also reducing the presence of hotspots in healthy tissues.

Similar to the simplified testbed, the thermal response in the realistic anatomical model was simulated by solving the Pennes' bioheat equation [35] in Sim4Life, incorporating tissue-specific thermal properties and perfusion rates [26] and completed with setting the boundary conditions as performed in Sec. 7.3.3 for the simplified phantom.

To further validate these results, the corresponding temperature distributions are illustrated in Fig. 7.9. The PSO algorithm required $P_0 = 60$ W to achieve effective heating (≥ 42°C in the tumor region), whereas the APA method reached comparable temperature levels with only $P_0 = 44$ W. This reduction in input power demonstrates the efficiency of APA in shaping the energy deposition more effectively, thus enhancing patient safety and minimizing the risk of overheating in the surrounding healthy tissues. The temperature maps also clearly reflect reduced hotspot formation in the APA case, aligning well with the SAR confinement observed in Fig. 7.8.

To further assess the thermal coverage achieved in the realistic testbed, Table 7.4 reports the same standard thermal estimators T90, T50 and T10, previously introduced in Sec. 7.3.3. These indicators confirm that both the PSO and APA methods deliver effective heating to the tumor region.

Table 7.4: Standard thermal estimators obtained with the different methods

Method	T90 (°C)	T50 (°C)	T10 (°C)
PSO	41.08	41.94	42.63
APA	41.05	41.83	42.50

7.4 Discussion and future works

While the present work focuses on demonstrating the APA optimization approach for deep hyperthermia in the H&N region—a particularly challenging anatomical site due to its complex geometry and heterogeneous tissue composition—the methodology presented is not limited to this application. The same optimization framework can be extended to other anatomical sites commonly treated with deep hyperthermia, such as the pelvic region for cervical and rectal cancer [14]. Investigating the performance of APA in such cases would allow for a broader validation of the method.

Another aspect worth exploring is the influence of tumor size and geometry on the achievable thermal coverage. In this study, we have evaluated the approach on a small irregularly shaped deep-seated tumor in the H&N region, representing a challenging scenario for hyperthermia treatment planning. However, larger or more irregularly shaped tumor models could present different optimization challenges. As a future work, systematic testing on a variety of tumor shapes and volumes would help quantify the robustness and adaptability of the APA algorithm.

Finally, although we limited the comparison of the proposed algorithm to the PSO method—selected because it is widely used in clinically applied SAR-based optimization routines [69]—other optimization strategies could serve as relevant benchmarks. For instance, time reversal [138] has been proposed in the literature as an alternative field-focusing method. While time reversal relies on certain approximations and may not capture full-wave nature of a metaheuristic optimization approach like PSO, its comparative evaluation against APA in realistic patient models could provide further insights.

7.5 Conclusions

This study presented a deterministic framework for SAR-based optimization in microwave cancer hyperthermia, using the Alternating Projections Algorithm (APA) as an efficient alternative to conventional metaheuristic approaches such as the Particle Swarm Optimization (PSO). By enforcing a two-level power mask, APA effectively shapes the electromagnetic energy deposition, achieving both strong tumor targeting and suppression of hotspots in surrounding healthy tissues.

To guide the mask selection process, we introduced an adaptive threshold search strategy based on the defined $V_{\chi\%}^{H}$ metric, which quantifies off-target SAR exposure. This metric enabled a systematic trade-off analysis, allowing the APA method to dynamically balance tumor coverage with safety constraints, while ensuring efficient heating of the tumor target.

The methodology was validated in both a simplified phantom and a realistic H&N anatomical model. In both cases, the APA method achieved SAR distributions and temperature profiles comparable to those obtained with the PSO algorithm, but with a significantly reduced presence of hotspots and lower required input power. Specifically, in the simplified model, comparable heating was achieved with just 16 W for APA versus 26 W for PSO. Similarly, in the realistic setup, APA reached the desired thermal performance with only 44 W, compared to 60 W for PSO.

In conclusion, the proposed APA-based SAR optimization method offers a robust and tunable alternative to PSO for SAR-based optimization in microwave hyperthermia treatment planning. Its deterministic nature and improved SAR and temperature distributions make it particularly attractive for anatomically complex targets, such as those found in the H&N region. Here, the algorithm was demonstrated using a two-level power mask; future work will explore its extension to multi-level masks and assess the resulting effects on focal quality and computational efficiency.

Chapter 8

Conclusions

This thesis addressed key bottlenecks in advancing microwave hyperthermia as a clinically reliable cancer treatment modality. The contributions span experimental, computational, and algorithmic dimensions, unified by the goal of enabling patient-specific, safe, and effective treatment planning and monitoring.

The research began with the development of a physical mock-up and its digital twin, enabling reproducible experimental validation and precise simulation-based studies. SAR-based optimization was investigated, introducing strategies that improved antenna matching and energy focusing without compromising treatment quality. The influence of blood flow on temperature distribution was explicitly quantified, underscoring the need for vascular modeling in hyperthermia planning.

The central contribution lies in the design of a real-time 3D temperature reconstruction framework. By merging sparse sensor data with libraries of pre-computed simulations, the method delivers accurate, robust, and computationally efficient temperature monitoring. This approach provides a pathway toward minimally invasive thermometry, addressing one of the major limitations of current clinical practice. Complementing this, the proposed APA-based optimization method offers a deterministic, low-power, and hotspot-suppressing alternative to conventional SAR-based optimization techniques, validated across simplified and realistic scenarios.

Taken together, these contributions demonstrate a coherent strategy for bridging the gap between simulation and clinical translation in hyperthermia. Future research may extend these methods to other anatomical sites, integrate uncertainty quantification more deeply, and explore clinical integration of the developed methods. Ultimately, the framework developed in this thesis contributes to the broader objective of establishing hyperthermia as a standard adjunct in cancer therapy, combining effectiveness with safety and accessibility.

Bibliography

[1] N. R. Datta et al., "Local hyperthermia combined with radiotherapy and-/or chemotherapy: Recent advances and promises for the future", *Cancer Treat. Rev.*, vol. 41, no. 9, pp. 742–53, 2015.

[2] P. K. Sneed et al., "Survival benefit of hyperthermia in a prospective randomized trial of brachytherapy boost ± hyperthermia for glioblastoma multiforme", *Int. J. Radiat. Oncol. Biol. Phys.*, vol. 40, no. 2, pp. 287–295, 1998, ISSN: 0360-3016.

[3] R. D. Issels, "High-risk soft tissue sarcoma: Clinical trial and hyperthermia combined chemotherapy", *Int. J. Hyperthermia*, vol. 22, no. 3, pp. 235–239, 2006, ISSN: 0265-6736. Accessed: Dec. 20, 2023.

[4] M. D. Hurwitz, "Hyperthermia and immunotherapy: Clinical opportunities", *International Journal of Hyperthermia*, vol. 36, no. sup1, pp. 4–9, 2019.

[5] G. C. Li, F. He, and C. C. Ling, "Hyperthermia and gene therapy: Potential use of micropet imaging", *International Journal of Hyperthermia*, vol. 22, no. 3, pp. 215–221, 2006.

[6] J. Overgaard et al., "Randomised trial of hyperthermia as adjuvant to radiotherapy for recurrent or metastatic malignant melanoma", *The Lancet*, vol. 345, no. 8949, pp. 540–543, 1995, ISSN: 0140-6736.

[7] R. B. Roemer, "Engineering aspects of hyperthermia therapy", *Annu. Rev. Biomed. Eng.*, vol. 1, pp. 347–376, 1999, ISSN: 1545-4274.

[8] J. van der Zee, D. González, G. C. van Rhoon, J. D. van Dijk, W. L. van Putten, and A. A. Hart, "Comparison of radiotherapy alone with radiotherapy plus hyperthermia in locally advanced pelvic tumours: A prospective, randomised, multicentre trial", *The Lancet*, vol. 355, no. 9210, pp. 1119–1125, 2000, ISSN: 0140-6736.

[9] J. R. Lepock, "Cellular effects of hyperthermia: Relevance to the minimum dose for thermal damage", *Int. J. Hyperthermia*, vol. 19, no. 3, pp. 252–266, 2003.

[10] S. N. Goldberg, G. S. Gazelle, and P. R. Mueller, "Thermal ablation therapy for focal malignancy: A unified approach to underlying principles, techniques, and diagnostic imaging guidance", *American Journal of Roentgenology*, vol. 174, no. 2, pp. 323–331, 2000.

[11] M. G. Lubner, C. L. Brace, J. L. Hinshaw, and F. T. Lee, "Microwave tumor ablation: Mechanism of action, clinical results, and devices", *Journal of Vascular and Interventional Radiology*, vol. 21, no. 8, Supplement, S192–S203, 2010, Thermal Ablation 2010: At the Crossroads of Past Success, Current Goals, and Future Technology.

[12] A. A. Gage and J. Baust, "Mechanisms of tissue injury in cryosurgery", *Cryobiology*, vol. 37, no. 3, pp. 171–186, 1998, ISSN: 0011-2240.

[13] S. S. Kitchen and C. J. Partridge, "A review of microwave diathermy", *Physiotherapy*, vol. 77, no. 9, pp. 647–652, 1991, ISSN: 0031-9406.

[14] M. M. Paulides et al., "ESHO benchmarks for computational modeling and optimization in hyperthermia therapy", *Int. J. Hyperthermia*, vol. 38, no. 1, pp. 1425–1442, 2021.

[15] M. Paulides, H. Dobsicek Trefna, S. Curto, and D. Rodrigues, "Recent technological advancements in radiofrequency- andmicrowave-mediated hyperthermia for enhancing drug delivery", en, *Adv. Drug Deliv. Rev.*, vol. 163-164, pp. 3–18, 2020, ISSN: 0169409X. Accessed: Jun. 23, 2023.

[16] M. M. Paulides et al., "The clinical feasibility of deep hyperthermia treatment in the head and neck: New challenges for positioning and temperature measurement", *Phys. Med. Biol.*, vol. 55, pp. 2465–2480, 2010.

[17] M. M. Paulides, J. F. Bakker, N. Chavannes, and G. C. van Rhoon, "A patch antenna design for application in a phased-array head and neck hyperthermia applicator", *IEEE Trans. Biomed. Eng.*, vol. 54, no. 11, pp. 2057–63, 2007.

[18] M. M. Paulides et al., "The HYPERcollar: A novel applicator for hyperthermia in the head and neck", *Int. J. Hyperthermia*, vol. 23, no. 7, pp. 567–76, 2007.

[19] C. Polk and E. Postow, *Handbook of Biological Effects of Electromagnetic Fields, Third Edition - 2 Volume Set*. CRC Press, 1995, ISBN: 978-0-8493-0641-9.

[20] H. H. Kampinga, "Cell biological effects of hyperthermia alone or combined with radiation or drugs: A short introduction to newcomers in the field", *Int. J. Hyperthermia*, vol. 22, no. 3, pp. 191–6, 2006.

[21] A. Vander Vorst and A. Rosen, *RF/Microwave Interaction with Biological Tissues*. John Wiley & Sons, Ltd, 2006, vol. 91, ISBN: 0-471-73277-X.

[22] P. J. W. Debye, *Polar molecules*. New York: The Chemical Catalog Company, Inc., 1929. [Online]. Available: http://archive.org/details/polarmolecules0000deby.

[23] K. S. Cole and R. H. Cole, "Dispersion and Absorption in Dielectrics I. Alternating Current Characteristics", *The Journal of Chemical Physics*, vol. 9, no. 4, pp. 341–351, 1941, ISSN: 0021-9606, 1089-7690.

[24] C. Gabriel, S. Gabriel, and E. Corthout, "The dielectric properties of biological tissues: I. literature survey", *Physics in medicine and biology*, vol. 41, pp. 2231–49, Dec. 1996.

[25] S. Gabriel, R. W. Lau, and C. Gabriel, "The dielectric properties of biological tissues: II. measurements in the frequency range 10 hz to 20 GHz", *Physics in Medicine and Biology*, vol. 41, no. 11, pp. 2251–2269, 1996, ISSN: 0031-9155, 1361-6560. Accessed: Feb. 24, 2023.

[26] P. A. Hasgall et al., *IT'IS database for thermal and electromagnetic parameters of biological tissues*. 2018. [Online]. Available: http://www.itis.ethz.ch/database.

[27] R. F. Verhaart et al., "Accurate 3D temperature dosimetry during hyperthermia therapy by combining invasive measurements and patient-specific simulations", *Int. J. Hyperthermia*, vol. 31, no. 6, pp. 686–92, 2015.

[28] W. T. Joines, Y. Zhang, C. Li, and R. L. Jirtle, "The measured electrical properties of normal and malignant human tissues from 50 to 900 MHz", *Medical Physics*, vol. 21, no. 4, pp. 547–550, Apr. 1994.

[29] M. Lazebnik et al., "A large-scale study of the ultrawideband microwave dielectric properties of normal, benign and malignant breast tissues obtained from cancer surgeries", en, *Physics in Medicine and Biology*, vol. 52, no. 20, pp. 6093–6115, 2007, ISSN: 0031-9155, 1361-6560. Accessed: Aug. 17, 2025.

[30] M. T. Bevacqua, G. G. Bellizzi, L. Crocco, and T. Isernia, "A method for quantitative imaging of electrical properties of human tissues from only amplitude electromagnetic data", *INVERSE PROBLEMS*, vol. 35, no. 2, 2019.

[31] M. Bevacqua, G. Bellizzi, T. Isernia, and L. Crocco, "A method for effective permittivity and conductivity mapping of biological scenarios via segmented contrast source inversion", *Progress In Electromagnetics Research*, vol. 168, pp. 1–15, Nov. 2019.

[32] C. A. Balanis, *Advanced Engineering Electromagnetics*, 3rd ed. John Wiley & Sons, 2024.

[33] J. D. Jackson, *Classical electrodynamics*, 3rd. New York, NY: John Wiley & Sons, Ltd, 1999, ISBN: 9780471309321. [Online]. Available: http://cdsweb.cern.ch/record/490457.

[34] *IEC/IEEE International Standard – Determining the peak spatial-average specific absorption rate (SAR) in the human body from wireless communications devices, 30 MHz to 6 GHz – Part 1: General requirements for using the finite-difference time-domain (FDTD) method for SAR calculations*, Standard IEC/IEEE 62704-1:2017, 2017. [Online]. Available: https://ieeexplore.ieee.org/document/8088404.

[35] H. H. Pennes, "Analysis of tissue and arterial blood temperatures in the resting human forearm", *J. Appl. Physiol.*, vol. 1, no. 2, pp. 93–122, 1948.

[36] H. P. Kok, C. A. T. van den Berg, A. Bel, and J. Crezee, "Fast thermal simulations and temperature optimization for hyperthermia treatment planning, including realistic 3D vessel networks", *Med. Phys.*, vol. 40, no. 10, 2013.

[37] H. P. Kok, P. M. van Haaren, J. B. van de Kamer, J. Wiersma, J. D. van Dijk, and J. Crezee, "High-resolution temperature-based optimization for hyperthermia treatment planning", *Phys. Med. Biol.*, vol. 50, no. 13, pp. 3127–41, 2005.

[38] H. P. Kok, P. Wust, P. R. Stauffer, F. Bardati, G. C. van Rhoon, and J. Crezee, "Current state of the art of regional hyperthermia treatment planning: A review", *Radiat. Oncol.*, vol. 10, 2015.

[39] M. M. Paulides et al., "Simulation techniques in hyperthermia treatment planning", *Int. J. Hyperthermia*, vol. 29, no. 4, pp. 346–57, 2013.

[40] E. Schena, D. Tosi, P. Saccomandi, E. Lewis, and T. Kim, "Fiber Optic Sensors for Temperature Monitoring during Thermal Treatments: An Overview", *Sensors*, vol. 16, no. 7, p. 1144, 2016, ISSN: 1424-8220.

[41] G. M. Hahn, *Hyperthermia and Cancer*. Springer, 1982.

[42] J. G. Webster, *Medical Instrumentation: Application and Design*, 4th ed. Wiley, 2010.

[43] A. Beccaria et al., "Temperature monitoring of tumor hyperthermal treatments with optical fibers: Comparison of distributed and quasi-distributed techniques", *Optical Fiber Technology*, vol. 60, p. 102 340, 2020, ISSN: 1068-5200.

[44] LumaSense Technologies, *Luxtron fiber optic thermometry probes and accessories*, https://www.advancedenergy.com/products/measurement-controls/temperature-measurement/fluoroptic-thermometry/, Commercial fluoroptic sensors, 2024.

[45] Opsens Solutions, *Gaas fiber optic temperature sensors (otg-m series)*, https://opsens-solutions.com/products/fiber-optic-temperature-sensors/, Commercial GaAs bandgap sensors, 2024.

[46] R. Gassino, A. Vallan, and G. Perrone, "Evaluation of temperature measurement errors due to fbg sensors during laser ablation of ex-vivo porcine liver", in *2018 IEEE International Instrumentation and Measurement Technology Conference (I2MTC)*, 2018, pp. 1–5.

[47] R. Gaffoglio et al., "Real-time 3D temperature reconstruction in microwave cancer hyperthermia from scarce temperature measurements", *Nat. Commun.*, vol. 16, no. 1, p. 4824, 2025, ISSN: 2041-1723.

[48] COMSOL Multiphysics, *version 6.1*. www.comsol.it, 2024.

[49] R. Gaffoglio et al., "Highly reproducible tissue-mimicking phantoms for hyperthermia applications", in *IEEE Antennas and Propagation Society International Symposium and URSI National Radio Science Meeting*, 2024.

[50] C. K. McGarry et al., "Tissue mimicking materials for imaging and therapy phantoms: A review", *Phys. Med. Biol.*, vol. 65, no. 23, 2020.

[51] D. Andreuccetti, R. Fossi, and C. Petrucci, *An Internet resource for the calculation of the dielectric properties of body tissues in the frequency range 10 Hz - 100 GHz*. IFAC-CNR, Florence (Italy), 1997.

[52] G. Hartsgrove, A. Kraszewski, and A. Surowiec, "Simulated biological materials for electromagnetic radiation absorption studies", *Bioelectromagnetics*, vol. 8, no. 1, pp. 29–36, 1987.

[53] T. Drizdal, M. M. Paulides, N. van Holthe, and G. C. van Rhoon, "Hyperthermia treatment planning guided applicator selection for sub-superficial head and neck tumors heating", *Int. J. Hyperthermia*, vol. 34, no. 6, pp. 704–13, 2018.

[54] G. Ruvio et al., "Comparison of different methods for dielectric properties measurements in liquid sample media", *Int. J. RF Microw. C. E.*, vol. 28, no. 3, 2018.

[55] SPEAG probe. https://speag.swiss/products/dak/dak-probes/.

[56] *Standard Test Method for Determining Specific Heat Capacity by Differential Scanning Calorimetry*. 2018.

[57] A. Lorenzati, S. Fantucci, A. Capozzoli, and M. Perino, "VIPs thermal conductivity measurement: Test methods, limits and uncertainty", *Energy Procedia*, vol. 78, pp. 418–23, 2015.

[58] M. Firuzalizadeh et al., "Digital twin of a H&N microwave cancer hyperthermia setup using comsol multiphysic", in *COMSOL Conference*, 2024. [Online]. Available: https://www.comsol.com/paper/digital-twin-of-a-hn-microwave-cancer-hyperthermia-setup-using-comsol-multiphysics-135142.

[59] M. M. Paulides, J. F. Bakker, A. P. M. Zwamborn, and G. C. Van Rhoon, "A head and neck hyperthermia applicator: Theoretical antenna array design", *Int. J. Hyperthermia*, vol. 23, no. 1, pp. 59–67, 2007.

[60] CST Studio Suite 2022, *www.cst.com*. Dassault Systèmes Simulia, 2024.

[61] M. Saporito, "Implementation of a control system for sar and temperature focusing in a head and neck cancer hyperthermia applicator", M.S. thesis, Politecnico di Torino, Torino, Italy, 2022. [Online]. Available: https://webthesis.biblio.polito.it/23602/.

[62] J.-M. Jin, *The Finite Element Analysis of Antennas and Arrays*. John Wiley & Sons, Feb. 2009, ISBN: 0470401281.

[63] M. Firuzalizadeh et al., "Joint optimization of antenna system matching and specific absorption rate focusing in microwave hyperthermia cancer treatment", *Cancers*, vol. 17, no. 3, 2025, ISSN: 2072-6694.

[64] S. Mumtaz, J. N. Rana, E. H. Choi, and I. Han, "Microwave Radiation and the Brain: Mechanisms, Current Status, and Future Prospects", en, *Int. J. of Molecular Sciences*, vol. 23, no. 16, p. 9288, 2022, ISSN: 1422-0067.

[65] H. P. Kok et al., "Heating technology for malignant tumors: A review", *Int. J. Hyperthermia*, vol. 37, no. 1, pp. 711–741, 2020, ISSN: 0265-6736. Accessed: Oct. 4, 2023.

[66] Z. Rijnen, P. Togni, R. Roskam, S. G. van de Geer, R. H. Goossens, and M. M. Paulides, "Quality and comfort in head and neck hyperthermia: A redesign according to clinical experience and simulation studies", *Int. J. Hyperthermia*, vol. 31, no. 8, pp. 823–30, 2015.

[67] G. Bruggmoser et al., "Quality assurance for clinical studies in regional deep hyperthermia", en, *Strahlenther Onkol*, vol. 187, no. 10, pp. 605–610, 2011, ISSN: 1439-099X. Accessed: Jul. 29, 2024.

[68] S. Gavazzi et al., "Advanced patient-specific hyperthermia treatment planning", *Int. J. Hyperthermia*, vol. 37, no. 1, pp. 992–1007, 2020.

[69] Z. Rijnen et al., "Clinical integration of software tool VEDO for adaptive and quantitative application of phased array hyperthermia in the head and neck", *Int. J. Hyperthermia*, vol. 29, no. 3, pp. 181–93, 2013.

[70] D. A. M. Iero, L. Crocco, and T. Isernia, "Thermal and microwave constrained focusing for patient-specific breast cancer hyperthermia: A robustness assessment", *IEEE Trans. Antennas Propag.*, vol. 62, no. 2, pp. 814–21, 2014.

[71] G. G. Bellizzi, T. Drizdal, G. C. van Rhoon, L. Crocco, T. Isernia, and M. M. Paulides, "The potential of constrained SAR focusing for hyperthermia treatment planning: Analysis for the head & neck region", *Phys. Med. Biol.*, vol. 64, no. 1, 2018.

[72] R. A. M. Canters, M. M. Paulides, M. Franckena, J. W. Mens, and G. C. van Rhoon, "Benefit of replacing the Sigma-60 by the Sigma-Eye applicator: A Monte Carlo-based uncertainty analysis", *Strahlenther Onkol.*, vol. 189, no. 1, pp. 74–80, 2013.

[73] M. de Greef, H. P. Kok, D. Correia, A. Bel, and J. Crezee, "Optimization in hyperthermia treatment planning: The impact of tissue perfusion uncertainty", *Med. Phys.*, vol. 37, no. 9, pp. 4540–50, 2010.

[74] H. K. Lee et al., "Superficial hyperthermia and irradiation for recurrent breast carcinoma of the chest wall: Prognostic factors in 196 tumors", *Int. J. Radiat. Oncol. Biol. Phys.*, vol. 40, no. 2, pp. 365–75, 1998.

[75] H. P. Kok et al., "Online Adaptive Hyperthermia Treatment Planning During Locoregional Heating to Suppress Treatment-Limiting Hot Spots", en, *Int. J. Radiat. Oncol. Biol. Phys.*, vol. 99, no. 4, pp. 1039–1047, 2017, ISSN: 03603016. Accessed: Apr. 15, 2024.

[76] "IEEE Standard for Definitions of Terms for Antennas", *IEEE Std 145-2013 (Revision of IEEE Std 145-1993)*, pp. 1–50, 2014.

[77] R. A. Canters, M. Franckena, M. M. Paulides, and G. C. van Rhoon, "Patient positioning in deep hyperthermia: Influences of inaccuracies, signal correction possibilities and optimization potential", *Phys. Med. Biol.*, vol. 54, no. 12, pp. 3923–36, 2009.

[78] M. Zanoli and H. D. Trefna, "Iterative time-reversal for multi-frequency hyperthermia", *Phys. Med. Biol.*, vol. 66, no. 4, 2021.

[79] D. Pozar, "The active element pattern", *IEEE Trans. Antennas Propag.*, vol. 42, no. 8, pp. 1176–1178, 1994.

[80] MATLAB, *R2023a*. Natick, Massachusetts: The MathWorks Inc., 2023.

[81] J. Kennedy and R. C. Eberhart, "Particle swarm optimization", in *IEEE International Conference on Neural Networks*, vol. 4, 1995.

[82] M. M. Paulides, S. H. J. A. Vossen, A. P. M. Zwamborn, and G. C. van Rhoon, "Theoretical investigation into the feasibility to deposit RF energy centrally in the head-and-neck region", *Int J Radiat Oncol Biol Phys*, vol. 63, no. 2, pp. 634–642, 2005, ISSN: 0360-3016.

[83] M. M. Paulides, G. M. Verduijn, and N. Van Holthe, "Status quo and directions in deep head and neck hyperthermia", *Radiat. Oncol*, vol. 11, no. 21, pp. 809–21, 2016.

[84] J. W. Hand, J. J. W. Lagenduk, J. B. Andersen, and J. C. Bolomey, "Quality assurance guidelines for ESHO protocols", *Int. J. Hyperthermia*, vol. 5, no. 4, pp. 421–428, 1989, ISSN: 0265-6736, 1464-5157.

[85] T. Samaras, P. Rietveld, and G. Van Rhoon, "Effectiveness of FDTD in predicting SAR distributions from the lucite cone applicator", *IEEE Trans. Microwave Theory Techn.*, vol. 48, no. 11, pp. 2059–2063, 2000, ISSN: 00189480. Accessed: Oct. 14, 2024.

[86] A. Bellone, E. Ullo, M. Olivero, G. Coppa, A. Vallan, and G. Perrone, "Preliminary analysis of the estimation of tissue thermal parameters for tumor laser ablation with minimally invasive techniques", in *Proceedings of the IEEE International Conference on Intrumentation and Measurement*, 2024.

[87] G. M. Verduijn et al., "Deep hyperthermia with the HYPERcollar system combined with irradiation for advanced head and neck carcinoma – a feasibility study", *Int. J. Hyperthermia*, vol. 34, no. 7, 2018, ISSN: 0265-6736. Accessed: Jan. 14, 2025.

[88] M. Firuzalizadeh et al., "Heat focusing in head and neck hyperthermia considering vessels blood flow", in *The 19th European Conference on Antennas and Propagation (EuCAP)*, 2025.

[89] R. Gaffoglio, M. Righero, G. Giordanengo, M. Zucchi, and G. Vecchi, "Fast Optimization of Temperature Focusing in Hyperthermia Treatment of Sub-Superficial Tumors", *IEEE J. Electromagn. RF Microw. Med. Biol.*, vol. 5, no. 3, pp. 286–293, Sep. 2021, ISSN: 2469-7249, 2469-7257.

[90] M. Franckena et al., "Long-term improvement in treatment outcome after radiotherapy and hyperthermia in locoregionally advanced cervix cancer: An update of the dutch deep hyperthermia trial", *International Journal of Radiation Oncology*Biology*Physics*, vol. 70, no. 4, pp. 1176–1182, 2008, ISSN: 0360-3016.

[91] N. Cihoric et al., "Hyperthermia-related clinical trials on cancer treatment within the ClinicalTrials.gov registry", *Int. J. Hyperthermia*, vol. 31, no. 6, pp. 609–14, 2015.

[92] N. R. Datta, S. Rogers, S. Gómez Ordóñez, E. Puric, and S. Bodis, "Hyperthermia and radiotherapy in the management of head and neck cancers: A systematic review and meta-analysis", *Int. J. of Hyperthermia*, vol. 32, no. 1, pp. 31–40, 2016.

[93] M. Kroesen et al., "Confirmation of thermal dose as a predictor of local control in cervical carcinoma patients treated with state-of-the-art radiation therapy and hyperthermia", *Radiother. Oncol.*, vol. 140, pp. 150–58, 2019.

[94] C. C. Vernon et al., "Radiotherapy with or without hyperthermia in the treatment of superficial localized breast cancer: Results from five randomized controlled trials", *International Journal of Radiation Oncology*Biology*Physics*, vol. 35, no. 4, pp. 731–744, 1996.

[95] A. Bakker, J. van der Zee, G. van Tienhoven, H. P. Kok, C. R. N. Rasch, and H. Crezee, "Temperature and thermal dose during radiotherapy and hyperthermia for recurrent breast cancer are related to clinical outcome and thermal toxicity: A systematic review", *Int. J. Hyperthermia*, vol. 36, no. 1, pp. 1024–39, 2019.

[96] J. Crezee et al., "Improving locoregional hyperthermia delivery using the 3-D controlled AMC-8 phased array hyperthermia system: A preclinical study", *Int. J. Hyperthermia*, vol. 25, no. 7, pp. 581–92, 2009.

[97] H. P. Kok et al., "Predictive value of simulated sar and temperature for changes in measured temperature after phase-amplitude steering during locoregional hyperthermia treatments", *International Journal of Hyperthermia*, vol. 35, no. 1, pp. 330–339, 2018.

[98] E. Balidemaja et al., "Hyperthermia treatment planning for cervical cancer patients based on electrical conductivity tissue properties acquired in vivo with EPT at 3 T MRI", *Int. J. Hyperthermia*, vol. 32, no. 5, pp. 558–568, 2016.

[99] J. A. Groen, J. Crezee, H. W. van Laarhoven, M. F. Bijlsma, and H. P. Kok, "Quantification of tissue property and perfusion uncertainties in hyperthermia treatment planning: Multianalysis using polynomial chaos expansion", *Computer Methods and Programs in Biomedicine*, vol. 240, p. 107 675, 2023.

[100] H. P. Kok and J. Crezee, "Hyperthermia treatment planning: Clinical application and ongoing developments", *IEEE Journal of Electromagnetics, RF and Microwaves in Medicine and Biology*, vol. 5, no. 3, pp. 214–222, 2021.

[101] G. C. van Rhoon and P. W. and, "Introduction: Non-invasive thermometry for thermotherapy", *International Journal of Hyperthermia*, vol. 21, no. 6, pp. 489–495, 2005.

[102] F. Adibzadeh, K. Sumser, S. Curto, D. T. B. Yeo, A. A. Shishegar, and M. M. P. and, "Systematic review of pre-clinical and clinical devices for magnetic resonance-guided radiofrequency hyperthermia", *International Journal of Hyperthermia*, vol. 37, no. 1, pp. 15–27, 2020.

[103] M. Zhu, Z. Sun, and C. K. Ng, "Image-guided thermal ablation with mr-based thermometry", *Quantitative Imaging in Medicine and Surgery*, vol. 7, no. 3, 2017.

[104] Medtronic, *Risk of tissue overheating due to inaccurate magnetic resonance thermometry - Letter to Health Care Providers*. U.S. Food and Drug Administration, 2021.

[105] J. Conway, M. S. Hawley, A. D. Seagar, B. H. Brown, and D. C. Barber, "Applied potential tomography (apt) for noninvasive thermal imaging during hyperthermia treatment", *Electronics Letters*, vol. 21, pp. 836–838, 1985.

[106] M. J. Moskowitz, T. P. Ryan, K. D. Paulsen, and S. E. M. and, "Clinical implementation of electrical impedance tomography with hyperthermia", *International Journal of Hyperthermia*, vol. 11, no. 2, pp. 141–149, 1995.

[107] K. D. Paulsen, M. J. Moskowitz, T. P. Ryan, S. E. Mitchell, and P. J. H. and, "Initial in vivo experience with eit as a thermal estimator during hyperthermia", *International Journal of Hyperthermia*, vol. 12, no. 5, pp. 573–591, 1996.

[108] R. Poni, E. Neufeld, M. Capstick, S. Bodis, T. Samaras, and N. Kuster, "Feasibility of temperature control by electrical impedance tomography in hyperthermia", *Cancers*, vol. 13, no. 13, 2021.

[109] A. Chaudhuri et al., "Predictive digital twin for optimizing patient-specific radiotherapy regimens under uncertainty in high-grade gliomas", *Frontiers in Artificial Intelligence*, vol. 6, Oct. 2023.

[110] M. Kapteyn, J. Pretorius, and K. Willcox, "A probabilistic graphical model foundation for enabling predictive digital twins at scale", *Nature Computational Science*, vol. 1, pp. 1–11, May 2021.

[111] T. Hernandez-Boussard et al., "Digital twins for predictive oncology will be a paradigm shift for precision cancer care", *Nature Medicine*, vol. 27, Nov. 2021.

[112] R. Laubenbacher, B. Mehrad, I. Shmulevich, and N. Trayanova, "Digital twins in medicine", *Nature Computational Science*, vol. 4, no. 3, pp. 184–191, 2024.

[113] K. Willcox and B. Segundo, "The role of computational science in digital twins", *Nature Computational Science*, vol. 4, no. 3, pp. 147–149, 2024. Accessed: Apr. 2, 2025.

[114] National Academies of Sciences, *Foundational Research Gaps and Future Directions for Digital Twins* (The National Academies Collection: Reports funded by National Institutes of Health). Washington (DC): National Academies Press (US), 2024.

[115] R. Verhaart, Z. Rijnen, V. Fortunati, G. Verduijn, T. Walsum, and J. Veenland, "Temperature simulations in hyperthermia treatment planning of the head and neck region: Rigorous optimization of tissue properties", *Strahlentherapie und Onkologie*, vol. 190, Jul. 2014.

[116] B. W. Raaymakers, M. Van Vulpen, J. J. Lagendijk, A. A. De Leeuw, J. Crezee, and J. J. Battermann, "Determination and validation of the actual 3D temperature distribution during interstitial hyperthermia of prostate carcinoma", *Physics in Medicine and Biology*, vol. 46, no. 12, pp. 3115–3131, 2001.

[117] I. Vilas-Boas Ribeiro et al., "Pod–kalman filtering for improving noninvasive 3d temperature monitoring in mr-guided hyperthermia", *Medical Physics*, vol. 49, Jun. 2022.

[118] Sim4Life, *version 7.0*. https://zmt.swiss/sim4life/, 2022.

[119] T. Hastie, "Ridge regularization: An essential concept in data science", *Technometrics*, vol. 62, pp. 1–21, Jul. 2020.

[120] E. J. Candès, J. K. Romberg, and T. Tao, "Stable signal recovery from incomplete and inaccurate measurements", *Communications on Pure and Applied Mathematics*, vol. 59, no. 8, pp. 1207–1223, 2006.

[121] E. Candes and T. Tao, "The Dantzig selector: Statistical estimation when p is much larger than n", *The Annals of Statistics*, vol. 35, no. 6, pp. 2313–2351, Dec. 2007, Publisher: Institute of Mathematical Statistics.

[122] A. Altman and J. G. and, "Regularized symmetric indefinite systems in interior point methods for linear and quadratic optimization", *Optimization Methods and Software*, vol. 11, no. 1-4, pp. 275–302, 1999.

[123] R. J. Vanderbei and T. J. Carpenter, "Symmetric indefinite systems for interior point methods", *Mathematical Programming*, vol. 58, no. 1, pp. 1–32, Jan. 1993.

[124] M.-C. Gosselin et al., "Development of a new generation of high-resolution anatomical models for medical device evaluation: The virtual population 3.0", *Physics in Medicine and Biology*, vol. 59, no. 18, pp. 5287–5303, 2014.

[125] M. L. van der Gaag, M. De Bruijne, T. Samaras, J. van der Zee, and G. C. van Rhoon, "Development of a guideline for the water bolus temperature in superficial hyperthermia", *Int. J. Hyperthermia*, vol. 22, no. 8, pp. 637–56, 2006.

[126] E. R. McFadden Jr. et al., "Thermal mapping of the airways in humans", *J. Appl. Physiol.*, vol. 58, no. 2, pp. 564–70, 1985.

[127] H. D. Trefná et al., "Quality assurance guidelines for superficial hyperthermia clinical trials: I. clinical requirements", *International Journal of Hyperthermia*, vol. 33, no. 4, pp. 471–482, 2017.

[128] J. Lang, B. Erdmann, and M. Seebass, "Impact of nonlinear heat transfer on temperature control in regional hyperthermia", *IEEE Trans. Biomed. Eng.*, vol. 46, no. 9, pp. 1129–38, 1999.

[129] C. Carrapiço-Seabra, M. D. Lazzari, A. Ameziane, G. C. van Rhoon, H. D. Trefná, and S. C. and, "Application of the esho-qa guidelines for determining the performance of the lca superficial hyperthermia heating system", *International Journal of Hyperthermia*, vol. 40, no. 1, p. 2 272 578, 2023.

[130] J. van der Zee, J. N. Peer-Valstar, P. J. Rietveld, L. de Graaf-Strukowska, and G. C. van Rhoon, "Practical limitations of interstitial thermometry during deep hyperthermia", *International Journal of Radiation Oncology*Biology*Physics*, vol. 40, no. 5, pp. 1205–1212, 1998, ISSN: 0360-3016.

[131] R. Geoghegan, G. ter Haar, K. Nightingale, L. Marks, and S. Natarajan, "Methods of monitoring thermal ablation of soft tissue tumors – a comprehensive review", *Medical Physics*, vol. 49, no. 2, pp. 769–791, 2022.

[132] H. Arkin, L. xu, and K. Holmes, "Recent developments in modeling heat transfer in blood perfused tissues", *IEEE transactions on bio-medical engineering*, vol. 41, pp. 97–107, Mar. 1994.

[133] A. Kotte, G. van Leeuwen, J. de Bree, et al., "A description of discrete vessel segments in thermal modelling of tissues", *Phys. Med. Biol.*, vol. 41, no. 5, pp. 865–884, 1996.

[134] M. Firuzalizadeh, R. Gaffoglio, G. Giordanengo, M. Righero, and G. Vecchi, "Specific Absorption Rate Optimization in Microwave Cancer Hyperthermia via Local Power Synthesis Algorithm", *Cancers*, vol. 17, no. 17, p. 2813, 2025, ISSN: 2072-6694. [Online]. Available: https://www.mdpi.com/2072-6694/17/17/2813.

[135] K. Nikita, N. Maratos, and N. Uzunoglu, "Optimal steady-state temperature distribution for a phased array hyperthermia system", *IEEE Trans. on Bio. Eng.*, vol. 40, no. 12, pp. 1299–1306, 1993.

[136] S. K. Das, S. T. Clegg, and T. V. Samulski, "Computational techniques for fast hyperthermia temperature optimization", *Medical Physics*, vol. 26, no. 2, pp. 319–328, 1999.

[137] F. Bardati, A. Borrani, A. Gerardino, and G. Lovisolo, "Sar optimization in a phased array radiofrequency hyperthermia system", *IEEE Trans. on Bio. Eng.*, vol. 42, no. 12, pp. 1201–1207, 1995.

[138] H. D. Trefná, J. Vrba, and M. Persson, "Time-reversal focusing in microwave hyperthermia for deep-seated tumors", *Physics in medicine and biology*, vol. 55, pp. 2167–85, Mar. 2010.

[139] C. A. Liontas and P. Knott, "An alternating projections algorithm for optimizing electromagnetic fields in regional hyperthermia", in *2016 10th European Conference on Antennas and Propagation (EuCAP)*, 2016, pp. 1–5.

[140] C. A. Liontas, "Alternating projections of auxiliary vector fields for electric field optimization in temperature-guided hyperthermia", in *2019 13th European Conference on Antennas and Propagation (EuCAP)*, 2019, pp. 1–5.

[141] O. M. Bucci, G. D'Elia, G. Mazzarella, and G. Panariello, "Antenna pattern synthesis: A new general approach", *Proc. IEEE*, vol. 82, no. 3, pp. 358–71, 1994.

[142] J. L. Araque Quijano and G. Vecchi, "Alternating adaptive projections in antenna synthesis", *IEEE Trans. Antennas Propag.*, vol. 58, no. 3, pp. 727–737, 2010.

[143] G. G. Bellizzi, L. Crocco, G. M. Battaglia, and T. Isernia, "Multi-frequency constrained sar focusing for patient specific hyperthermia treatment", *IEEE Journal of Electromagnetics, RF and Microwaves in Medicine and Biology*, vol. 1, no. 2, pp. 74–80, 2017.

[144] S. Zumbo, T. Isernia, and M. T. Bevacqua, "A simple auxiliary model for field amplitude shaping in complex environments, and application to mri shimming", *IEEE Open Journal of Antennas and Propagation*, vol. 3, pp. 917–931, 2022.

[145] G. G. Bellizzi, D. A. M. Iero, L. Crocco, and T. Isernia, "Three-dimensional field intensity shaping: The scalar case", *IEEE Antennas and Wireless Propagation Letters*, vol. 17, no. 3, pp. 360–363, 2018.

[146] M. T. Bevacqua, T. Isernia, and S. Zumbo, "Shaping intensities of complex scalar fields in inhomogeneous scenarios via linearly combined bricks", *IEEE Open Journal of Antennas and Propagation*, pp. 1–1, 2025.

[147] F. P. Yosandha, K. Adi, and C. E. Widodo, "Calculation of lung cancer volume of target based on thorax computed tomography images using active contour segmentation method for treatment planning system", *J. Phys.: Conf. Ser.*, vol. 855, no. 012063, 2017.

This Ph.D. thesis has been typeset by means of the TEX-system facilities. The typesetting engine was pdfLATEX. The document class was `toptesi`, by Claudio Beccari, with option `tipotesi=scudo`. This class is available in every up-to-date and complete TEX-system installation.